# Studies on cloud bands causing heavy snowfalls during a cold air outbreak over the Sea of Japan

**Hisaki Eito**

# Acknowledgements

The author would like to express his sincere gratitude to Professor Shigeo Yoden of Kyoto University for his elaborated guidance and a lot of invaluable advice for this dissertation. The author wishes to express his heartfelt appreciation to Dr. Teruyuki Kato of the Japan Meteorological Agency (JMA) for his invaluable comments, helpful support, and considerable encouragement throughout this work. The author also wishes to express his deep gratitude to Dr. Masanori Yoshizaki of the Japan Agency for Marine-Earth Science and Technology (JAMSTEC) for providing the author an opportunity for research on mesoscale meteorology and participation in the field campaign “Winter MCSs Observations over the Japan Sea in 2001 (WMO-01) ”. The author deeply thanks Dr. Chiashi Muroi of the JMA, Drs. Kazuo Saito, Masataka Murakami, Kenichi Kusunoki, Ahoro Adachi, and Syugo Hayashi of the Meteorological Research Institute (MRI), and Dr. Hiroshi Kuroiwa of the National Institute of Information and Communications Technology, for their helpful comments, valuable cooperation, and continuous encouragement. The author wishes to express his sincere gratitude to Professors Takehiko Satomura, Hirohiko Ishikawa, Hitoshi Mukougawa, Keiichi Ishioka, and Shinobu Machida of Kyoto University for their valuable comments and careful reading of the manuscript. The author is also deeply grateful to Professors Yasushi Fujiyoshi and Masayuki Kawashima of Hokkaido University for their fruitful discussions and helpful comments.

The author especially wishes to express his deepest appreciation to Emeritus Professor Isamu Hirota of Kyoto University for his invaluable guidance in research on meteorology and heartfelt encouragement over the years. The author is also profoundly grateful to Professor Kaoru Sato of the University of Tokyo for her helpful and hearty guidance in how to research on meteorology. Thanks are extended to Drs. Tadashi Tsuyuki, Masaomi Nakamura, Fumiaki Fujibe, Kazumasa Aonashi, Yoshinori Shoji, Hiromu Seko, and other members of the MRI for their valuable advices and continuous encouragement regarding research on mesoscale meteorology.

The WMO-01 field campaign was mainly conducted under the framework of Core Research for Evolutional Science and Technology ‘‘Studies on structure

and formation/development Mechanisms of Mesoscale Convective Systems'' by the fund of the Japan Science and Technology Agency. The author thanks the organizations and members participated in the WMO-01 field campaign. The author wishes to express his special gratitude to Professor Kiyotaka Nakagawa of Rissho University for his devoted support and invaluable cooperation in carrying out the WMO-01.

The numerical simulations of this work were performed mainly using the super computer system operated by the MRI and partly using the Earth Simulator operated by JAMSTEC. The Earth Simulator was used under the framework of the Research Revolution 2002 project ''Development of Super-High-Resolution Global and Regional Climate Models'', called ''Kyosei-4 project'' funded by the Ministry of Education, Culture, Sports, Science, and Technology. The author thanks members of the Kyosei-4 modeling group.

Finally, the author would like to express his heartfelt appreciation to his wife, Hiromi, and his family, Ryota and Masaki, for their understanding and hearty support.

# Abstract

During the winter monsoon season, mesoscale convective systems (MCSs) frequently form around the western coastal regions of the Japanese Islands. Line-shaped MCSs (cloud bands) with a long lifetime often bring heavy snowfalls in coastal plain areas ("P-type" heavy snowfalls), sometimes seriously confusing human activities there. Therefore, to understand the processes of P-type heavy snowfalls, the formation and maintenance mechanisms of the cloud bands should be clarified. However, they remain poorly understood because of the lack of detailed observations and high-resolution numerical simulations. In this thesis, the author investigates the detailed structures and the formation and maintenance mechanisms of the cloud bands that bring P-type heavy snowfalls, using the high-resolution data provided by the special observations during a field campaign "Winter MCSs Observations over the Japan Sea in 2001" (WMO-01) and a high-resolution cloud resolving model, the Japan Meteorological Agency (JMA) nonhydrostatic mesoscale model (JMA-NHM).

P-type heavy snowfalls occurred over the coastal region of the Hokuriku and San-in districts, middle and western part of Japan, during the period of 12–17 January 2001, when an upper-level synoptic-scale trough was quasi-stationary over the Sea of Japan. Various cloud bands periodically formed and developed under the effect of moving upper-level positive potential vorticity anomalies around the trough, causing heavy snowfalls to the coastal plain areas. These include a quasi-stationary snowband along the coastal line of the Hokuriku district and the broad cloud band associated with the Japan-Sea Polar-Airmass Convergence Zone (JPCZ cloud band) extending over the Sea of Japan from the base of the Korean Peninsula to the Japanese Islands.

On 16 January 2001, a meso-β-scale snowband was observed in the coastal area of the eastern Hokuriku district. This snowband stagnated for about half a day, bringing a heavy snowfall in this region. The structure and the formation and maintenance mechanisms were investigated on the basis of observations (e.g., Doppler radars, boundary layer radars, and upper-air soundings) and simulation results of the JMA-NHM with a horizontal resolution of 1 km. The results can be summarized as follows:

1. Structures of the snowband
    - Convective snow cells with the horizontal scale of a few km successively formed at the northern part of the snowband and propagated east-southeastward.
    - Meso-γ-scale convective snow systems were organized of developed snow cells in the snowband.
    - A cold pool formed under the snowband.
2. Formation mechanism of the snowband
    - A land breeze was a trigger for the formation of the snowband.
3. Formation mechanism of the cold pool and its role in maintenance of the snowband
    - The diabatic cooling due to sublimation of snow was responsible for the formation of the cold pool.
    - The cold pool contributed to the maintenance of the horizontal convergence with the northwesterly winter monsoon at the northern edge of the snowband by compensating for the weakened land breeze.

On 14 January 2001, the JPCZ cloud band extended in a southeastward direction from the base of the Korean Peninsula to Wakasa Bay, and it stagnated during a half day. The JPCZ cloud band was organized by two cloud regions: one was a long cloud band extending along its southwestern edge (a developed convective cloud band), and the other was the region consisting of cloud bands normal to a wind direction of the winter monsoon extending to the northeast from the developed convective cloud band (transversal cloud bands). It is well known that the developed convective cloud band forms on the low-level convergence line at southwestern edge of the JPCZ cloud band and brings heavy snowfalls on the downstream coastal region. On the other hand, the structure and the formation mechanism of the transversal cloud bands have not been well understood; therefore, the author examined them closely on the basis of observations (e.g., satellite images, in-situ measurement and cloud profiling radar data from an instrumented aircraft, and upper-air soundings from observation vessels) and the simulation results of the JMA-NHM with a horizontal resolution of 1 km. The results can be summarized as follows:

1. Structures of the transversal cloud bands
    - The transversal cloud bands extended along a northeast-southwest direction, which was parallel to the direction pointed by the vertical

shear vector of horizontal wind in the mixed layer.

- They mainly consisted of convective clouds, which slanted with height toward the downshear side.
- They widened and deepened toward southwest, as the depth of the mixed layer increased.
- A convectively unstable layer was observed in the lower layer under the transversal cloud bands.

2. Formation mechanism of the transversal cloud bands

- The transversal cloud bands were accompanied by roll circulations.
- The axes of rolls were oriented nearly parallel to the direction of the vertical shear vector in the mixed layer.
- The roll circulations derived most of its energy from the mean vertical shear and the buoyancy.

In this thesis, the author clarified the detailed structures and the formation and maintenance processes of the cloud bands causing P-type heavy snowfalls, such as the snowband and the JPCZ cloud band, on the basis of observations and numerical experiments with high-resolution. Moreover, the author focused the relation between the snowband and the JPCZ cloud band. Some of the results obtained through this study indicate that the transversal cloud bands with a convectively unstable low-level air tend to flow into the snowband. This suggests that the transversal cloud bands play an important role in the formation and maintenance of the snowband. These findings regarding on the cloud bands in this thesis have led us to deeper understanding of the cause and detailed process for P-type heavy snowfalls in the western coastal region of the Japanese Islands during a cold air outbreak.

# Contents

# List of Figures

# List of Tables

# Chapter 1

# General introduction

## 1.1 Heavy snowfalls in the western coastal region of the Japanese Islands during the winter monsoon season

When cold air outbreaks occur from the Eurasian Continent in winter, many clouds frequently form and develop over the Sea of Japan. A geographical map around the Sea of Japan is shown in Fig. 1.1. As a cold air mass from the Eurasian Continent flows out over the relatively warm sea, a great amount of heat and water vapor is supplied from the sea surface (e.g., Asai 1965; Ninomiya 1968). The increase of heat and moisture in the lower layer makes the air mass moist and unstable. Consequently, convective clouds form and develop over the Sea of Japan, causing snowfalls in the downstream coastal region.

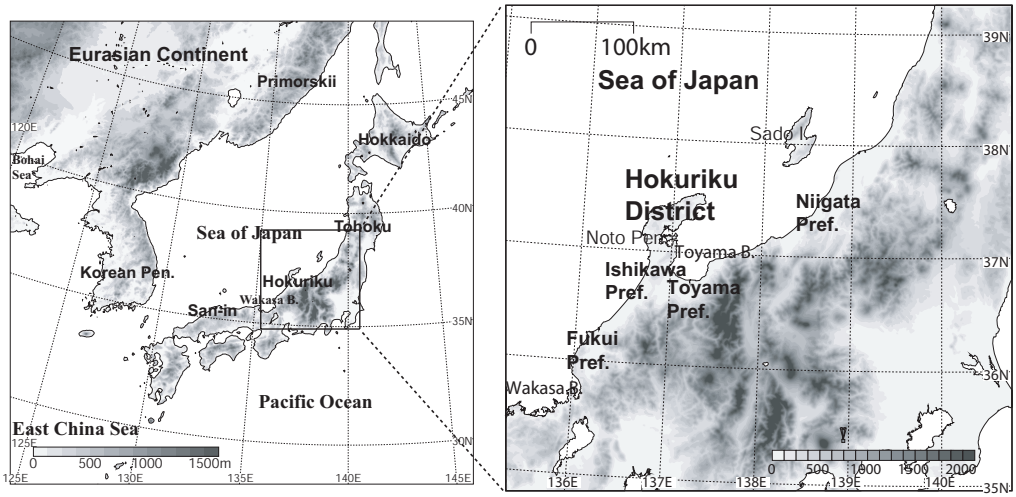


Figure 1.1: Geographical map around the Sea of Japan. The enlarged portion included the Hokuriku district.

Snowfalls occur frequently over mountain areas and sometimes over coastal plain areas, depending on large-scale situations. In Japan, the former type of snowfall is usually called “mountain-snowfall type” (referred to hereafter as “M-type”) and the latter “plain snowfall type” (referred to hereafter as “P-type”). As a typical example of M-type, accumulated precipitation map during the period of 18-19 December 2005 is shown in Fig. 1.2a. The maximum precipitation areas are observed in the mountain region of the Niigata and Toyama prefectures while the minimum areas spread in the coastal region of the Hokuriku district, middle part of Japan. As a typical example of P-type, accumulated precipitation map during the period of 15-16 January 2001 is shown in Fig. 1.2b. In contrast to the distribution of M-type precipitation shown in Fig. 1.2a, the maximum precipitation areas are observed in the coastal region of the Hokuriku district.

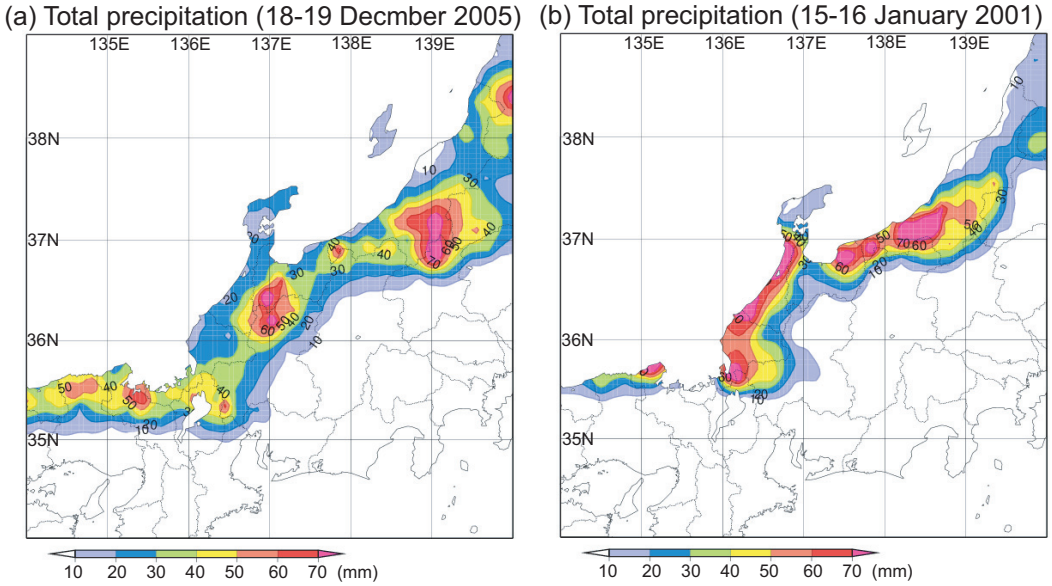


Figure 1.2: Horizontal maps of total precipitation amount during the period of (a) 18–19 December 2005 and (b) 15–16 January 2001.

M-type heavy snowfalls occur when a wedge-shaped deep upper trough propagates fast over the Japanese Islands, accompanied with a rapidly developing surface low pressure near the Japanese Islands (Akiyama 1981a, 1981b). In this situation, the intensity of the winter monsoon tends to become strong and its direction is perpendicular to the mountain range. Consequently,

convective clouds over the Sea of Japan flow into the mountain range, and they develop by orographic lifting (e.g., Estoque and Ninomiya 1976).

P-type heavy snowfalls occur when a cold vortex slowly propagates to east after protruding southward over the Sea of Japan (Akiyama 1981a, 1981b). In this situation, surface low pressure does not rapidly develop near the Japanese Islands, and therefore the intensity of the winter monsoon is rather weak. Convective clouds develop under the cold vortex aloft situating over the Sea of Japan. Sometimes, they are organized into mesoscale convective systems (MCSs) and cause concentrated snowfalls over the coastal plain area (e.g., Matsumoto et al. 1967; Miyazawa 1968; Sakakibara 1988a).

Although P-type heavy snowfalls occur less frequently than M-type heavy snowfalls, the former bring snowfalls even in coastal urban areas, sometimes seriously confusing human activities there. Therefore, improvement on short-range snowfall forecast to reduce the impact from heavy snowfalls is becoming a great concern of the public. To achieve this objective, the formation and maintenance processes of the MCSs causing P-type heavy snowfalls and their snowfall mechanisms should be well understood.

## 1.2 Cloud bands over the Sea of Japan

Various types of MCS's such as line-shaped disturbances (e.g., cloud bands) and vortex disturbances (e.g., polar lows) occur over the Sea of Japan during cold air outbreaks. As shown in meteorological satellite images, cloud bands appear most frequently over the Sea of Japan. Among various types of MCSs, cloud bands tend to cause heavy snowfalls (Sakakibara 1988a), because cloud bands often have a long lifetime and they tend to be quasi-stationary in the same place.

As shown in meteorological satellite images, cloud bands are usually extending along a low-level wind direction of the winter monsoon. Such cloud bands are called as longitudinal (wind-parallel) mode cloud bands (e.g., Tsuchiya and Fujita 1967). Longitudinal-mode cloud bands, which have also been known as "cloud streets", are most common among the cloud bands observed over the Sea of Japan. As a typical example of the longitudinal-mode cloud bands, the Geostationary Meteorological Satellite (GMS) visible image at 12 Japan Standard Time (JST; JST = Coordinated Universal Time (UTC) + 9

hours) on 16 January 2001 is shown in Fig. 1.3, showing that the longitudinal-mode cloud bands extending from the Eurasian Continent to the Japanese Islands cover most of the Sea of Japan. Typical longitudinal-mode cloud bands form in a shallow convective mixed layer; therefore, their cloud tops are not so high. The top height of longitudinal-mode cloud bands is observed as ~2 km over the Sea of Japan (e.g., Miura 1986). The longitudinal-mode cloud bands with a spacing of 5–20 km (e.g., Miura 1986) are oriented parallel to the mean wind direction.

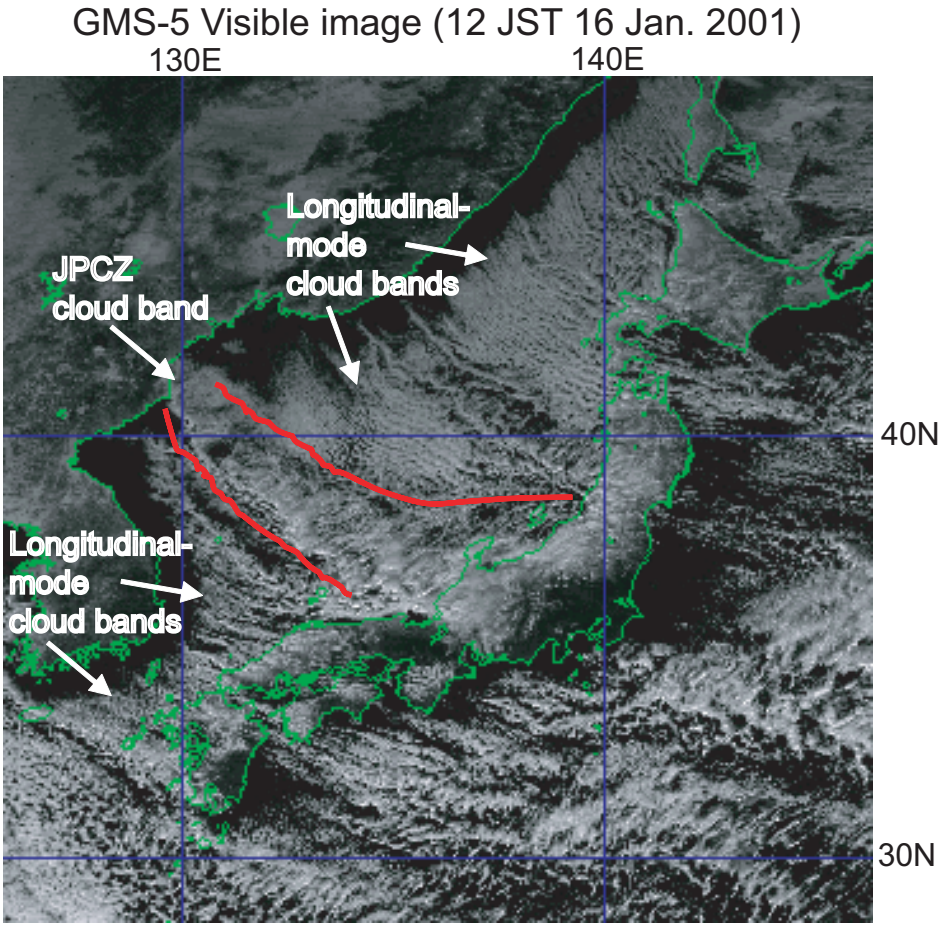


Figure 1.3: GMS-5 visible image at 1200 JST on 16 January 2001. Two red lines denote the boundaries of the JPCZ cloud band.

It is well known that the longitudinal-mode cloud bands are produced from roll convections related to thermal instability in the vertical shear flow (e.g., Asai 1970a, 1970b, and 1972). The longitudinal-mode cloud bands mainly bring

snowfalls to the mountain area, due mainly to development of clouds by orographic lifting of air mass (e.g., Estoque and Ninomiya 1976). As described in the previous section, they cause M-type heavy snowfalls under the strong monsoon situation (e.g., Akiyama 1981a, 1981b). Therefore, the formation and precipitation mechanisms of the longitudinal-mode cloud bands are well understood.

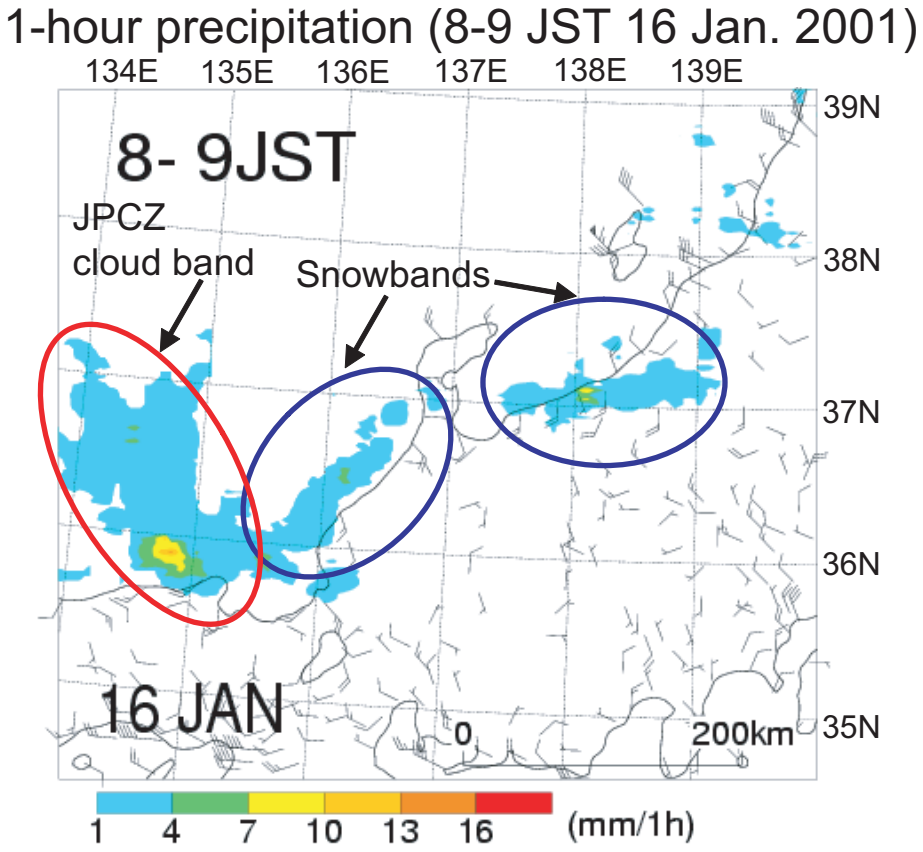


Figure 1.4: Horizontal map of hourly accumulated precipitation at 1500 JST on 16 January 2001, obtained by the Radar/Raingauge-Analyzed Precipitation. Wind barbs denote surface wind velocities observed by the Automated Meteorological Data Acquisition System (AMeDAS). Half, full, and triangle-shaped barbs mean 2.5 m $s^{-1}$, 5 m $s^{-1}$, and 25 m $s^{-1}$, respectively. Two blue circles denote precipitation areas corresponding to snowbands. A red circle denotes a precipitation area corresponding to the JPCZ cloud band.

In addition to the longitudinal-mode cloud bands, some other remarkable

cloud systems with line-shaped structures are observed over the Sea of Japan. Cloud bands, which are often referred to as “snowbands”, are frequently observed in the coastal region facing to the Sea of Japan (e.g., Sakakibara et al. 1988a). As a typical example of snowbands, an hourly-accumulated precipitation chart at 0900 JST on 16 January 2001 is shown in Fig. 1.4. Two line-shaped precipitation areas are observed along the coastal line of the Hokuriku district, corresponding to snowbands. These snowbands stagnated for about half a day and brought a heavy snowfall in the coastal region (see Fig. 1.2b). Snowbands are considered to form and develop over the convergence zone between the northwesterly monsoon wind and the local wind affected by the land, i.e., a land breeze (e.g., Ishihara et al. 1989; Tsuboki et al. 1989).

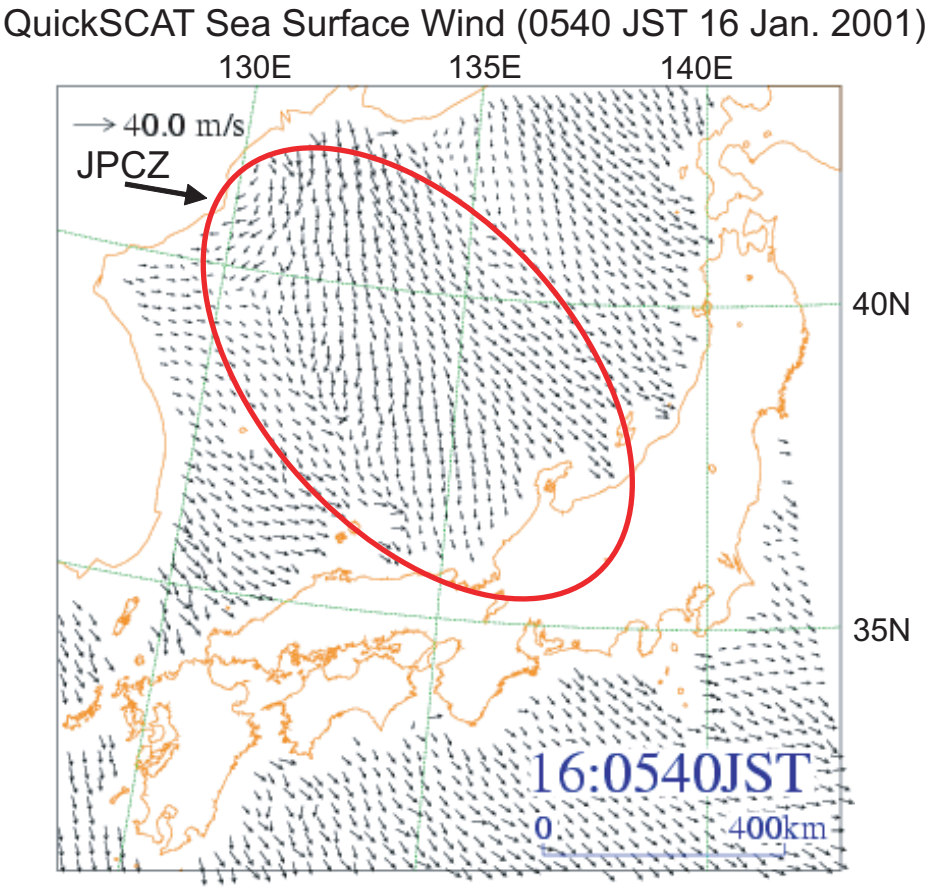


Figure 1.5: Sea surface wind velocities retrieved using observation data from NASA/JPL's SeaWinds Scatterometer aboard the QuikSCAT satellite at 0540 JST on 16 January 2001. A red circle denotes the JPCZ.

Moreover, a broad cloud band extending southeastward from the base of the Korean Peninsula to the Japanese Islands is occasionally observed by meteorological satellites (Okabayashi 1969, 1972; Okabayashi and Satomi 1971). The broad cloud band forms over the Japan-Sea Polar-Airmass Convergence Zone (JPCZ; Asai 1988), which is the low-level convergence zone between two airmasses with different characteristics. In this thesis, the broad cloud band associated with the JPCZ is referred to hereafter as the "JPCZ cloud band". A typical example of the JPCZ cloud band is shown in Fig. 1.3. The JPCZ cloud band with a width of 200–300 km is observed over the Sea of Japan from the base of the Korean Peninsula to the Hokuriku district and San-in district, western part of Japan. The low-level convergence zone is also seen in the sea surface wind field (Fig. 1.5), corresponding to the JPCZ. As shown in Fig. 1.4, a line-shaped precipitation area is observed around the San-in district. This corresponds to the downstream part of the JPCZ cloud band, causing a heavy snowfall to the coastal area of the San-in district (see Fig 1.2b).

As described in the previous subsection, heavy snowfalls tend to occur over the coastal plain area, when cold vortex is over the Sea of Japan and the intensity of the winter monsoon is rather weak (e.g., Akiyama 1981a, 1981b). In this situation, snowbands tend to form and develop along the coastal line, causing heavy snowfalls (see Figs 1.2b and 1.3; e.g., Ishihara et al. 1989; Tsuboki et al. 1989). The JPCZ cloud band brings heavy snowfalls to the coastal region of the Japanese Islands, because the downstream part of the JPCZ cloud band contains active convective clouds (see Figs 1.2b and 1.3; e.g., Okabayashi 1969; Yagi et al. 1986). The JPCZ cloud band also develops and brings heavy snowfalls to the coastal plain area, when a short trough along the rim of cold vortex approaches the JPCZ cloud band (e.g. Nagata 1992; Ohigashi and Tsuboki 2007). Therefore, its formation, development, and maintenance processes and precipitation mechanisms should be studied for understanding heavy snowfalls and improvement on heavy snowfall forecast over the coastal plain area.

## 1.3 Snowbands

Snowbands often form and develop in the Sea of Japan-side coastal regions of the Japanese Islands. They are one form of MCSs with a long lifetime and a

line-shaped structure, and occasionally bring a large amount of snowfall to a narrow area in the coastal region (see Fig. 1.4). Many studies have been made on the mesoscale structures of snowbands over the Sea of Japan mainly using Doppler radars.

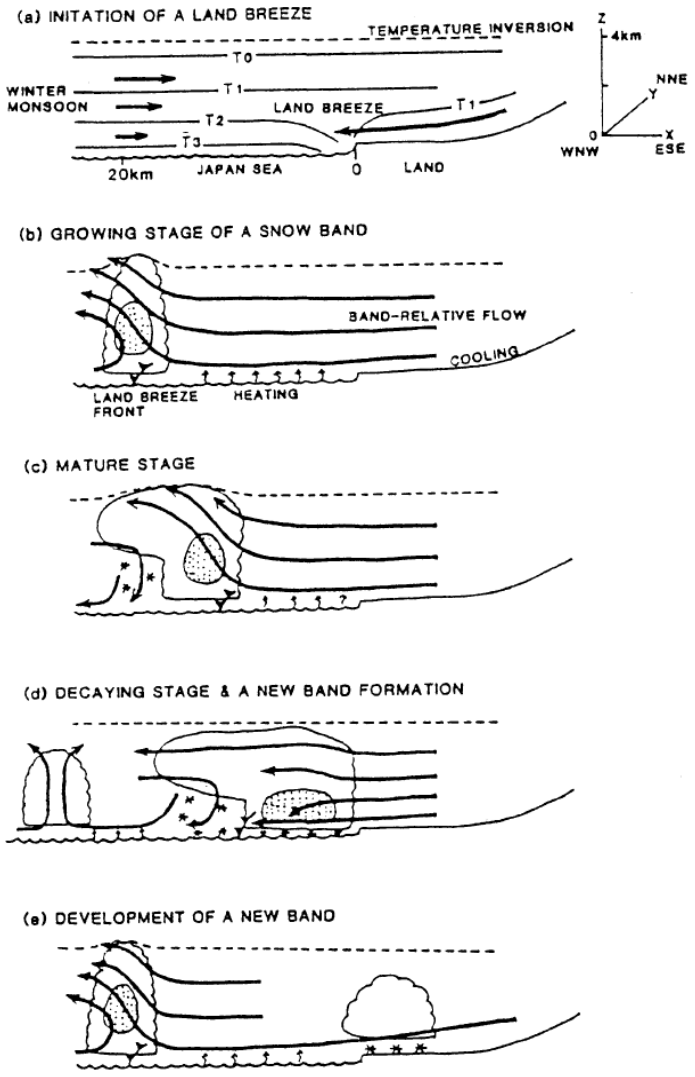


Figure 1.6: Schematic depiction of the evolution of the land breeze-induced snowbands observed around the coastal region of the western Hokuriku district on 23 January 1984 in the vertical cross section perpendicular to the alignment of the snowbands (Ishihara et al. 1989).

Sakakibara et al. (1988b) observed squall-line like snowbands in the western

Hokuriku district. They showed that the descending current from rear to front, found relative to the snowband under the anvil, was significant for the formation of new convective cells. They indicated that the diabatic cooling through sublimation of snow particles played an important role in the enhancement of this descending current. Ishihara et al. (1989) also observed snowbands along the costal line in the western Hokuriku district. Figure 1.6 depicts, in schematic form, the evolution of the snowbands. They revealed that the formation and successive production of the snowbands resulted from the coupling of three flows: A land breeze, the northwesterly monsoon, and a low-level outflow originating from anvil-like clouds at the rear of the snowbands.

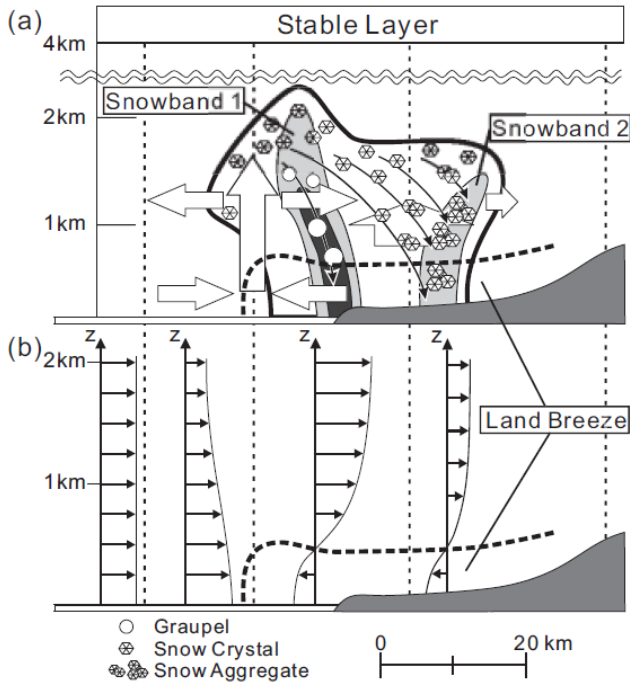


Figure 1.7: Schematic representation of the structures and maintenance processes of the double snowbands observed around the coastal region of the western Hokuriku district from 15 to 16 January 2001 in the vertical cross section perpendicular to the alignment of the snowbands. The thick broken lines indicate the outline of a land breeze. (a) The thick solid line represents the outline of the echo region. The strong reflectivity regions are shaded. The thick arrows show the wind relative to the ambient wind, and the thin arrows indicate the trajectories of particles. The precipitation particle types (graupel, snow crystal, and snow aggregate) are shown. (b) Vertical profiles of horizontal wind in the cross section (Ohigashi and Tsuboki 2005).

Recently, Ohigashi and Tsuboki (2005) investigated stationary double snowbands along the costal line in the western Hokuriku district, mainly using Doppler and dual-polarization radars. A schematic representation of the structures and maintenance processes of the double snowbands is given in Fig. 1.7. They revealed that the convergence between a land breeze and the winter monsoon mainly contributed to the formation and maintenance of the snowbands. They also examined their microphysical structures and interactions between the two snowbands using dual-polarization radar data. They found that the transportation of snow crystals from one snowband was significant for the maintenance of another snowband. Yoshihara et al. (2004) also observed several migratory snowbands along the eastern Hokuriku district associated with a cold front using a dual-Doppler radar system. They revealed that a low-level mesoscale convergence line between a westerly and a relatively colder southwesterly, which formed at 10-30 km offshore, contributed significantly to the successive development of the snowbands.

Doppler radar studies conducted concerning snowbands observed along the west coast of Hokkaido, northern part of Japan (Fujiyoshi et al. 1988; Tsuboki et al. 1989). They revealed the detailed structures and movements of a land breeze, and the interaction between the snowband and the land breeze. Maki et al. (1992) observed a longitudinal-mode snowband in the northern Tohoku district, northeastern part of Japan. They found that a strong downdraft existed in the center of a snow cloud, and it induced a low-level cold outflow in front of the snow cloud. Fujiyoshi et al. (1992) observed that a snowband formed on the lee side of mountain in the west coast of Hokkaido. They reported that the snowband was composed of meso-γ-scale cloud systems. Two longitudinal-mode snowbands were observed in the western coast of Hokkaido using a dual-Doppler radar system (Fujiyoshi et al. 1998; Yoshimoto et al. 2000). Fujiyoshi et al. (1998) revealed that the evolution of strong band-parallel winds played an important role in the organization and maintenance of the meso-γ-scale systems, organized into one snowband. They indicated that strong band-parallel winds formed due to sublimation of ice and snow particles near the cloud top. Yoshimoto et al. (2000) examined the interactions between the two snowbands. They found that the transportation of ice and snow particles from one snowband was significant for the development of another snowband.

These observational studies revealed the mesoscale structures of various

snowbands. However, owing to the limitation of the detectable area of the Doppler radars, the structures of the environmental air such as a land breeze, which affect to the formation and maintenance of snowbands, have not been well clarified in some studies. In order to compensate for lack of observation and to deepen our understanding of the formation and maintenance mechanisms of mesoscale snowfall systems, the numerical approach is an effective method. Some numerical studies have been performed (e.g., Ikawa et al. 1987; Ikawa 1988; Nagata 1993; Takayama and Nagata 1995; Saito et al. 1996). However, the three-dimensional cloud resolving numerical simulations have not been carried out due to the problems in numerical models and computer resources. Therefore, contributions of each process, such as a land breeze, a cold pool, and topographic effects, for the formation and maintenance of snowbands have not been fully investigated.

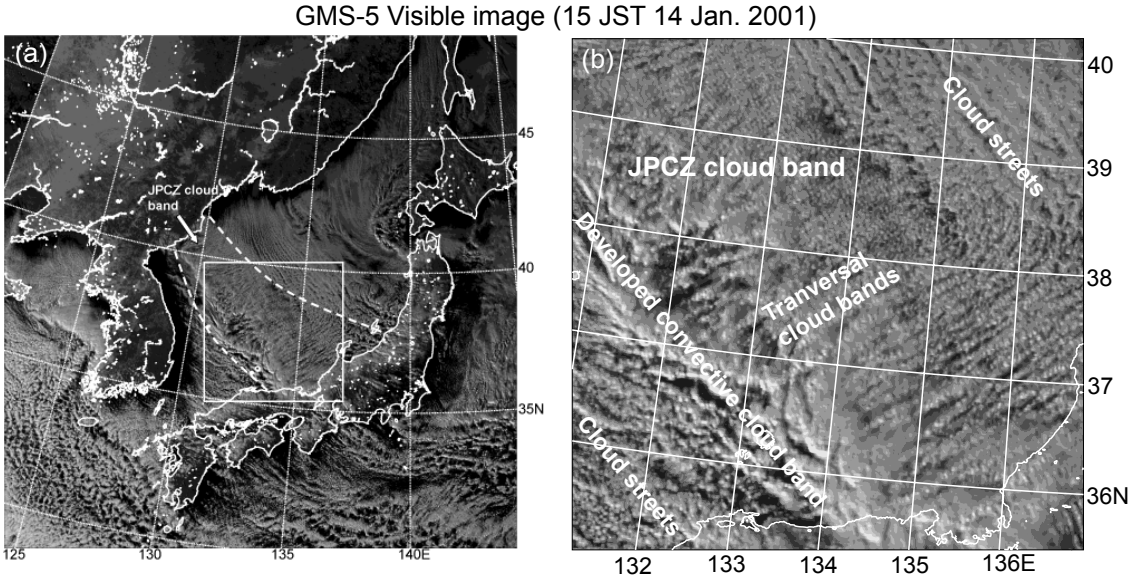


Figure 1.8: GMS-5 visible images at 15 JST on 14 January 2001. The rectangle in (a) corresponds to the display area in (b). Two dashed lines in (a) denote the boundaries of the JPCZ cloud band.

## 1.4 The JPCZ cloud band

The JPCZ cloud band occasionally forms from the base of the Korean Peninsula over the Sea of Japan. As a typical example of the JPCZ cloud band,

the GMS visible image at 15 JST on 14 January 2001 is shown in Fig. 1.8a. The downstream part of the JPCZ cloud band brings heavy snowfalls to the coastal areas of the Japanese Islands (e.g., Okabayashi 1969; Yagi et al. 1986); therefore, many studies have been carried out regarding its formation mechanisms (Nagata et al. 1986; Nagata 1991), movement and intensification (Endoh et al. 1984; Uemura 1980; Nagata 1992; Ohigashi and Tsuboki 2007), and inner structures (Uemura 1980; Hozumi and Magono 1984; Yagi 1985; Yagi et al. 1986; Nagata 1987; Arakawa et al. 1988).

Nagata et al. (1986) and Nagata (1991) investigated the formation mechanisms of the JPCZ cloud band using a hydrostatic numerical model with a horizontal resolution of about 40 km. They revealed that the JPCZ is caused cooperatively by three low-level boundary forcings, i.e., the land-sea thermal contrast between the Korean Peninsula and the Sea of Japan, the blocking effect of the mountains north of the Korean Peninsula, and the characteristic distribution of the sea surface temperature (SST) of the Sea of Japan.

The JPCZ cloud band usually extends southeastward from the base of the Korean Peninsula; however, its downstream part sometimes shifts from the western San-in district to the southern Tohoku district, according to the change of large scale fields (Endoh et al. 1984; Uemura 1980). Nagata (1992) numerically investigated the movement and development of the JPCZ cloud band in the passage of a short-wave trough accompanied by a remarkable cold low. Ohigashi and Tsuboki (2007) clarified the dynamics of the movement and intensification of the JPCZ associated with the upper cold core using a cloud resolving model.

Many studies have been conducted to describe the detailed structures of the JPCZ and the JPCZ cloud band (Uemura 1980; Hozumi and Magono 1984; Yagi 1985; Yagi et al. 1986; Nagata 1987; Arakawa et al. 1988). The mesoscale airflow and thermodynamic structures around the JPCZ were investigated in several case studies, having the following common features (Uemura 1980; Yagi et al. 1986; Nagata 1987). A west-northwesterly airflow with weak vertical wind shear is observed on the southwestern side of the JPCZ. On the northeastern side of the JPCZ, a northerly airflow is dominant in the lower-level. As a result, a convergence line between the northerly and the west-northwesterly forms on the southwestern edge of the JPCZ. A middle-level air above the convergence line flows northeastward over the lower-level northerly airflow, resulting that the

vertical wind shear becomes large on the northeastern side of the JPCZ. The schematic picture of the typical airflow structures around the JPCZ is shown in Fig. 1.9.

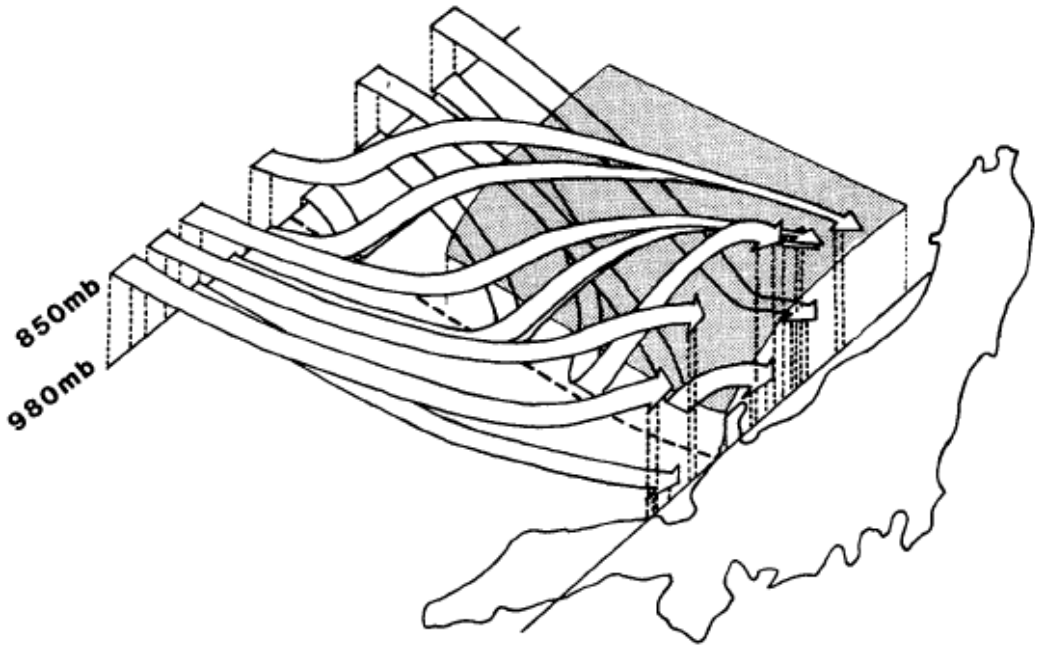


Figure 1.9: Schematic picture of three-dimensional airflow based on the trajectories of air parcels which start from two levels (980 hPa and 850 hPa) over the central part of the Sea of Japan. The shaded surface shows the weak stable layer in cold airmass and the thick dashed line indicates the position of the convergence line with active convection (Nagata 1987).

Figure 1.10 shows a vertical cross section of atmospheric structures around the JPCZ obtained by upper-air soundings. A warm and weak-wind zone is observed on the northeastern side of the convergence line (e.g. Yagi et al. 1986; Nagata 1987; Ohigashi and Tsuboki 2005, 2007). The lower warm and weak-wind zone is induced by the mesoscale updraft along the JPCZ. The updraft generates the vertical transport of horizontal momentum, forming the weak-wind zone in the mixed layer along the JPCZ. The updraft also induces latent heat release. The latent heat release contributes to reducing the surface pressure in the lower layer and maintains the updraft and mesoscale circulation around the JPCZ.

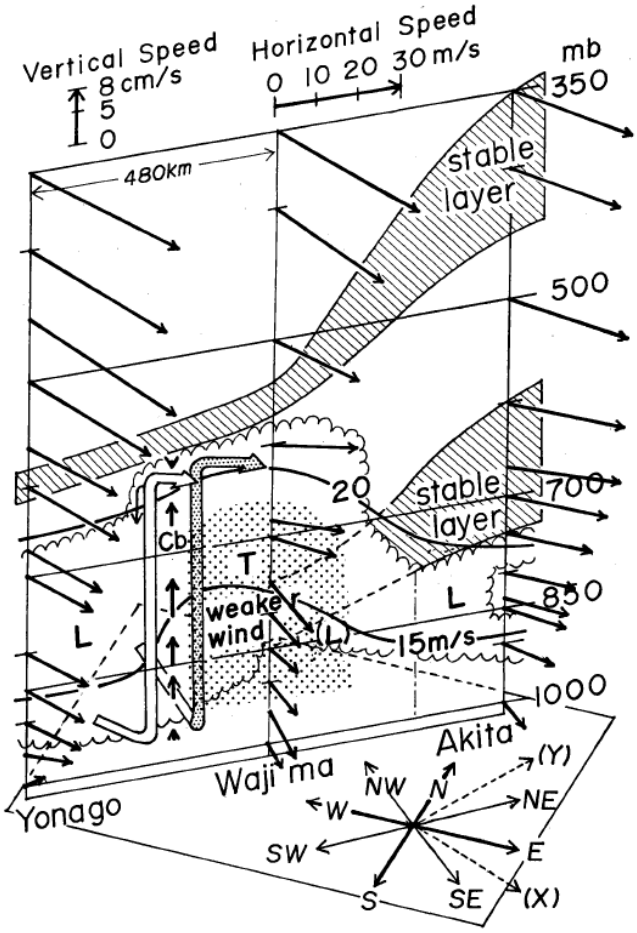


Figure 1.10: Vertical cross section normal to the JPCZ of atmospheric structures obtained by upper-air soundings at Yonago, Wajima, and Akita stations at 21 JST on 2 February 1978. Vectors denote wind velocities. Total wind speed is contoured by solid lines every 5 m $s^{-1}$. A dotted area denotes a relatively weaker-wind zone. Shaded areas indicate stable layers. An area enclosed by spiral lines denotes an area with a dew point depression of less than 2ºC. The symbols "Cb", "L", and "T" denote the area with a developed convective cloud band, longitudinal-mode cloud bands, and transversal cloud bands in the JPCZ cloud band, respectively. Open arrows denote streamlines around the developed convective cloud band (Yagi et al. 1986).

Satellite images show that two types of cloud bands are commonly observed in the JPCZ cloud band; one is a developed convective cloud band (e.g., Yagi et al. 1986) and the others are transversal cloud bands (e.g., Yagi 1985). The developed convective cloud band is found along the southwestern edge of the JPCZ cloud band, where the convergence line forms. A typical example of the

developed convective cloud band is shown in Fig. 1.8b. Yagi et al. (1986) analyzed the GMS images in detail and found that the developed convective cloud band (referred to as “Cu-Cb line” in Yagi et al. 1986) was located on the line of the maximum horizontal wind shear at cloud level. They also showed that the cloud top heights of the developed convective cloud band were tallest in the JPCZ cloud band. These features of the developed convective cloud band are in common with those shown by the other studies.

The transversal cloud bands, whose orientation is normal to the wind direction of the winter monsoon, extend to the northeast from the developed convective cloud band. They form on the northeastern side of the JPCZ, where the vertical wind shear is large. A typical example of the transversal cloud bands is also shown in Fig. 1.8b. Yagi (1985) and Yagi et al. (1986) analyzed GMS images and upper-air sounding data, and indicated that the axes of the transversal cloud bands were parallel to the vertical wind shear vector of horizontal winds. In addition, applying the linear theory of thermal instability in the vertical shear flow (Asai 1970a, 1970b, and 1972), Yagi (1985) proposed that the transversal cloud bands were produced from longitudinal-mode (shear-parallel mode) roll convections. Shimizu and Tsuboki (2005) analyzed the transversal cloud band near the coast of the western Hokuriku district on the basis of dual-Doppler radar observations. They showed that the transversal cloud band consisted of convective clouds, and that its axis was parallel to the vertical wind shear vector of horizontal winds.

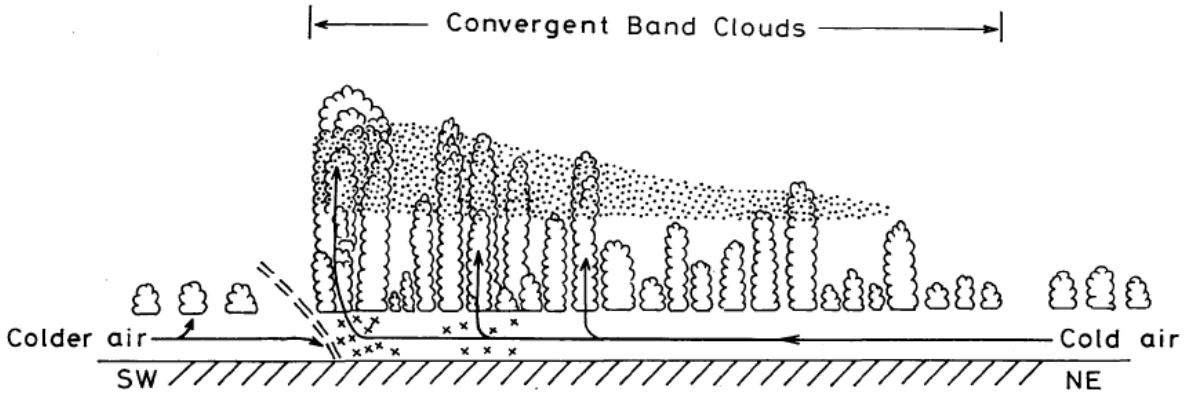


Figure 1.11: Conceptual model of the vertical structures of the JPCZ cloud band observed from 28 February to 1 March 1979. Vertical cross section normal to the JPCZ cloud band is displayed (Hozumi and Magono 1984).

On the other hand, Hozumi and Magono (1984) made another conceptual model of the transversal cloud bands in the JPCZ cloud band, on the basis of the analysis of cloud photographs taken from an aircraft. The vertical structure of their proposed conceptual model of the JPCZ cloud band (referred to as "Convergent band clouds" in Hozumi and Magono 1984) is shown in Fig. 1.11. They suggested that the transversal cloud bands were mainly stratiform clouds, which extend northeastward from the developed convective cloud band. An analysis with upper-air soundings from a research vessel across the JPCZ was made by Arakawa et al. (1988). They also suggested that the transversal cloud bands were mainly stratiform clouds, which could be maintained by water substance supply from the southwestern side of the JPCZ and slow upward motion. On the basis of numerical simulation results and observational data, Nagata (1987) analyzed the mesoscale structure of the JPCZ cloud band using a hydrostatic numerical model. His analysis showed that a wet region is located in the middle-level on the northeastern side of the line of active convection, that is, the developed convective cloud band. As supposed by Hozumi and Magono (1984) and Arakawa et al. (1988), he expected that transversal cloud bands are stratiform clouds generated in the wet region, but he could not confirm that directly, because the numerical model used in Nagata (1987) did not have hydrometeors as prognostic variables.

As mentioned above, the structure and formation mechanism of the transversal cloud bands are not yet clear. The above-mentioned observational and analytical studies were mainly based on sparse data over the Sea of Japan, except for satellite images and dual-Doppler radar observations. The satellite image is usually used in two-dimensional analyses in a horizontal plane. On the other hand, Doppler radar, which usually operates at C-band or X-band, can show three-dimensional kinematic structures of mesoscale precipitation systems. However, it can not detect cloud particles whose size is 100-1000 times smaller than that of precipitation particles, and besides Doppler radar observations are usually limited near the coastal region. The cloud profiling radar (CPR), which presently operates at Ka-band or W-band, is sensitive enough to detect cloud particles. To capture the characteristics of the transversal cloud bands, it is necessary to conduct observations over the sea using the CPR. In order to compensate for sparse observational data, the numerical approaches have been effectively performed (e.g., Nagata 1987). However, the previous numerical

studies were based on simulation results of a coarse mesh model with a horizontal resolution of several tens of kilometers. Such a model cannot resolve the cloud bands over the Sea of Japan during cold air outbreaks with a spacing of 5-20 km (e.g., Miura 1986). To resolve and investigate the transversal cloud bands, it is necessary to conduct cloud resolving experiments by a fine mesh model with a horizontal resolution of a few kilometers or less.

## 1.5 Outline of the field campaign and cloud-resolving model

As shown in the previous sections, many studies have been made on snowbands and the JPCZ cloud band. However, their inner structures and the formation and maintenance mechanisms are not well understood, because these scales in time and space are too small to clarify them using routine or conventional observations and numerical weather prediction models. In this thesis, the author investigates them closely using data provided by high-resolution special observations of a field campaign and simulation results of a high-resolution cloud-resolving model. Outlines of the related field campaign and cloud-resolving model to this thesis are described in the following subsections.

### 1.5.1 Field campaign

In order to understand the formation and development mechanisms of mesoscale snowfall systems, a field campaign, named “Winter MCSs Observations over the Japan Sea in 2001” (referred to as “WMO-01”, Yoshizaki et al. 2001), was conducted over the Sea of Japan surrounding the Hokuriku district in 2001. High-resolution radar observations such as an airborne CPR, Doppler radars, and boundary layer radars (BLRs) were conducted in the WMO-01. In order to capture the detailed structures of MCSs around the coastal region, observation network of Doppler radars covered the coastal region of Hokuriku district. In addition to upper-air soundings, BLR observations were also conducted to capture the characteristics of the environmental field in and around the cloud bands.

In addition to the ground-based observations, three observation vessels were operated, which carried out upper air-soundings over the Sea of Japan. Two observation aircrafts were also operated over the Sea of Japan. Dropsonde

soundings and in-situ cloud observations were conducted by the airplanes. Additionally, airborne CPR and Doppler radar observations were conducted to capture the detailed structures of cloud bands over the Sea of Japan.

### 1.5.2 Cloud-resolving model

Cloud-resolving models (CRMs) are powerful tools for understanding of MCSs. CRMs are usually nonhydrostatic models with sophisticated cloud microphysics; therefore, they can carry out high-resolution numerical experiments to achieve the cloud dynamical reproduction of MCSs. In this thesis, a CRM, the Japan Meteorological Agency (JMA) nonhydrostatic mesoscale model (referred to as JMA-NHM) is used to simulate observed cloud bands.

The JMA-NHM is a community model for operation and research. The JMA has used this model for operational mesoscale numerical weather prediction around Japan since 1 September 2004 (Saito et al. 2006). Since March 2006, the resolution has been improved from 10 km horizontally with 40 vertical layers to 5 km with 50 layers (Saito et al. 2007). The JMA-NHM was initially developed in the Meteorological Research Institute (MRI) as a research tool for small scale phenomena such as convection or nonlinear mountain waves (Ikawa and Saito 1991). Various modifications have extended the model to a full-scale mesoscale model to realistically simulate mesoscale phenomena (Saito et al. 2001). Many studies have used this model to study real mesoscale systems, which are mainly heavy rainfall events in the warm season (e.g., Kato 1998; Seko et al. 1999; Yoshizaki et al. 2000; Kato and Goda 2001).

## 1.6 Purpose and contents of the thesis

During the WMO-01, snowbands were frequently observed around the coastal region of the Hokuriku district. The JPCZ cloud bands also frequently formed over the Sea of Japan, extending from the base of the Korean Peninsula to the Hokuriku and San-in districts. They brought heavy snowfalls to the coastal region of the Hokuriku and San-in districts. These cloud bands were captured by Doppler radars and an airborne CPR. The characteristics of the environmental field in and around the cloud bands were also observed with BLRs and upper-air soundings. In addition, numerical experiments with a horizontal resolution of 1 km were performed with the use of the JMA-NHM. The JMA-NHM

successfully reproduced observed characteristics of the cloud bands.

The purpose of this thesis is to clarify the characteristics, the kinematic and thermodynamic structures, and the formation and maintenance mechanisms of the cloud bands observed during the WMO-01, by analyzing data provided by the special observations of the WMO-01 and the simulation results of the high-resolution JMA-NHM. Special attention will be given to the inner structure and the maintenance mechanism of the snowband. The effect of a cold pool, produced under the snowband, on the maintenance process of the snowband will be investigated. Moreover, the structure and the formation mechanism of transversal cloud bands in the JPCZ cloud band will be also investigated. The role of the transversal cloud bands in the formation and maintenance of the snowband will be discussed.

The contents of this thesis are as follows.

In Chapter 2, an outline of the field campaign WMO-01 is presented. Various observation facilities and their operations are reported. An overview of the heavy snowfall during the period of 12–17 January 2001 is also presented.

In Chapter 3, a quasi-stationary snowband observed on 16 January 2001 is analyzed on the basis of observations (e.g., Doppler radars, BLRs, and upper-air soundings) and the simulation results of the JMA-NHM with a horizontal resolution of 1 km. The inner structure and the maintenance mechanism of the snowband are focused. This chapter is based on Eito et al. (2005). The author participated in the WMO-01 and contributed to carry out the field campaign. The author conducted upper-air soundings in the WMO-01, collecting upper-air sounding data used in the article. Numerical experiments using the JMA-NHM were entirely performed by the author. The author conducted the whole analysis of observation data and simulation results in Eito et al. (2005).

In Chapter 4, the JPCZ cloud band observed on 14 January 2001 is analyzed. The structure and the formation mechanism of the transversal cloud bands associated with the JPCZ cloud band are examined on the basis of observations (e.g., satellite images, in-situ measurement and CPR data from an instrumented aircraft, and upper-air soundings from observation vessels) and the simulation results of the JMA-NHM with a horizontal resolution of 1 km. This chapter is based on Eito et al. (2010). The author performed numerical experiments in cooperation with coauthors. The author conducted the whole analysis of observation data and simulation results in Eito et al. (2010).

In Chapter 5, the present snowband is compared with the other snowbands investigated in the previous studies. The relation between the JPCZ cloud band and the snowband is also discussed. Special attention will be given to the role of the transversal cloud bands associated with the JPCZ cloud bands in the formation and maintenance of the snowband.

The conclusions of this thesis are presented in Chapter 6.

# Chapter 2

# Overview of the field campaign “Winter MCSs Observations over the Japan Sea in 2001”

## 2.1 Outline of the field campaign

Figure 2.1 shows maps of the WMO-01. The operations of observation facilities during the WMO-01 are summarized in Fig. 2.2. During the whole observation period (12 January–1 February, 2001), ground-based observations were continuously conducted with Doppler radars operated at C-band (at Goishigamine) or X-band (at Kashiwazaki, Joetsu, Oumi, Oshimizu, Kawakita, Mikuni, and Obama), BLRs (at Fukushima, Maebashi, Joetsu, Toyama, and Mikuni), an upper-air sounding (at Joetsu), and a microwave radiometer (at Joetsu).

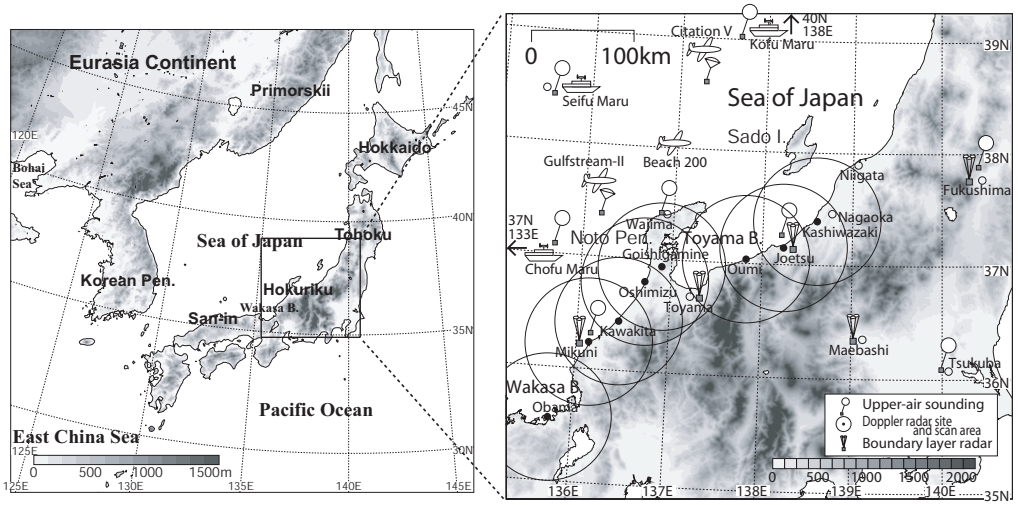


Figure 2.1: Maps of the field observation of WMO-01.

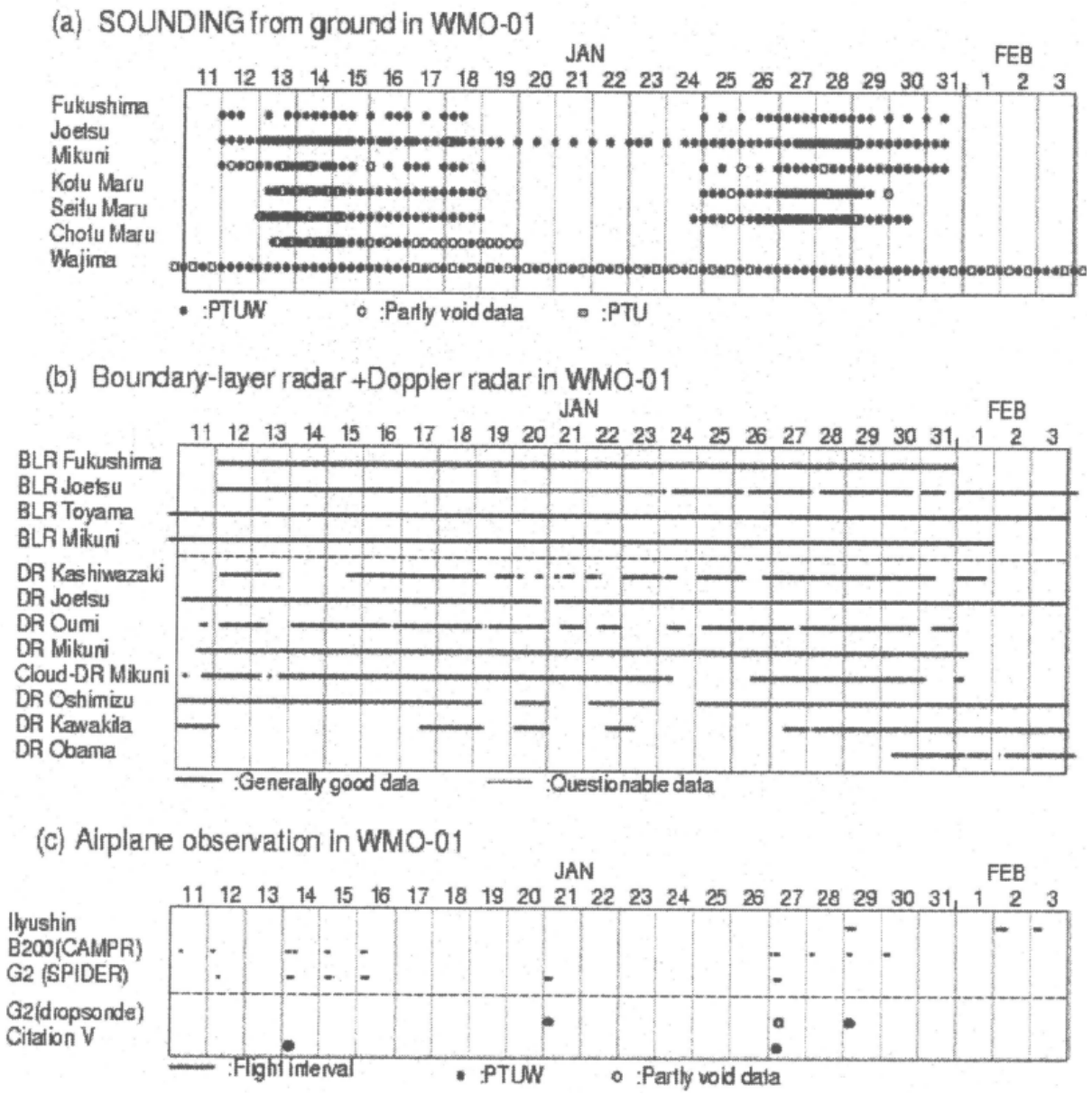


Figure 2.2: Observations during the WMO-01 period with (a) upper-air soundings from surface, (b) boundary layer radars (BLRs) and Doppler radars (DRs), and (c) airplanes (Ilyshin, Beach 200 (B200), Gulfstream-II (G2) and Citation V) (Yoshizaki et al. 2001).

During two intensive observation periods (IOP1, 12–19 January; IOP2, 25 January–1 February), three instrumented aircrafts (Gulfstream-II, Beach 200, and Citation V) were operated over the Sea of Japan. Dropsonde soundings

(Gulfstream-II and Citation V) and in-situ cloud observations (Gulfstream-II) were carried out by the aircrafts. Additionally, an airborne CPR (referred to as "SPIDER"; Horie et. al 2000) was mounted on the Gulfstream-II. An airborne Doppler radar (referred to as "CAMPR"; Kumagai et. al 1996) was mounted on the Beach 200. Boundary-layer observations by a Russian airplane (Ilyushin) were also made on the Russian side of the Sea of Japan.

Over the Sea of Japan, three observation vessels (Chofu-Maru, Seifu-Maru, and Kofu-Maru) were also operated by the JMA, which carried out upper-air soundings every 3 or 6 hours during two intensive observation periods. Upper-air soundings at two additional ground-based sites (at Fukushima and Mikuni) were also conducted.

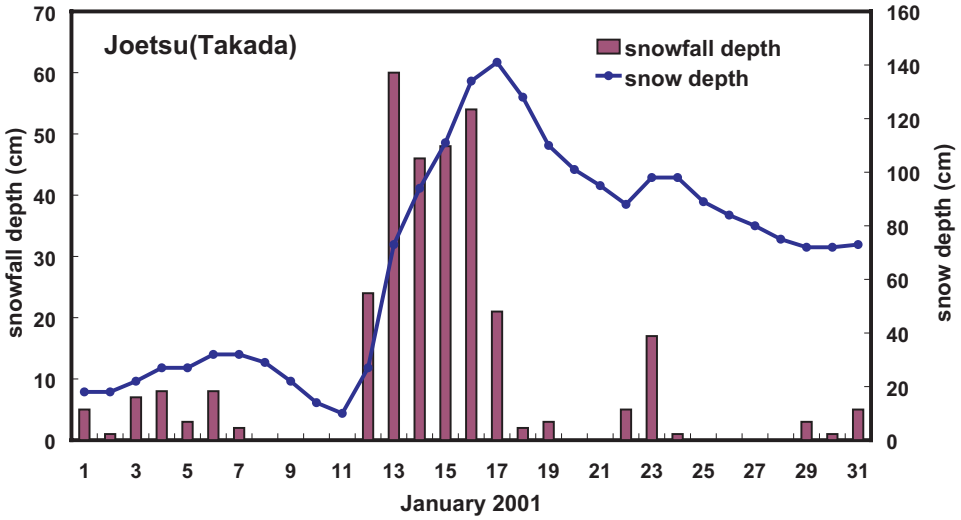


Figure 2.3: Time series of daily snowfall depth (red bars) and snow depth (blue dots) at Takada weather station (in Joetsu city) in January 2001.

## 2.2 Overview of the heavy snowfalls during the period of 12–17 January 2001

A cold air outbreak dominated during the period of 12–17 January 2001. Heavy snowfalls attacked the Hokuriku and San-in districts. Such heavy snowfalls have not occurred there in the past decade or so. Figure 2.3 shows time series of daily snowfall depth and snow depth at Joetsu located in the eastern part of the Hokuriku district. Intense snowfall with a daily snowfall

depth of over 20 cm began on 12 January 2001. It continued about 6 days, resulting that snow depth increased from 10 cm on 11 January to 141 cm on 17 January. After 18 January 2001, no remarkable snowfall was observed.

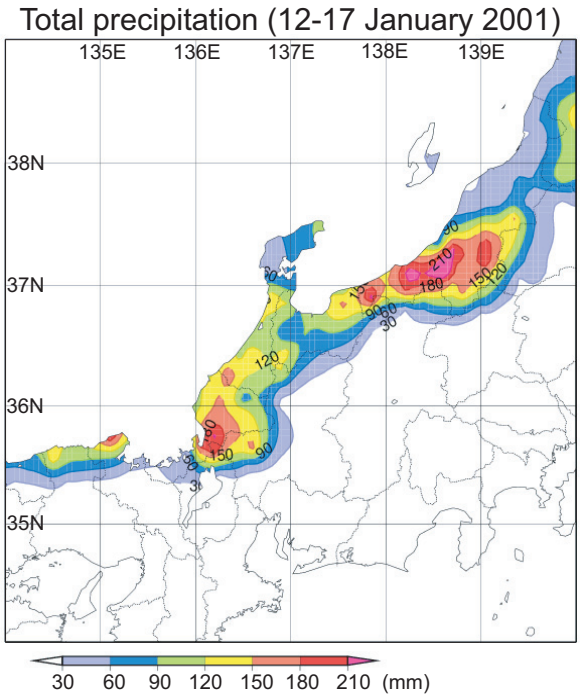


Figure 2.4: Horizontal map of total precipitation amount during the period of 12–17 January 2001.

Figure 2.4 shows the horizontal map of total precipitation amount during the period of 12–17 January 2001. The maximum precipitation zone extends east-northeast–west-southwest in the southern part of the Niigata prefecture. Large precipitation areas also exist in the costal region of the Hokuriku and San-in districts, indicating that heavy snowfalls mainly occurred in the coastal plain area. The heavy snowfalls were mainly caused by mesoscale cloud bands such as snowbands and the JPCZ cloud band, as already shown in Fig. 1.3.

Figure 2.5 shows the temporal variation of precipitation intensity estimated by the JMA operational radar along 138ºE during the period of 12–16 January 2001. Precipitation is observed in the coastal area (around 37ºN) almost throughout the period. Precipitation appears to be periodically intensified at an interval of ~1 day. Each intensified precipitation continues for ~0.5 day, corresponding to the

periodical formation and maintenance of snowbands and development of the JPCZ cloud band.

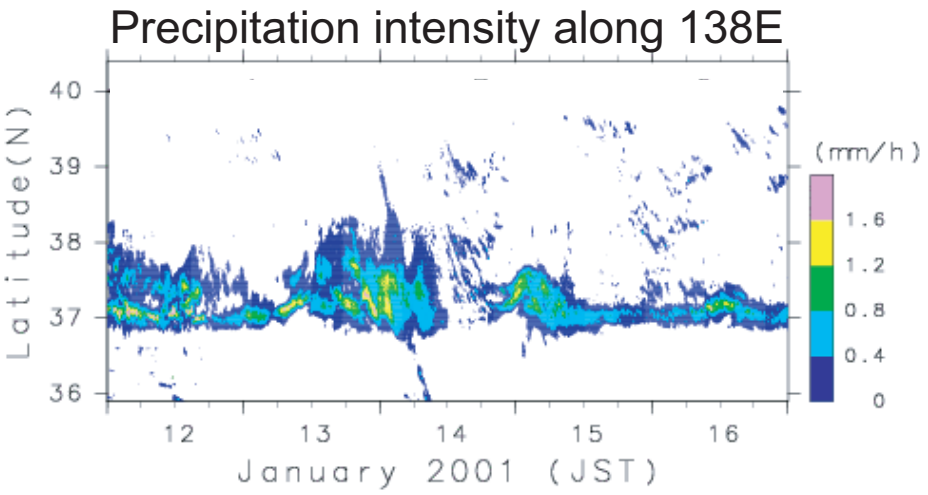


Figure 2.5: Time-latitude cross section of precipitation intensity observed by the JMA Niigata operational radar along 138ºE during the period of 12–16 January 2001.

In order to present the large scale situation of the heavy snowfalls, fields of sea level pressure, surface wind, and temperature at 925 hPa at 09 JST on 14 January 2001 are shown in Fig. 2.6a. Between a developed cyclone over the Pacific Ocean and a high-pressure zone over the continent, the contours of sea level pressure (thin lines) around Japan lie in a south–north direction. This pressure pattern often appears during the winter monsoon season. The surface winds (vectors) flow normal to the isothermal lines (bold dashed lines) near the surface (at 925 hPa) over the Sea of Japan, indicating that there is an outbreak of cold air from the Eurasian Continent over the Sea of Japan. However, the contour interval of sea level pressure is broader over the Sea of Japan; therefore, the winds in this area are not so strong.

Fig. 2.6b shows fields of geopotential heights, winds, and temperature at 500 hPa. Both geopotential heights and temperature fields indicate synoptic-scale features of a cold trough in eastern Asia, showing that a cold air mass with the temperature less than –35ºC covers most of the Sea of Japan. The polar jet is seen on the southern side of the Sea of Japan, suggesting that positive vorticity areas, which are located on the northern side of the jet axis, cover over the Sea of Japan. This upper-level trough was quasi-stationary over the Sea of Japan

during the heavy snowfall period of 12–17 January 2001. This situation is similar to that on P-type heavy snowfalls described in Akiyama (1981a, 1981b).

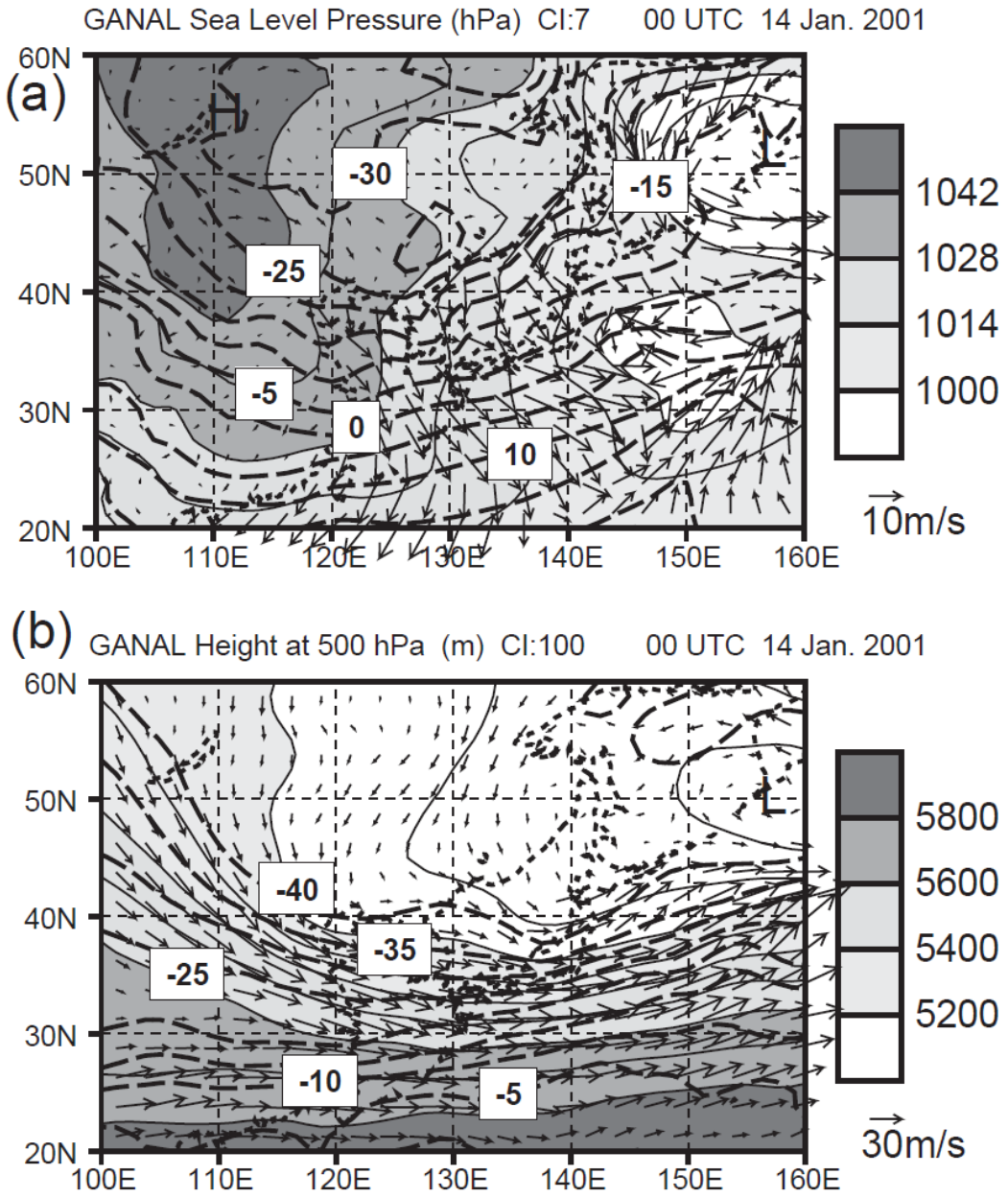


Figure 2.6: (a) Sea level pressure, surface wind, and temperature (925 hPa) fields, and (b) geopotential height, wind, and temperature fields at 500 hPa at 09 JST on 14 January 2001. Contour lines of temperature are drawn every 5ºC by dashed lines (Yoshizaki et al. 2004).

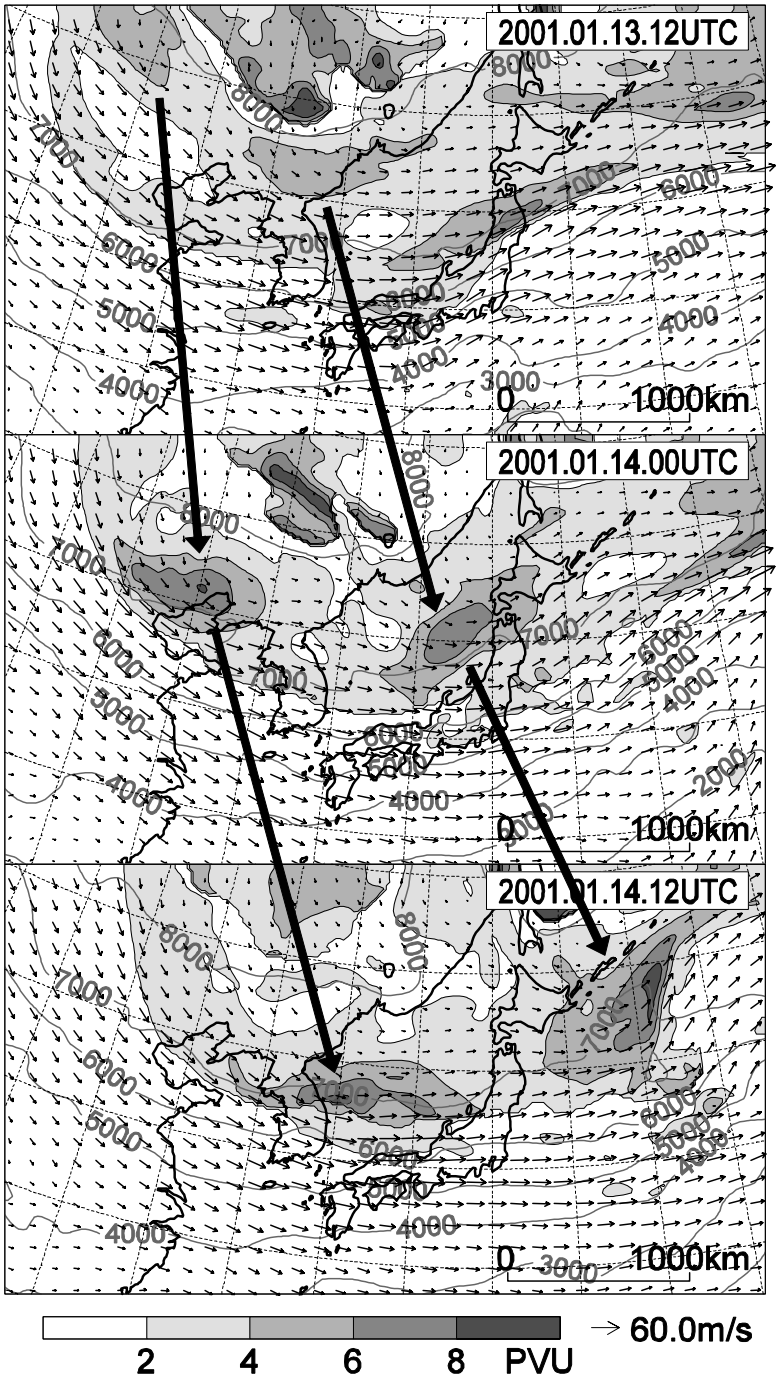


Figure 2.7: Time series of isentropic charts on $\theta = 300$ K during the period from 21 JST 13 to 21 JST 14 January 2001. High PV areas (> 2 PVU) are shaded every 2 PVU ($1\text{PVU} \equiv 10^{-6}\,\text{m}^2\,\text{K}\,\text{s}^{-1}\,\text{kg}^{-1}$); geopotential height is contoured by solid lines every 1000 m; thin arrows show horizontal wind velocities. PV anomalies are traced by bold arrows (Yoshizaki and Kato 2005).

To examine features of the vorticity distribution, the isentropic potential vorticity (PV) is introduced instead. The isentropic charts of PV and geopotential height at a potential temperature ($\theta$) of 300 K around 14 January 2001 are shown in Fig. 2.7. It is noticed that the primary synoptic-scale trough did not change much; however, additional 1000-km size PV anomalies propagated eastward repeatedly along the northern side of the jet. The PV anomalies resemble those associated with medium-scale tropopausal waves (e.g., Sato et al. 1993; Hirota et al. 1995; Yamamori et al. 1997; Yamamori and Sato 1998; Sato et al. 2000; Yamamori and Sato 2002) in their horizontal scale, period, and location. A moving upper-level PV anomaly, which is often referred to as a short-wave trough, induces decrease of static stability below and in front of it (e.g., Hoskins et al. 1985; Ogura 2000). Therefore, it sometimes tends to generate various types of mesoscale disturbances in the lower atmosphere over the Sea of Japan, such as the formation and maintenance of snowbands and the intensification of the JPCZ cloud band, as shown in this case.

In summary, P-type heavy snowfalls occurred over the coastal region of the Hokuriku and San-in districts during the period of 12–17 January 2001, when an upper-level synoptic-scale trough was quasi-stationary over the Sea of Japan. Mesoscale disturbances such as snowbands and the JPCZ cloud band periodically formed and developed under the affect of moving upper-level PV anomalies, causing heavy snowfalls to the coastal plain areas. In the following chapters, in order to understand the detailed process of the heavy snowfalls caused by snowbands and the JPCZ cloud band, the structure and the formation and maintenance mechanisms of them are analyzed in typical cases during the heavy snowfall period of the WMO-01. A quasi-stationary snowband observed on 16 January 2001 is focused in Chapter 3. The JPCZ cloud band observed on 14 January 2001 is investigated in Chapter 4.

# Chapter 3

# Formation and maintenance mechanisms of the quasi-stationary snowband on 16 January 2001

## 3.1 Introduction

On 16 January 2001, during the WMO-01, a remarkable snowband formed in the coastal area of the eastern Hokuriku district. The snowband stagnated for about half a day and caused about 50 cm snowfall in this area. Such a snowband was often observed in almost the same place during the WMO-01, bringing a heavy snowfall. Thus, it is required to clarify the mechanism of the snowband for an understanding of the characteristics of snowfalls in this region.

The purpose of this chapter is to examine the detailed structures of the snowband and the environmental air for an understanding of the formation and maintenance mechanisms of the snowband, by analyzing on the basis of observations (e.g., Doppler radars, BLRs, and upper-air soundings) and the simulation results of the JMA-NHM with a horizontal resolution of 1 km. Special attention will be given to the role and formation mechanism of a cold pool under the snowband. Characteristics of the snowband observed by radar are shown in Section 3.2. Environmental fields around the snowband are examined in Section 3.3. In Section 3.4, a description of the JMA-NHM used in this study is given. The design of the numerical experiment is also presented. The structures of the snowband are examined on the basis of the simulation results of the JMA-NHM in Section 3.5. The effect of a cold pool, produced under the snowband, on the maintenance process of the snowband are discussed in Section 3.6. The conclusions are presented in the last section.

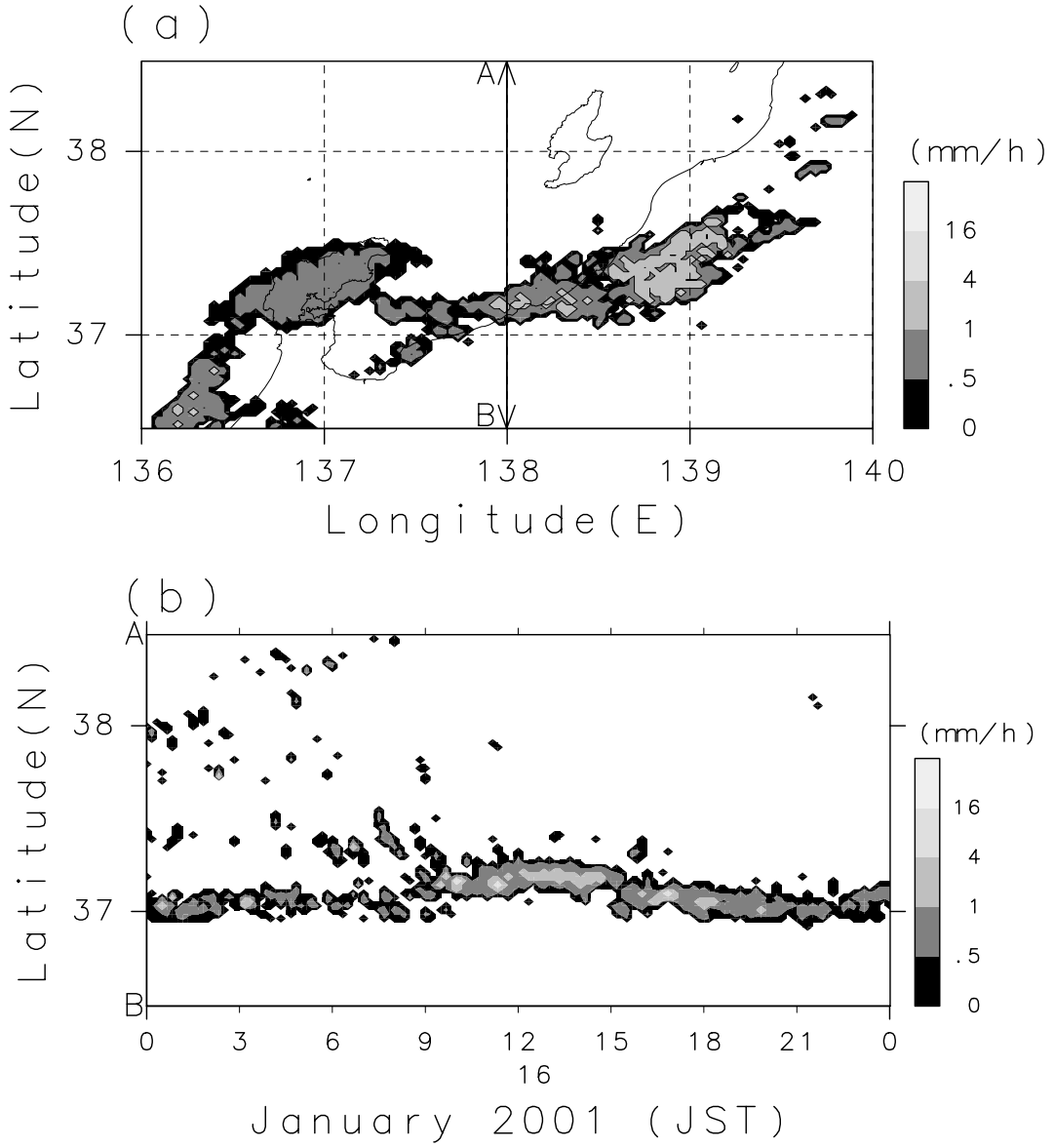


Figure 3.1: (a) Horizontal distribution of precipitation intensity observed by the JMA Niigata operational radar at 1400 JST on 16 January 2001. (b) Time-latitude cross section of precipitation intensity along 138ºE (line A–B in (a)).

## 3.2 Characteristics of the snowband

Figure 3.1a shows the horizontal distribution of hourly precipitation intensity estimated by the JMA operational radar at 1400 JST on 16 January 2001. A snowband with a length of about 150 km, and a width of about 50 km, is found

lying eastward from Toyama Bay. Figure 3.1b shows the temporal variation of precipitation intensity along 138ºE (line A–B in Fig. 3.1a). Weak precipitation is observed until around 09 JST in the coastal area. Precipitation is intensified off the coast around 09 JST, when the snowband formed. Intensified precipitation appears for approximately half a day, denoting that the snowband lasted. It is noticed that the snowband slightly moved from the north to south.

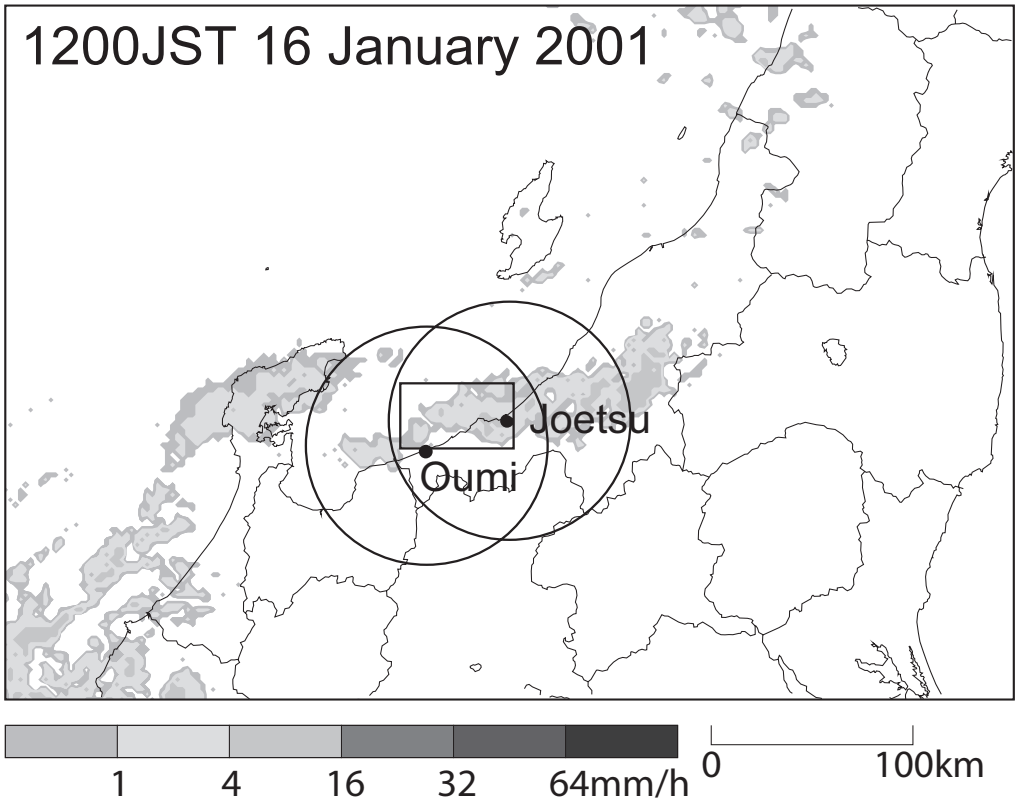


Figure 3.2: Locations of the NIED Doppler radars (Oumi and Joetsu), the area of quantitative radar observation (shown by two circles), and a map of the observation area. The maximum range circles are at 64 km from each radar. The distance between two radars is 37.6 km. Prefectural boundaries are shown by solid lines in the map. The box corresponds with the radar display area shown in Fig. 3.3. The shaded regions indicate precipitation areas observed by the JMA Niigata radar at 1200 JST on 16 January 2001.

The snowband was also captured by a dual-Doppler radar system (Kusunoki et al., 2002). Figure 3.2 shows the radar sites and the detective areas of radar

observation. The two X-band Doppler radars of the National Research Institute for Earth Science and Disaster Prevention (NIED) were operated at Oumi and Joetsu. Figure 3.3a shows the radar reflectivity pattern observed by the Oumi radar at an altitude of 0.2 km at 1206 JST on 16 January 2001. As illustrated in Fig. 3.3a, the present snowband contains several cellular radar echoes with a horizontal scale of a few km. Cellular radar echoes, with a maximum reflectivity of about 30 dBZ (defined as ‘‘band B’’ by Kusunoki et al. 2002), are observed at the northern edge of the snowband (defined as ‘‘band A’’ by Kusunoki et al. 2002). Horizontal wind velocities obtained by the dual-Doppler analysis are also shown in Fig. 3.3a. Northwesterly winds of the winter monsoon are observed to the north of the snowband, and they produce the convergence at the northern edge of the snowband, with weaker westerly or west-northwesterly winds inside the snowband. Figure 3.3b shows the band-normal vertical structure of radar reflectivity and airflows. While the width of band B is narrower than that of band A, the echo top of band B is higher than that of band A. Moreover, the intensity of radar reflectivity in band B is stronger than that in band A. An updraft zone is analyzed in the region of band B, corresponding to the low-level horizontal convergence zone. The time series of the dual-Doppler observation (not shown) present that band B was generated at the northern edge of pre-existent band A. While band A gradually weakened and dissipated, band B developed and moved east-southeastward. This indicates that a regeneration of the snowband occurred.

Some characteristics of the snowband presented by Kusunoki et al. (2002) were generally observed in the dual-Doppler observation. They are as follows: 1) The snowband contained several cellular radar echoes with a horizontal scale of a few km, and it propagated east-southeastward. 2) A horizontal convergence and an updraft zone were observed at the northern edge of the snowband, where new cellular radar echoes formed. However, the regeneration of the snowband shown by Kusunoki et al. (2002) was so drastic that such an event was not constantly observed through the Doppler observation. In contrast, it was mainly observed that cellular echoes with lower reflectivity around the northern edge of the snowband tended to develop gradually, as they moved east-southeastward.

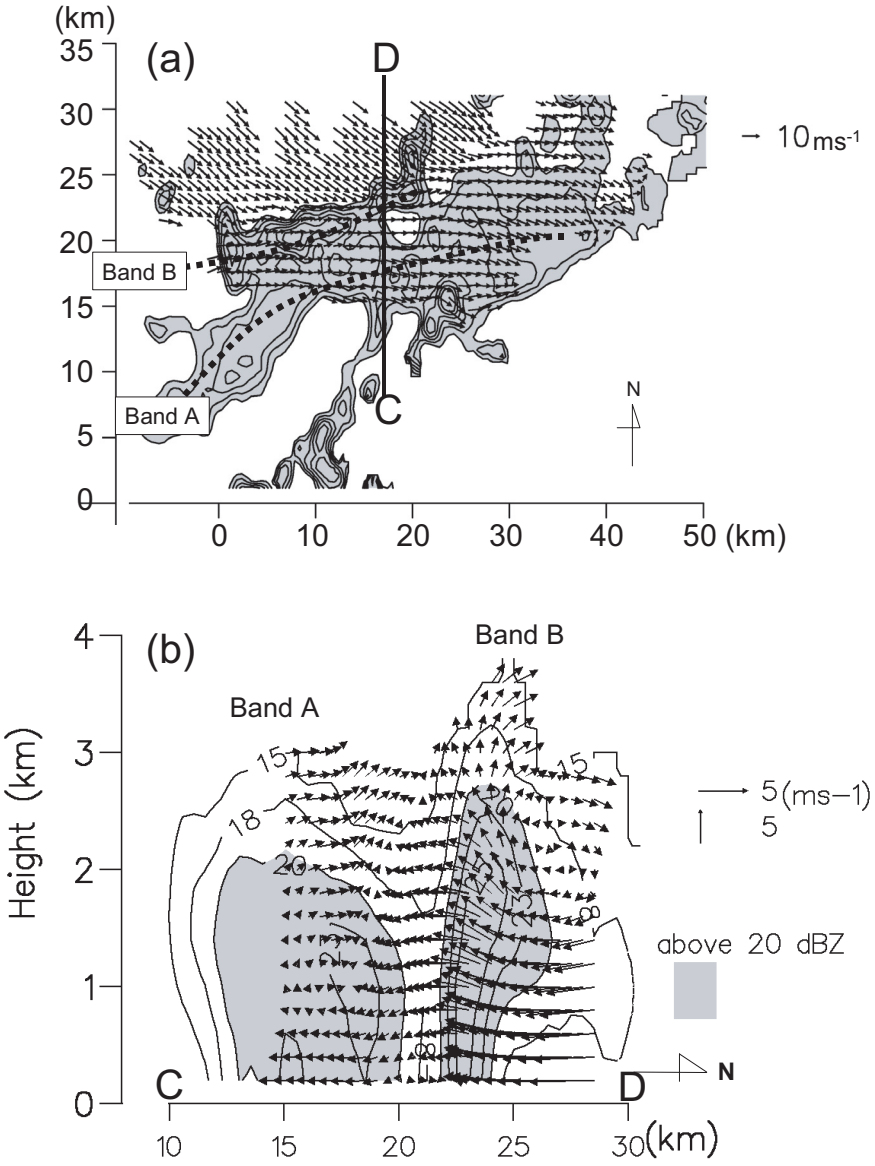


Figure 3.3: (a) Radar reflectivity pattern (shaded and contoured regions) and horizontal wind velocity (arrows) at an altitude of 0.2 km at 1206 JST. Reflectivities are shaded above 20 dBZ and contoured every 3 dBZ above 20 dBZ. Bold dashed lines indicate the locations of band A and B, respectively. A bold solid line C–D shows the line along which the vertical cross section shown in (b) (Kusunoki et al. 2002). (b) Radar reflectivity (shaded and contoured regions) and airflow (arrows) in vertical cross section along the bold solid line C–D in (a). Reflectivities are shaded above 20 dBZ and contoured above 15 dBZ (Kusunoki et al. 2002).

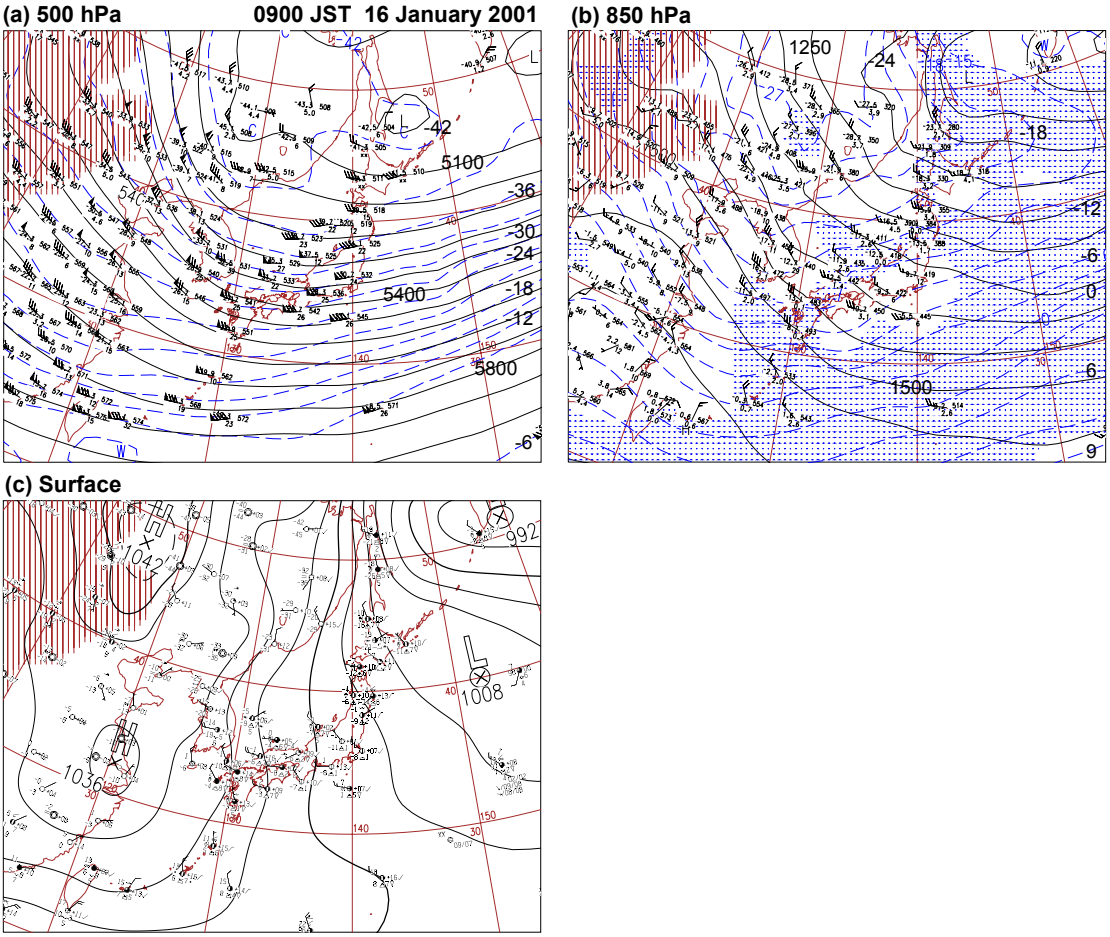


Figure 3.4: Weather maps provided by JMA at 0900 JST on 16 January 2001. (a) At 500 hPa, geopotential height is contoured by solid lines every 60 m; temperature is contoured by dashed lines every 3ºC. (b) At 850 hPa, geopotential height is contoured by solid lines every 50 m; temperature is contoured by dashed lines every 3ºC; the wet areas (T−Td < 3ºC) are dotted. (c) At the surface, pressure is contoured by solid lines every 4 hPa. Half-barb, one full barb, and triangle-shaped barb mean 5 knots, 10 knots, and 50 knots, respectively.

## 3.3 Environmental field around the snowband

Figure 3.4 shows weather maps at 0900 JST on 16 January 2001. A cold air outbreak from the Eurasian Continent had continued for 5 days at that time. At a level of 500 hPa (Fig. 3.4a), a cold air mass, with the temperature less than –33ºC, exists over the Hokuriku district. At a level of 850 hPa (Fig. 3.4b), the

isometric lines (solid lines) are almost normal to the isotherms (dashed lines) over the Sea of Japan. These features denote that the advection of a cold air tended to be induced in this area. There are two remarkable cold airflows, one from Primorskii (see Fig. 2.1) to the northern part of Japan, and the other from the Korea Peninsula to the western part of Japan. The contours of sea level pressure around Japan lie in a south-north direction (Fig. 3.4c). This pressure pattern often appears during the winter monsoon. The contour interval, however, is broader around the Hokuriku District; therefore, the winds in this area are not so strong. For example, a northwesterly surface wind at a speed of about 5 m $s^{-1}$ is observed at Wajima (see Fig. 2.1). Around the Hokuriku District, these pressure and temperature patterns are also analyzed at 2100 JST (not shown). This indicates that such large-scale atmospheric conditions lasted during the occurrence of the snowband.

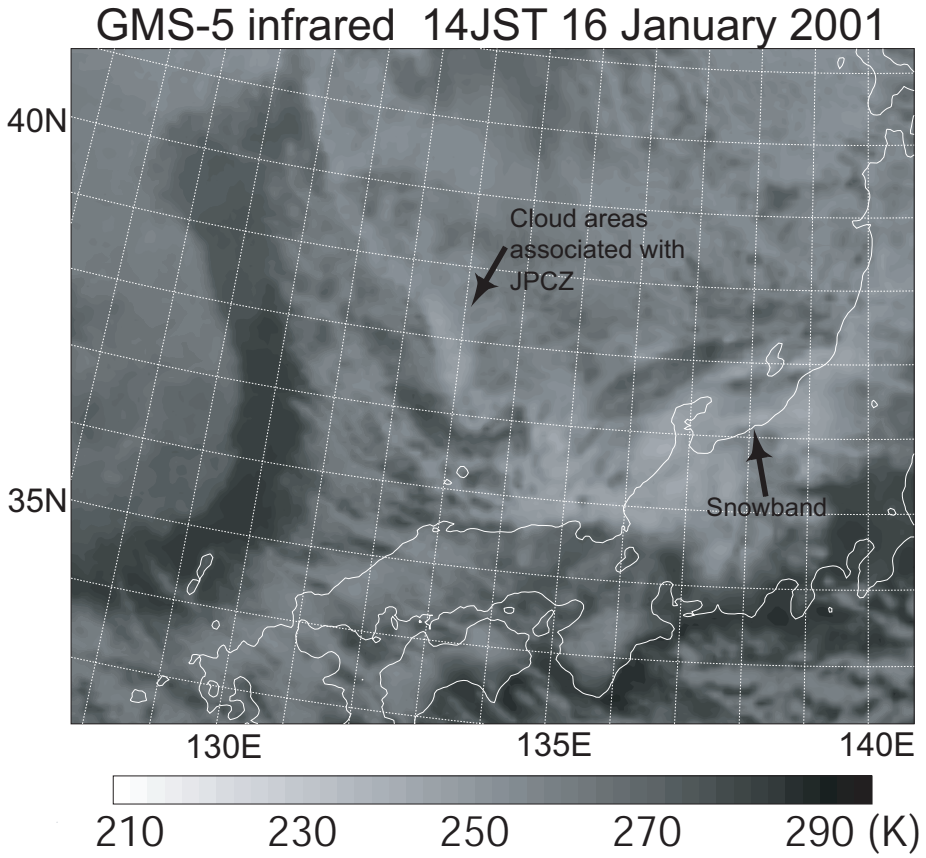


Figure 3.5: GMS-5 infrared image at 14 JST on 16 January 2001. The white solid lines show the seashore of Japan.

Figure 3.5 shows the GMS-5 infrared image at 14 JST. Several clouds are found over the Sea of Japan. They are caused as a consequence of heat and moisture supply from the relatively warm sea to the continental cold air mass. The areas with low brightness temperature, where cumulus convections develop, are distributed over the Sea of Japan from the base of the Korean Peninsula to Wakasa Bay. These cloud areas correspond to the developed convective cloud band in the JPCZ cloud band (see section 1.3). The areas with developed convections are also found around the Hokuriku district, corresponding to the present snowband. It is also shown that the snowband forms on the downstream side of the transversal cloud bands in the JPCZ cloud band (see section 1.3).

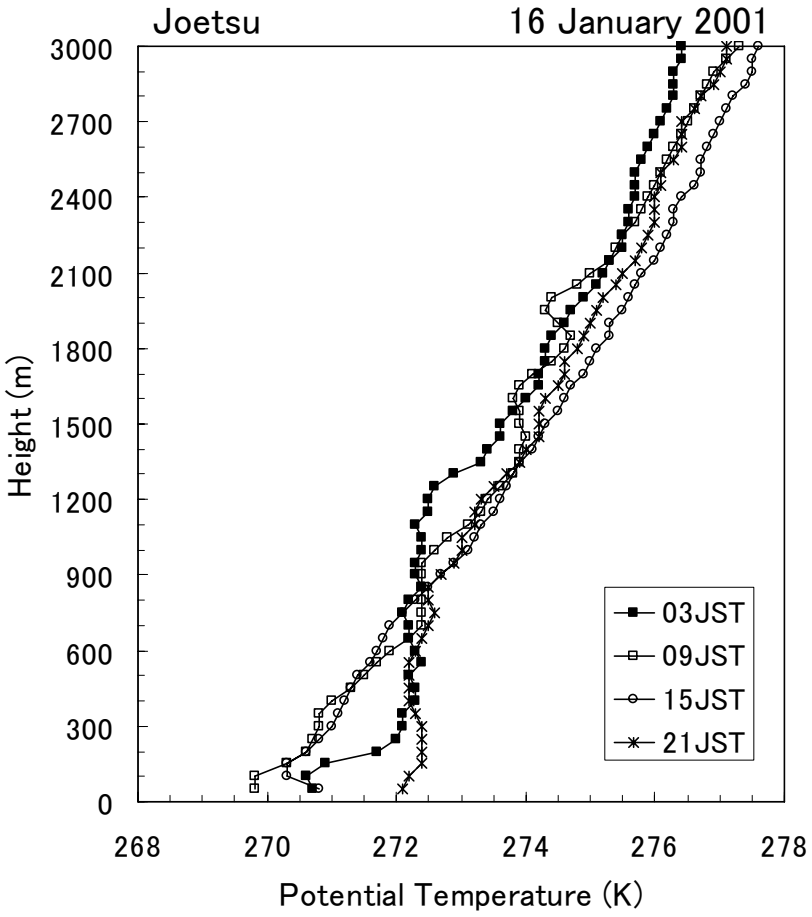


Figure 3.6: Vertical profiles of potential temperature ($\theta$) observed in Joetsu at 03 JST (closed squares), 09 JST (open squares), 15 JST (open circles), and 21 JST (crosses) on 16 January 2001.

Figure 3.6 shows the vertical profiles of potential temperature ($\theta$) observed at Joetsu at 03, 09, 15, and 21 JST. At 03 JST, about 6 h prior to the formation of the snowband, a surface cooling layer is found from the surface to a height of 300 m. The $\theta$ in this cooling layer is about 1.5 K lower than that in the upper mixed layer. At 09 JST, the depth of the cooling layer has increased to 600 m. A decline of $\theta$ with about 1 K is observed near the surface. Around that time, the snowband formed. The vertical profile of $\theta$ at 15 JST is similar to that at 09 JST. This indicates that the surface cooling layer remains. At 21 JST, a rise of $\theta$ with about 1.5 K is observed near the surface, and the surface cooling layer has disappeared. The snowband had decayed until this time.

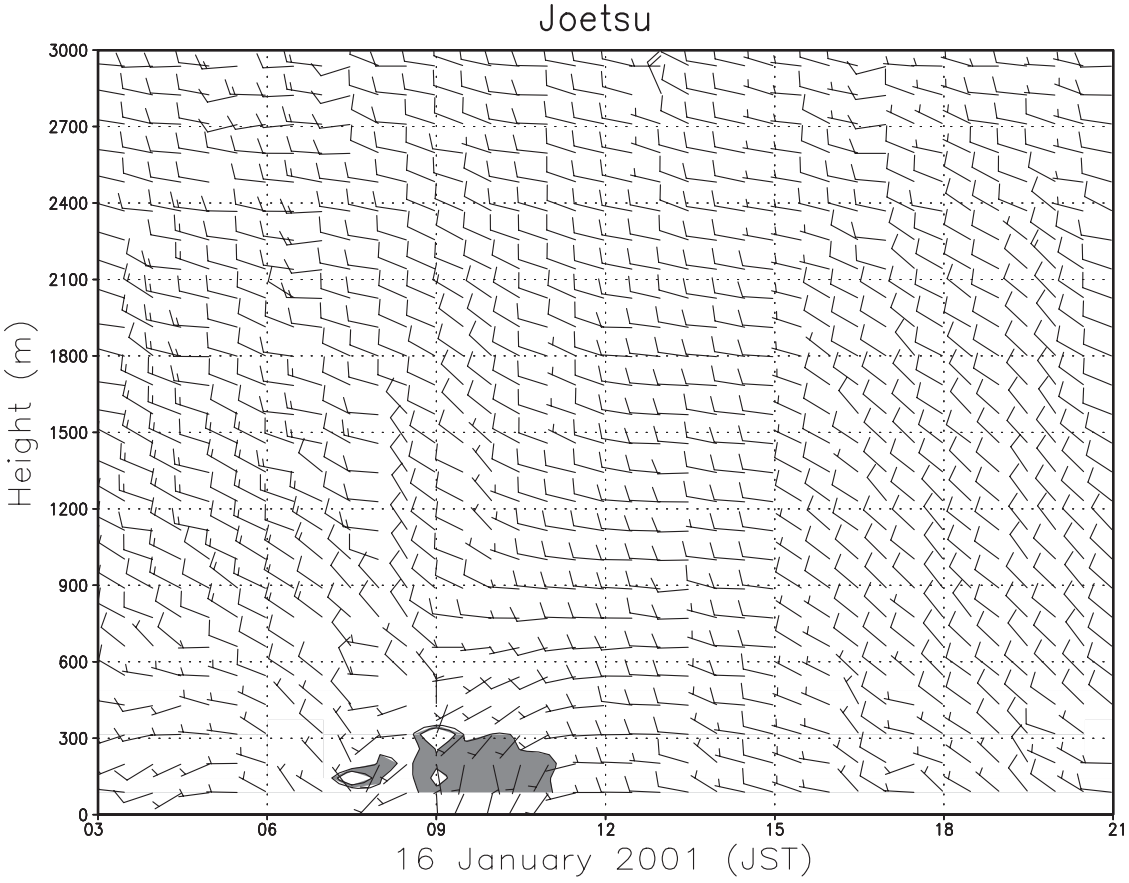


Figure 3.7: Vertical profiles of horizontal wind velocity observed by the boundary layer radar at Joetsu from 0300 JST to 2100 JST on 16 January 2001. Half-barb means 5 m $s^{-1}$ and one full barb means 10 m $s^{-1}$. The areas of wind direction between 160º and 220º are shaded.

A low-level wind variation measured by the BLR at Joetsu is shown in Fig. 3.7. Westerly or northwesterly winds at a speed less than 10 m $s^{-1}$ are predominant in this observation. The vertical wind shear is small. It is noted that, in the lowest 300 m, southerly winds at a speed less than 5 m $s^{-1}$ are observed during the period from 08 to 11 JST. Figure 3.8 shows the time series of surface meteorological data observed at Takada Weather Station in Joetsu. A large increase of pressure with 0.5 hPa and a little decline of temperature with 0.2ºC are observed during the period from 08 to 09 JST. These changes are caused by a land breeze of low-level southerly winds from land to sea, observed by the BLR (Fig. 3.7). The snowband formed around 09 JST just after the appearance of the land breeze, suggesting that the land breeze is a trigger for the formation of the snowband. After 09 JST, a decrease of pressure and a rise of temperature were observed (Fig. 3.8). Furthermore, the southerly wind had disappeared around 11 JST (Fig. 3.7). These features indicate that the land breeze became weaker after the snowband formed.

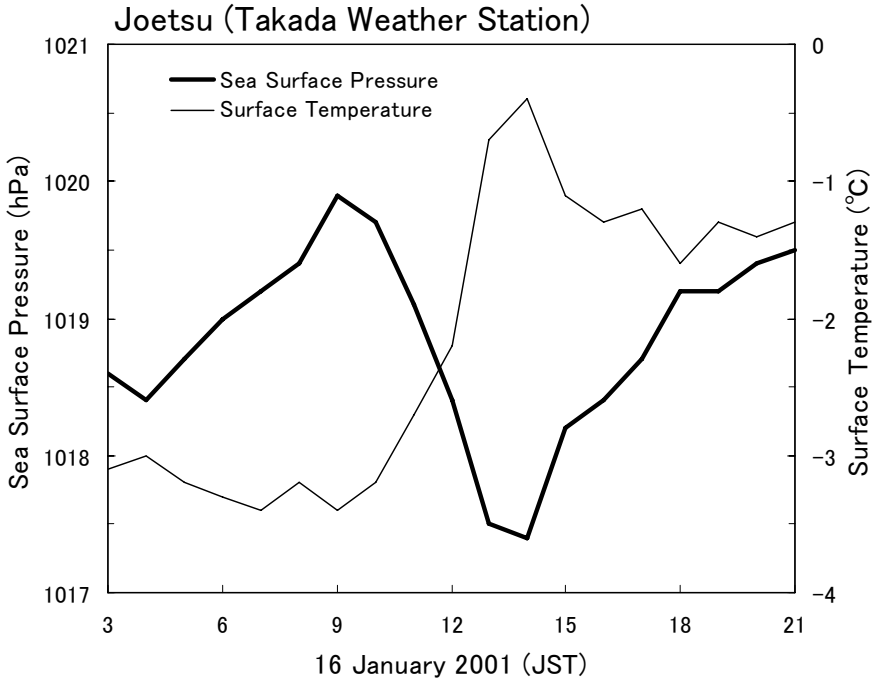


Figure 3.8: Time series of sea surface pressure (bold solid line) and surface temperature (thin solid line) in Joetsu (Takada Weather Station) from 03 JST to 21 JST on 16 January 2001.

Although the land breeze could contribute to the development of the surface cooling layer observed at Joetsu at 09 JST (Fig. 3.6), the depth of the land breeze was shallower than that of the cooling layer. Furthermore, the cooling layer lasted after the land breeze disappeared. These results indicate that there were some other mechanisms for the formation and maintenance of the observed surface cooling layer.

## 3.4 Numerical simulations

The general characteristics of the JMA-NHM simulation as well as the specific options chosen in this chapter are summarized in Table 3.1. In order to examine the structure of the snowband, a high-resolution numerical experiment is performed using the JMA-NHM with a horizontal resolution of 1 km. The vertical direction contains 38 levels with a variable grid interval of 40 m near the surface and 1090 m at the top of model domain. The terrain-following coordinate system is introduced such as

$$z^* = \frac{H(z - z_s)}{H - z_s}, \tag{1}$$

where $z_s$ is the surface height, and $H$ is the model-top height (20.36 km). The time step interval is 5 s. The cloud microphysics scheme is only used for the moist process in this experiment. The initial and boundary conditions are provided from the forecasts of the Regional Spectral Model (referred to as "RSM"; JMA 2002). The RSM is a hydrostatic model with a horizontal resolution of 20 km. It was operationally used in the JMA until November 2007. The domains of the two models are shown in Fig. 3.9. Daily analysis of the SST with 1.0º latitude/longitude resolution (JMA 2002) is used for a lower boundary condition in sea areas. The initial time of the JMA-NHM is 1000 JST on 16 January 2001 (1-h forecast of the RSM), and time-dependent boundary conditions with an interval of 1 h are used. The integration time is 9 h. For examining the formation of the snowband, it is desirable that the time previous to the snowband formation (09 JST) is adopted as the initial time. However, the snowband was not able to be well reproduced, when the initial time of the RSM used for the initial and boundary conditions is previous to 0900 JST on 16 January 2001. Therefore, the RSM forecast, of which initial time is 0900 JST, is adopted as the initial and boundary conditions for the JMA-NHM in this

experiment.

Table 3.1: Specification of the JMA-NHM and the experimental configurations in Chapter 3

| | |
|---|---|
| Initial time | 1000 JST, 16 January, 2001 |
| Time step | 5 s |
| Forecast period | 9 h |
| Horizontal mesh (resolution) | 300 × 300 (1 km) |
| Levels | 38 terrain-following stretched levels from 40 m to 1090 m |
| Model top | 20.36 km |
| Moist physics | bulk scheme, three-class ice (Ikawa and Saito 1991 based on Lin et al. 1983, Murakami 1990 and Cotton et al. 1986) |
| Surface | Bulk method (Ikawa and Saito 1991 based on Kondo 1975 and Sommeria 1976) |
| Turbulence | Diagnostic TKE scheme (Ikawa and Saito 1991 based on Deardorff 1980) |
| Radiation | Long and short wave radiation scheme for cloud optical properties with empirical constant (Saito et al. 2001 based on Sugi et al. 1990) |

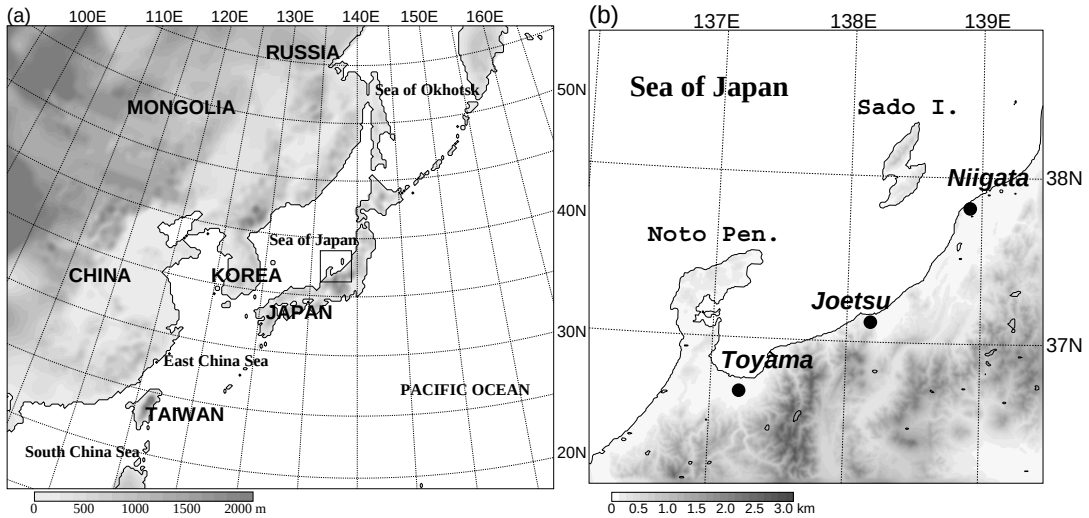


Figure 3.9: Calculation domains and topography of (a) the RSM and (b) the JMA-NHM. The square in (a) represents the domain of the JMA-NHM.

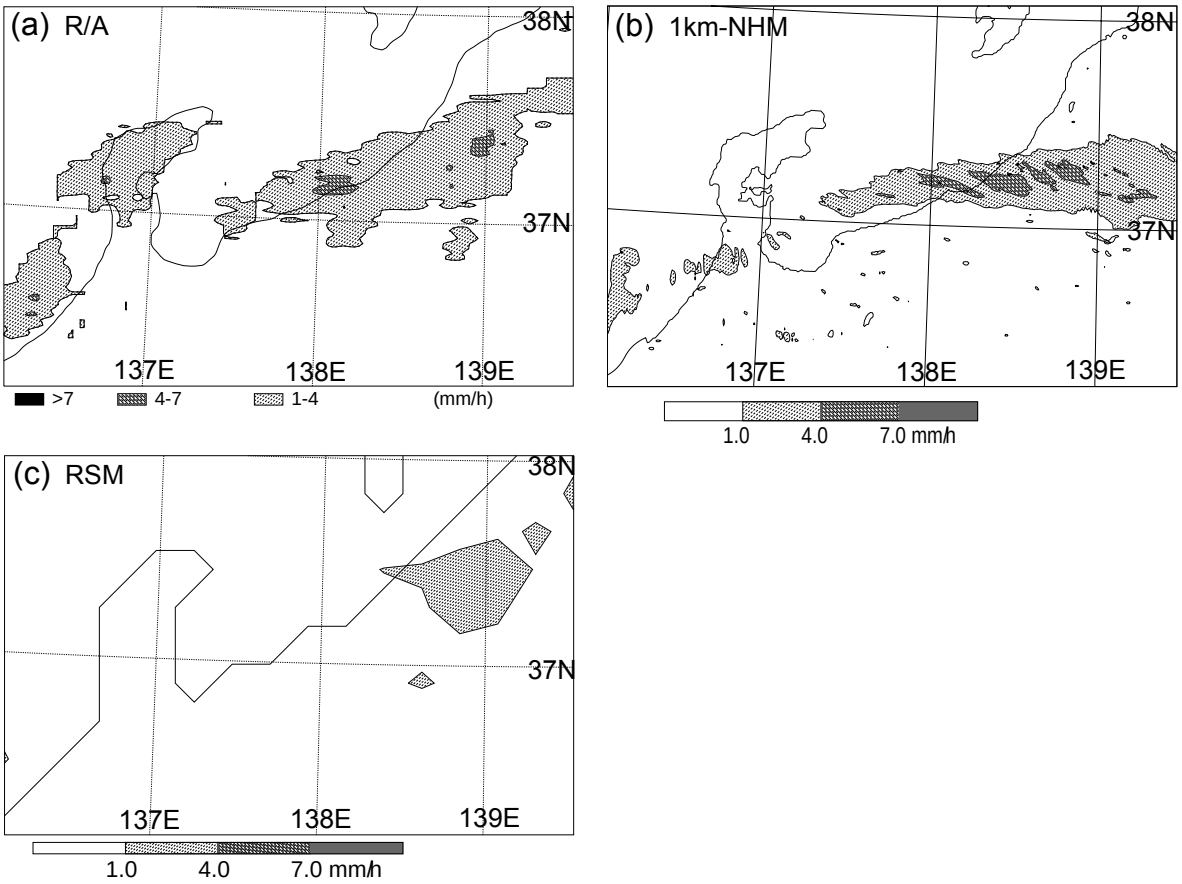


Figure 3.10: Horizontal distributions of hourly accumulated precipitation at 1500 JST on 16 January 2001, obtained by (a) the Radar/Raingauge-Analyzed Precipitation, (b) the JMA-NHM (5-h forecast), and (c) the RSM (6-h forecast).

Figure 3.10 shows hourly-accumulated precipitation charts at 1500 JST. The JMA-NHM well reproduces a line-shaped snowband in the coastal area of eastern Hokuriku district (Fig. 3.10b). The JMA-NHM-simulated snowband is similar in location, precipitation intensity, and shape to the observation (Fig. 3.10a), while the RSM-simulated precipitation area (Fig. 3.10c) is considerably smaller than the observation.

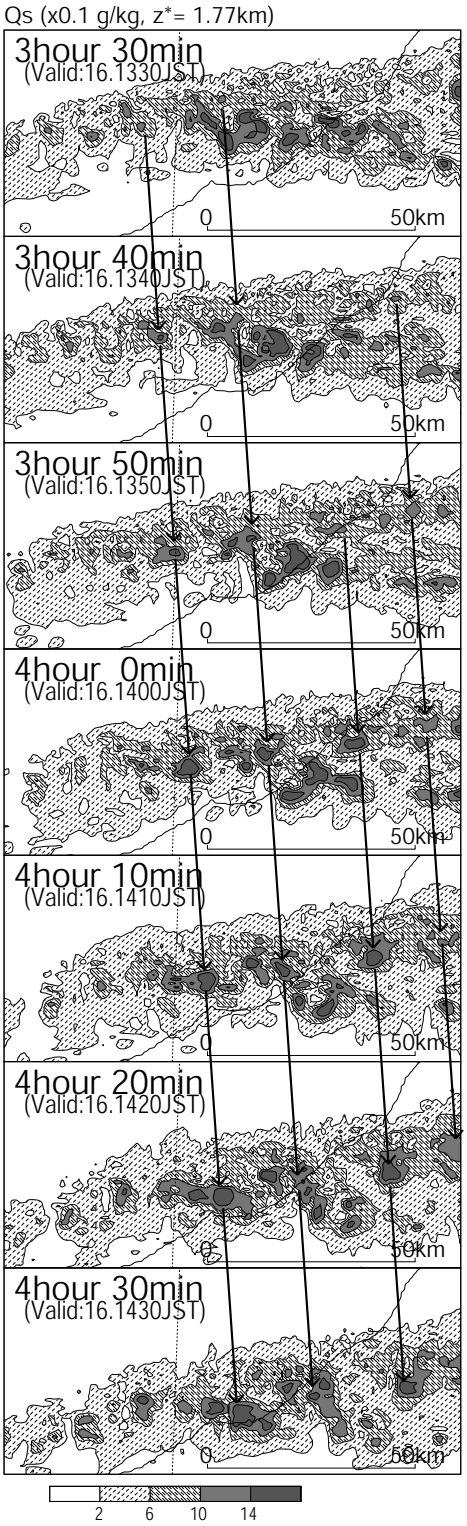


Figure 3.11: Horizontal distributions of snow mixing ratio (*qs*) at z* = 1.77 km simulated by the JMA-NHM. Outputs are shown every 10 minutes after 3.5-h forecast.

Figure 3.11 shows the time series of horizontal distributions of snow mixing ratio (*qs*) at the middle level of the snowband, simulated by the JMA-NHM. Model-simulated snowband consists of cellular high *qs* areas (defined by the 1.0 g $kg^{-1}$ contour, called snow cells hereafter). Each snow cell, which is a few km in horizontal scale, is thought to be generated by cumulus convection. Snow cells successively form at the northern part of the snowband, and propagate east-southeastward at a speed of about 8 m $s^{-1}$. Snow cells tend to develop and merge with pre-existent cells. Consequently, large *qs* areas with the horizontal scale of 5–20 km and the maximum of ~1.4 g $kg^{-1}$ are organized. Since these areas are made of convective snow cells, they can be regarded as meso-γ-scale convective systems. These features almost agree with those of the Doppler radar observation, except for the drastic regeneration of the snowband, presented by Kusunoki et al. (2002).

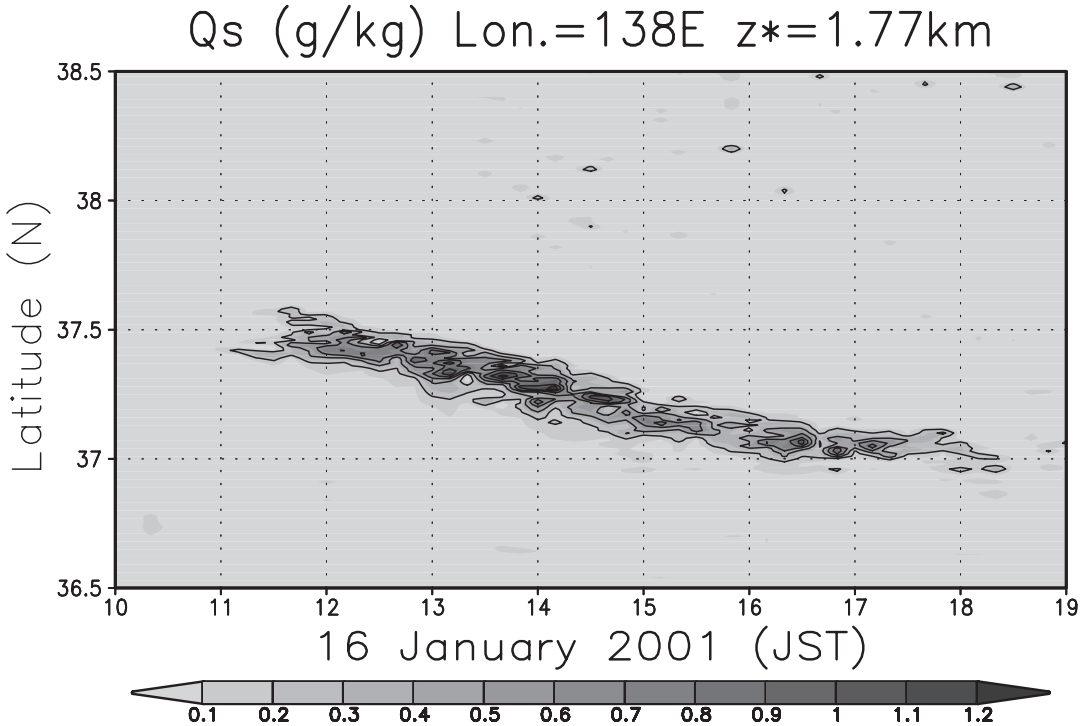


Figure 3.12: Time-latitude cross section of *qs* at z* = 1.77 km along 138ºE simulated by the JMA-NHM. The contours are drawn every 0.2 g $kg^{-1}$ above 0.2 g $kg^{-1}$.

Figure 3.12 shows the temporal variation of the JMA-NHM-simulated snowband. The simulated snowband forms around 11 JST (1-h forecast) and

lasts until around 18 JST (8-h forecast), slowly moving southward. As illustrated in Fig. 3.12, the JMA-NHM simulates a small snow amount during the first 2 h, due to the spin-up problem. An amount of model-simulated snow is also small during the last hour of the experiment. In comparison with the observation (Fig. 3.1b), the simulated snowband forms at a little higher latitude, and the simulated snowband propagates southward faster than that of the observation. Because of these features of simulated snowband, the distribution of simulated total precipitation is wider than that of the observation, while the total amount of simulated precipitation is less than that of the observation. However, as shown in Fig. 3.12, the movement and longevity of the observed snowband are well simulated; therefore, the JMA-NHM successfully reproduces key features of the observed snowband.

## 3.5 Structures of the snowband

### 3.5.1 Mean structures

The time-averaged structures of the simulated snowband are calculated to examine its internal structure. The averaged period is between 1330 JST (3.5-h forecast) and 1430 JST (4.5-h forecast). The average domain is shifted associated with the movement of the snowband, because the snowband moves slowly southward.

Figure 3.13a shows the time-averaged horizontal structure of *qs* and horizontal airflow pattern in the middle layer around the snowband. The region with the *qs* higher than 0.2 g $kg^{-1}$ is defined as the snowband. The areas with the *qs* higher than 1.0 g $kg^{-1}$ are aligned eastward from the center to the southern part of the snowband. These areas correspond to developed meso-γ-scale systems as shown in Fig. 3.11. The wind direction and speed inside the snowband are about west-northwest and about 10 m $s^{-1}$, respectively. This wind speed almost agrees with that observed by the BLR (Fig. 3.7) and that of simulated snow cells movement (Fig. 3.11). The horizontal divergence fields in the lower and upper layers are shown in Figs. 3.13b and 3.13c, respectively. In the lower layer, a line-shaped strong convergence zone is found along the northern edge of the snowband, where the divergence is dominant in the upper layer. The middle-level horizontal distribution of vertical velocities is shown in

Fig. 3.13d. A line-shaped strong updraft zone lies along the northern edge of the snowband. This updraft zone corresponds with the lower horizontal convergence zone. These features indicate that vertical circulations are situated around the snowband. Another line-shaped stronger updraft zone is found at the southern part of the snowband, corresponding to the areas the *qs* higher than 1.0 g $kg^{-1}$ (Fig. 3.13a).

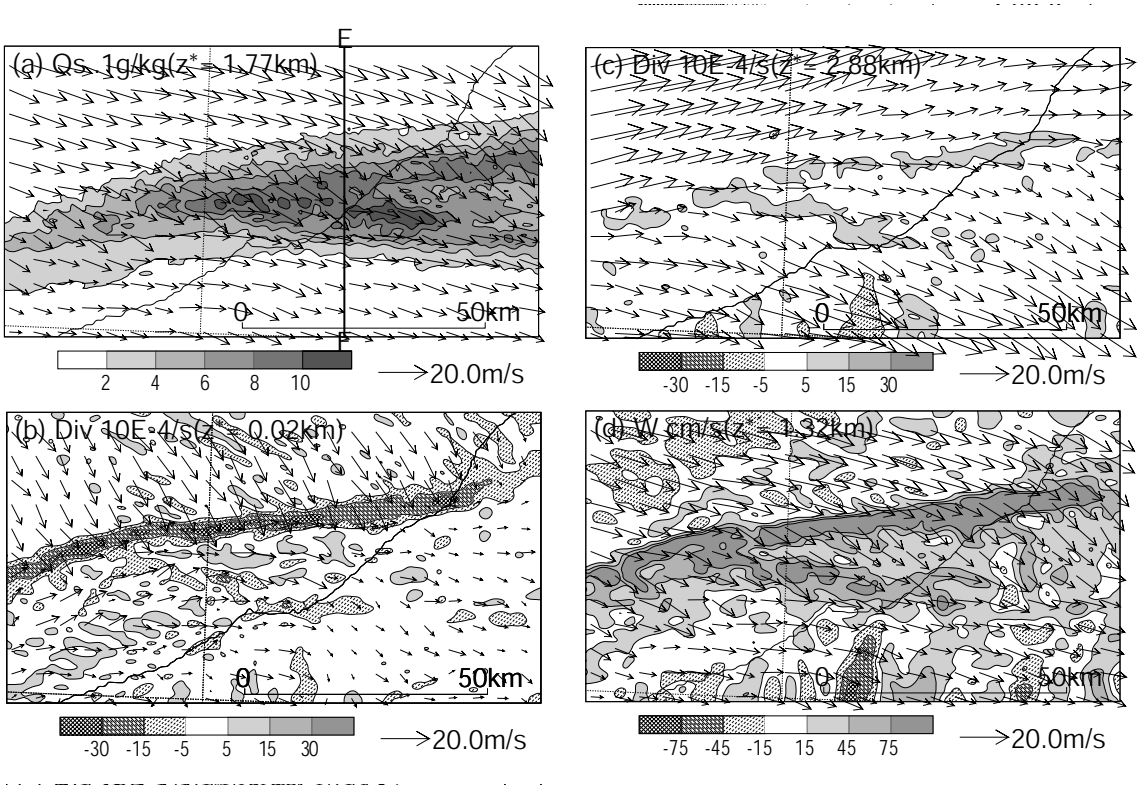


Figure 3.13: Time-mean horizontal structures of the snowband. The averaged period is between 1330 (3.5-h forecast) and 1430 JST (4.5-h forecast). Arrows show horizontal wind velocities at each level. (a) *qs* at z* = 1.77 km. (b) Horizontal divergence at z* = 0.02 km. (c) Horizontal divergence at z* = 2.88 km. (d) Vertical velocity at z* = 1.32 km. A bold solid line E–F shows the line along the vertical cross section shown in Fig. 3.15.

Figure 3.14 shows the vertical profiles of mean horizontal divergence and its components ($\partial u/\partial x$ and $\partial v/\partial y$) in the snowband over the line E–F in Fig. 3.13a. It is clear that convergence exists below a height of 1.3 km, and divergence

exists above that height. The maximum convergence is found at the lowest level. It should be noted that the magnitude of $\partial v/\partial y$ is much larger than that of $\partial u/\partial x$ in the whole layer. This result indicates that the vertical circulations are dominant in the band-normal cross section. Hereafter, the vertical structures of the snowband will be examined in the band-normal cross section.

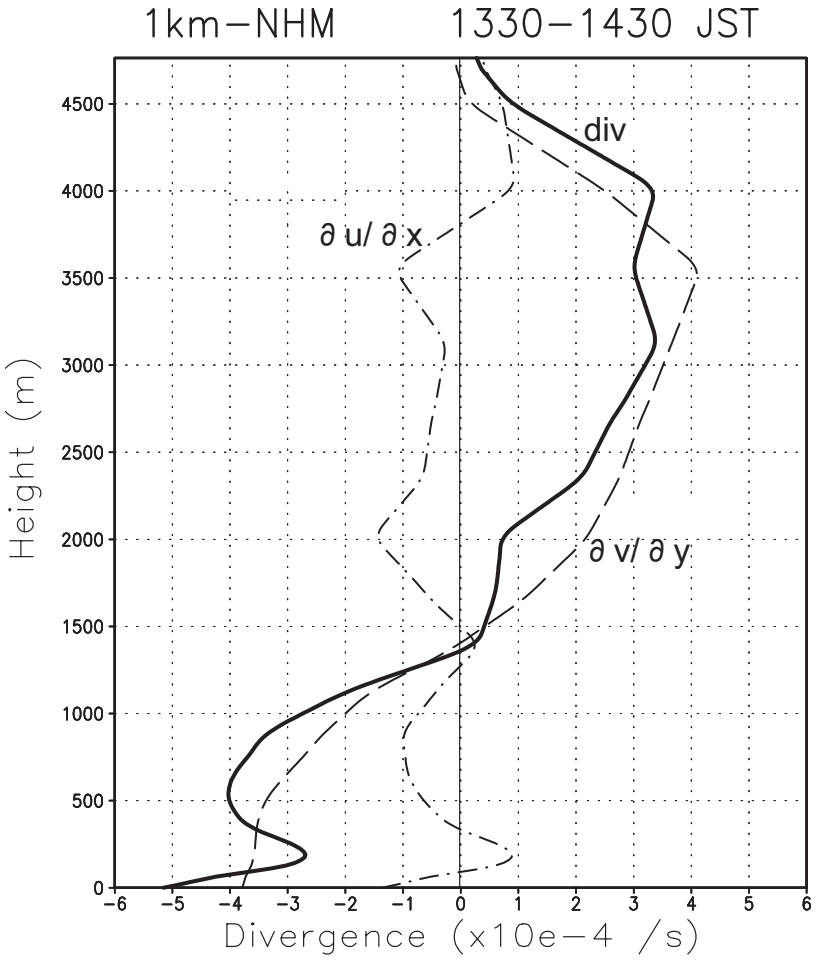


Figure 3.14: Vertical profiles of horizontal divergence (bold solid line), $\partial u/\partial x$ (dot-dashed line), and $\partial v/\partial y$ (broken line) averaged horizontally and temporally in the region of high $qs$ ($\geq 0.2$ g kg$^{-1}$) in the line E–F in Fig. 3.13a. The averaged period is same as Fig. 3.13.

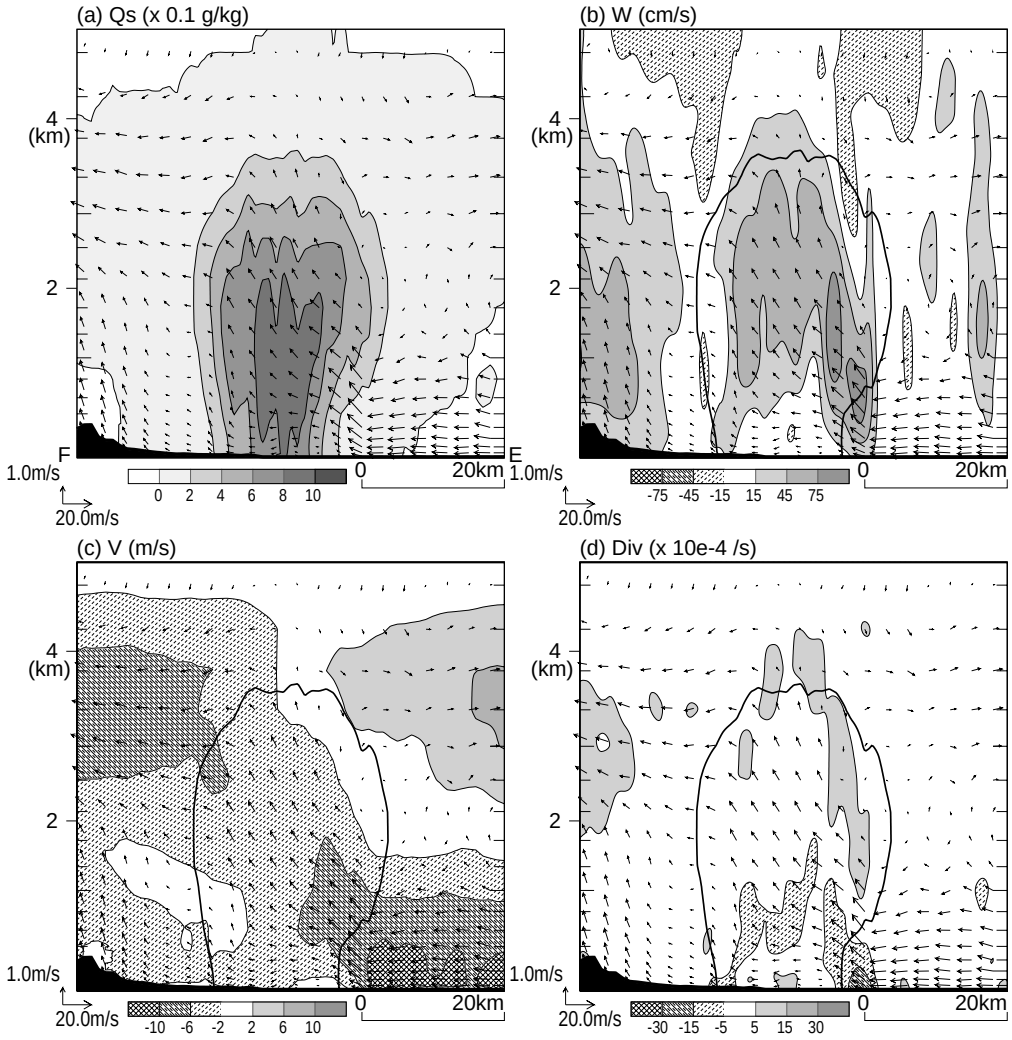


Figure 3.15: Time-mean structures of the snowband in a vertical cross section on the line E–F in Fig. 3.13a. The averaged period is same as Fig. 3.13. Arrows show airflow in the vertical cross section. (a) *qs*. (b) Vertical velocity. (c) Meridional velocity. (d) Horizontal divergence. A bold line in (b), (c), and (d) denotes a contour line of the 0.2 g $kg^{-1}$ *qs* in (a).

Figure 3.15 shows the mean structures of the snowband in the band-normal cross section along the line E–F in Fig. 3.13a. Figure 3.15a shows the vertical cross section of mean *qs* and airflow patterns. Inside the snowband (i.e., the region with $qs \geq 0.2$ g $kg^{-1}$), since the distribution of *qs* has a few peaks, the snowband is composed of a few snow cells in the band-normal structure, as shown in Fig. 3.11. The vertical cross section of vertical velocity is shown in Fig.

3.15b. Updraft is dominant inside the snowband. The core of strong updraft slants southward with height in the northern part of the snowband. In particular, the strongest updraft cores are found at the northern part of the snowband, as shown in Fig. 3.13d. This indicates the successive formation of convective cells. In contrast, no remarkable downdraft is found in the snowband. A strong updraft area is also found at the southern part of the snowband, corresponding to another line-shaped strong updraft zone, as shown in Fig. 3.13d. Figure 3.15d shows the vertical cross section of horizontal divergence. The low-level convergence and the upper-level divergence are simulated in the snowband, as discussed with Figs. 3.13b, 3.13c, and 3.14. The strongest convergence is found near the surface at the northern edge of the snowband. Figure 3.15c shows the vertical cross section of meridional wind velocity. Northerly flows are dominant to the north of the snowband under a height of 1 km. In contrast, the meridional winds are relatively weak under the snowband. The convergence of these low-level flows contributes significantly to the formation of strong updrafts at the northern edge of the snowband. These features in the wind structures almost agree with those found by the dual-Doppler analysis (Kusunoki et al. 2002).

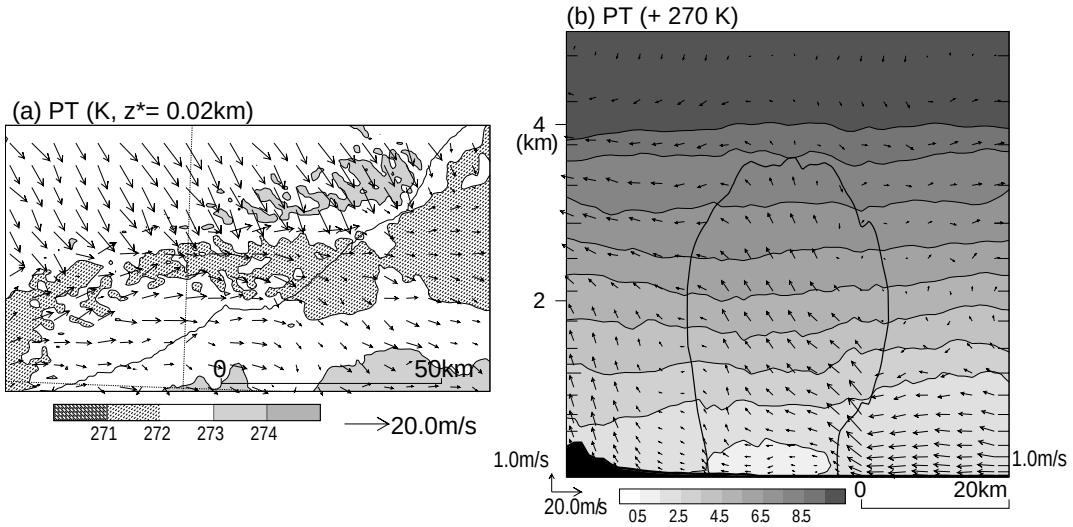


Figure 3.16: Time-mean structures of $\theta$. The averaged period is same as Fig. 3.13. (a) Horizontal distribution at z* = 0.02 km. Arrows show horizontal wind velocities. (b) Vertical distribution in the same cross section as those in Fig. 3.15. Arrows show airflow in the vertical cross section. A bold line denotes a contour line of the 0.2 g kg$^{-1}$ *qs* in Fig. 3.15a.

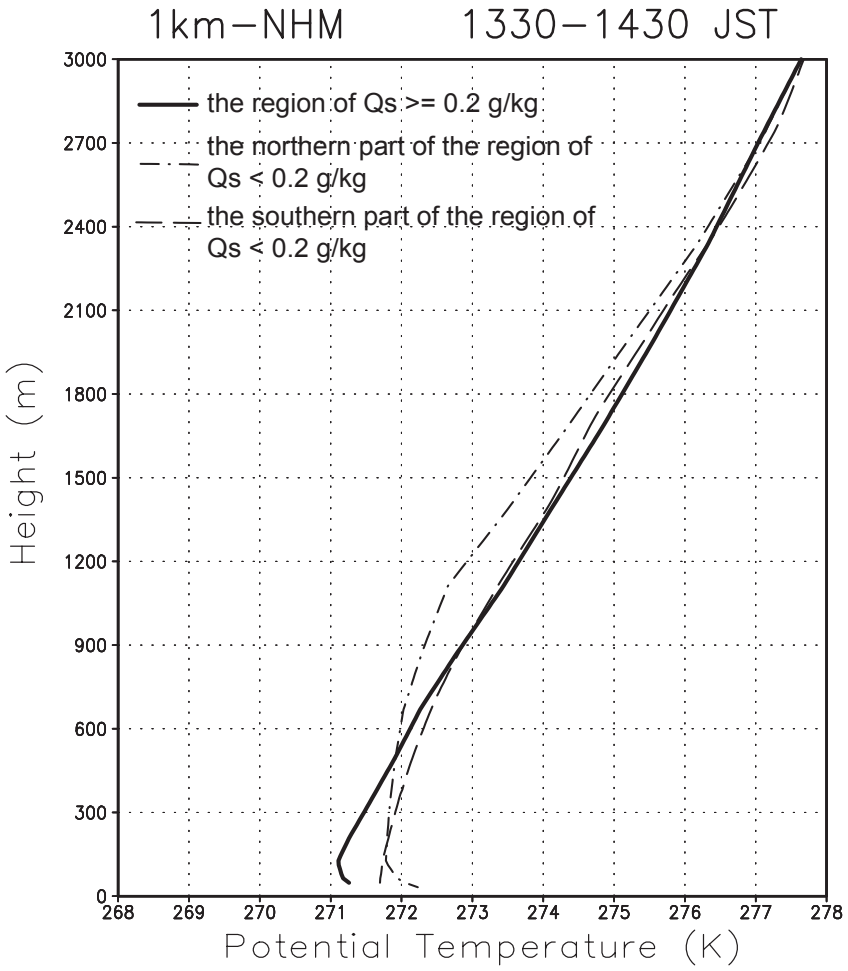


Figure 3.17: Mean vertical profiles of $\theta$ in the vertical cross section in Fig. 3.16b. The bold solid line shows the $\theta$ averaged in the region of high $qs$ ($\geq$ 0.2 g kg$^{-1}$). The dot-dashed line shows the $\theta$ averaged in the northern part of the region of low $qs$ (< 0.2 g kg$^{-1}$). The broken line shows the $\theta$ averaged in the southern part of the region of low $qs$ (< 0.2 g kg$^{-1}$).

Figure 3.16a shows the mean horizontal distribution of $\theta$ near the surface. A colder air area is found under the snowband, as shown in Fig. 3.13a. The boundary between relatively warm northwesterly winds and this colder air area corresponds to the line-shaped strong horizontal convergence zone (Fig. 3.13b). Figure 3.16b shows the mean vertical distribution of $\theta$. A colder air region is found at the lower part of the snowband. This indicates the formation of a cold pool. It is noted that, inside the cold pool, the meridional winds are weak (Fig. 3.15c). The airflow pattern in the band-normal cross section shows that the

warmer northerly winds flow over the cold pool. In order to examine the height and intensity of the simulated cold pool, the vertical profiles of $\theta$ in and around the snowband are shown in Fig. 3.17. In the lowest 500 m, the $\theta$ is about 1 K lower in the snowband (bold solid line) than in the north (dot-dashed line) and south (broken line) side. In comparison with observation (Fig. 3.6), the JMA-NHM almost reproduces the features of the observed cold pool; however, the height and intensity of the cold pool are slightly underestimated.

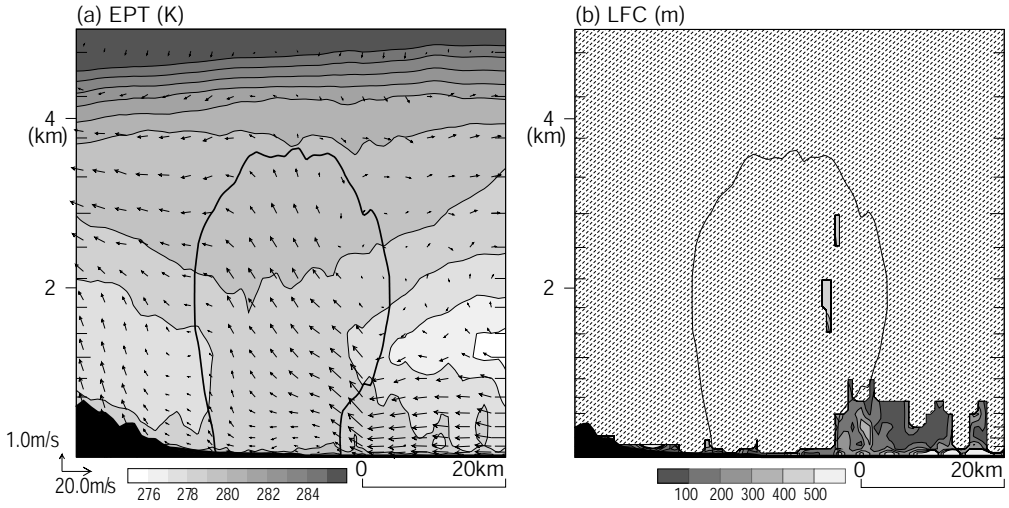


Figure 3.18: Time-mean structures in the same cross section as Fig. 3.15. The averaged period is same as Fig. 3.13. A bold line denotes a contour line of the 0.2 g kg$^{-1}$ *qs* in Fig. 3.15a. (a) Equivalent potential temperature. Arrows show airflow in the vertical cross section. (b) The level of free convection (LFC). LFC cannot be calculated in case that an air is lifted from the area shaded with dashed lines.

The vertical cross section of equivalent potential temperature ($\theta_e$) is shown in Fig. 3.18a. A low-level northerly flow, with a high $\theta_e$, produces convectively unstable layer to the north of the snowband. This high $\theta_e$ air is produced receiving heat and moisture from relatively warm sea surface. Figure 3.18b shows the vertical cross section of the level of free convection (LFC). The values in Fig. 3.18b denote the distance to LFC from the level of each originated point on the panel. The low-level air to the north of the snowband is able to reach the LFC by being lifted at a few hundred meters. This indicates that the low-level northerly flows tend to generate cumulus convection.

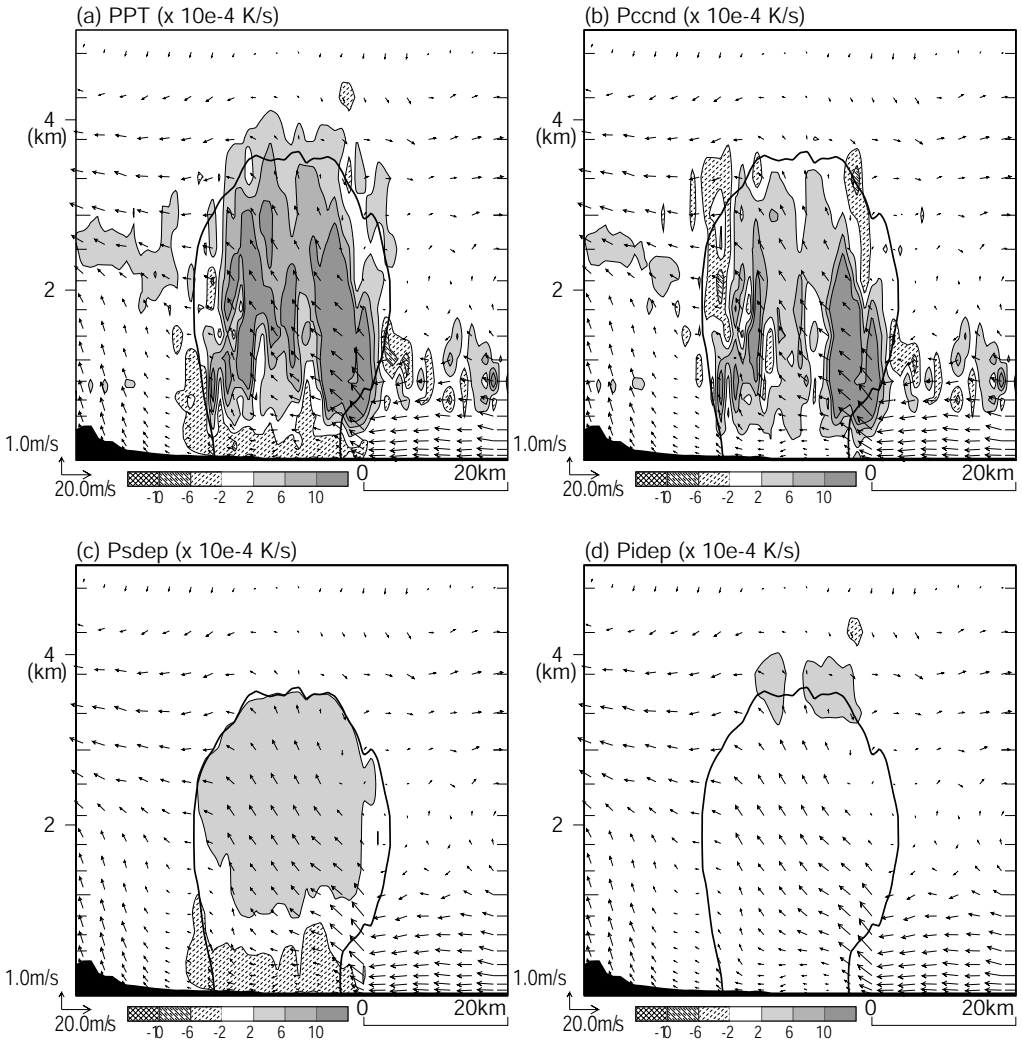


Figure 3.19: As for Fig. 3.15 except that different physical parameters are shown. (a) Diabatic heating by all processes of cloud microphysics. (b) Diabatic heating by condensation and evaporation. (c) Diabatic heating by deposition and sublimation related to snow. (d) Diabatic heating by deposition and sublimation related to cloud ice.

The convergence of the low-level northerly flows with a high $\theta_e$ and relatively weak winds in the cold pool under the snowband contributes significantly to the formation of updraft and cumulus convection at the northern edge of the snowband. Therefore, these low-level flows are essential for the development and maintenance of the snowband. The source of the northerly flows with a high $\theta_e$ is the winter monsoon, to which heat and moisture are received from the relatively warm sea surface. Meanwhile, what is the origin of the cold pool? In

the following subsection, the origin and role of this cold pool are examined.

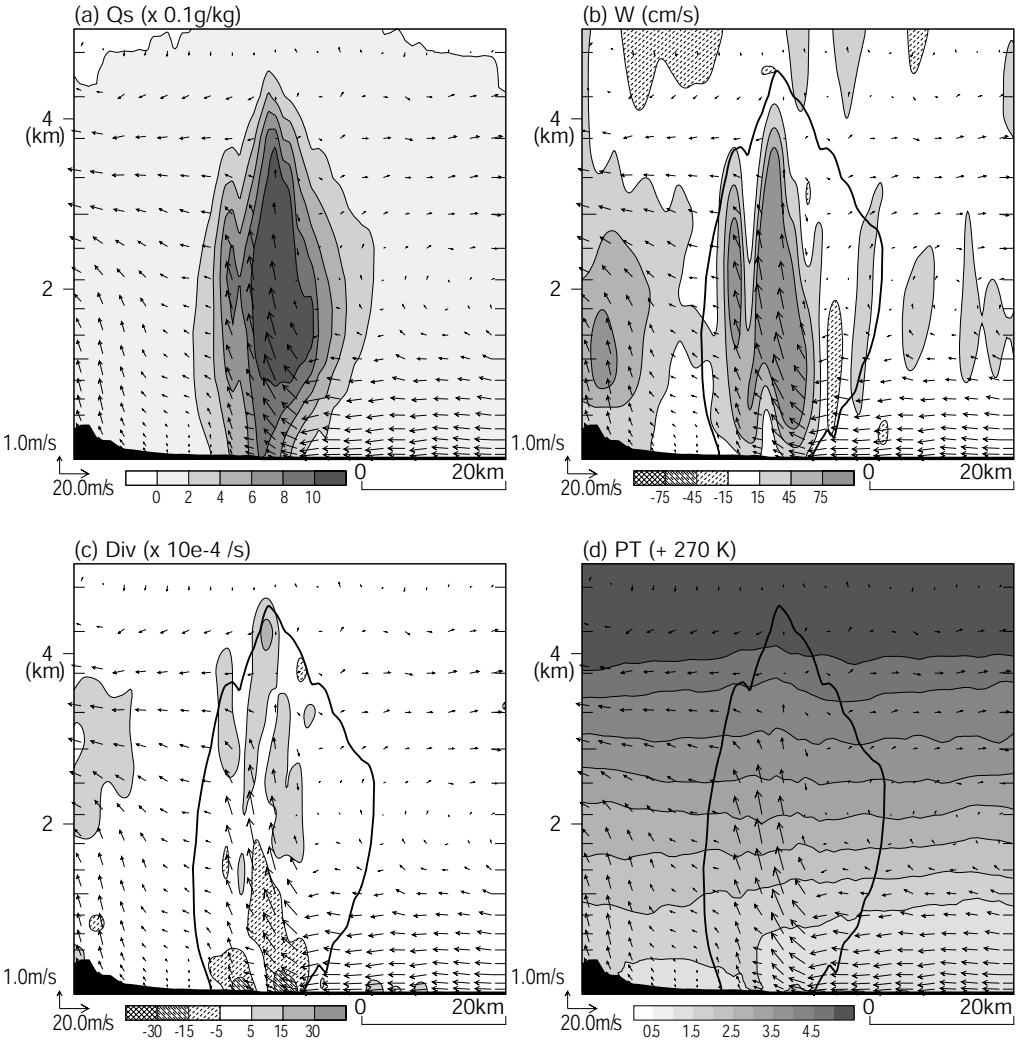


Figure 3.20: (a) As for Fig. 3.15a, (b) as for Fig. 3.15b, (c) as for Fig. 3.15c, and (d) as for Fig. 3.16b except for the simulation in which the sublimation process of snow is removed. A bold line in (b), (c), and (d) denotes a contour line of the 0.2 g $kg^{-1}$ *qs* in (a).

### 3.5.2 Origin and role of the cold pool under the snowband

The formation of the cold pool under the snowband is largely dependent on some cloud microphysics processes. Figure 3.19 shows the vertical cross sections of diabatic heating through cloud microphysics processes. The distribution of total diabatic heating (Fig. 3.19a) shows that the heating is

predominant inside the snowband. Especially, the large magnitude of heating in the northern part of the snowband indicates the formation of cumulus convection. On the contrary, a cooling area is found near the surface. This cooling area almost corresponds to the cold pool. This indicates that diabatic cooling contributes to the enhancement of the cold pool. The vertical cross sections of diabatic heating in three major processes are also shown in Figs. 3.19b, 3.19c, and 3.19d. The condensation and deposition of water vapor produce the majority of diabatic heating in the snowband (Figs. 3.19b and 3.19c). Meanwhile, the sublimation of snow is responsible for the diabatic cooling near the surface (Fig. 3.19c). The contribution of cloud ice to the total diabatic heating is small (Fig. 3.19d).

In order to estimate an effect of snow sublimation on the enhancement of the cold pool, a sensitivity experiment was conducted by removing the process of snow sublimation from the JMA-NHM. The band-normal vertical cross section, depicted from the result of the sensitivity experiment, is shown in Fig. 3.20. The cold pool under the snowband does not form (Fig. 3.20d), differently from the control experiment (Fig. 3.16b). Therefore, it is concluded that the cold pool is produced only through the process of snow sublimation.

As shown in Fig. 3.20b, an updraft core is simulated around the center of the snowband, and its magnitude is nearly two times larger in comparison with that in the control experiment (Fig. 3.15b). In the horizontal divergence field (Fig. 3.20c), the low-level convergence region is found under the center of the snowband, differently from the control experiment (Fig. 3.15c). As a result, the snowband in the sensitivity experiment overdevelops (Fig. 3.20a). Therefore, the cold pool contributes to form the characteristic structures of the snowband, such as the horizontal convergence and the updraft at the northern edge of the snowband.

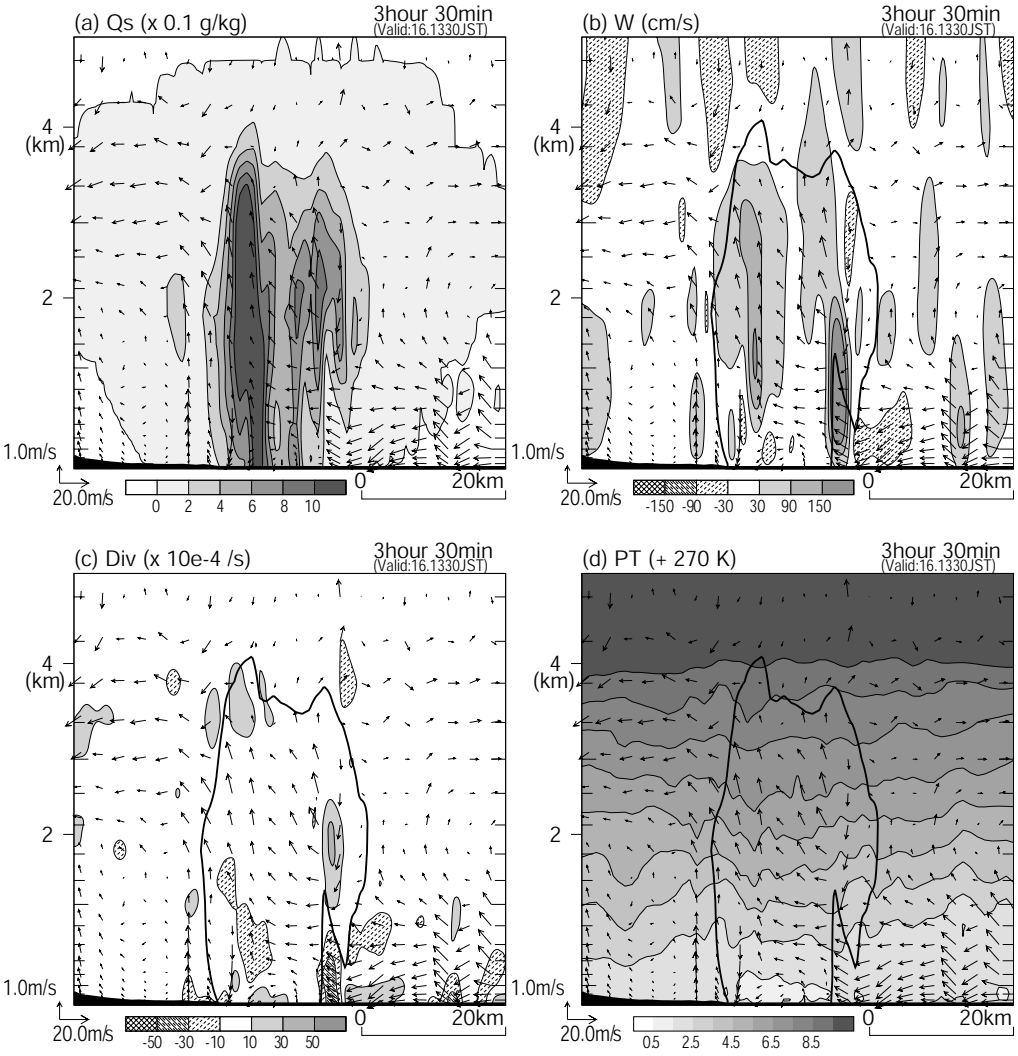


Figure 3.21: Vertical structures of the snowband in the cross section same as Fig. 3.15 at 1330 JST (3.5-h forecast). Arrows show airflow in the vertical cross section. (a) *qs*. (b) Vertical velocity. (c) Horizontal divergence. (d) $\theta$. A bold line in (b), (c), and (d) denotes a contour line of the 0.2 g kg$^{-1}$ *qs* in (a).

### 3.5.3 Contribution of detailed structures to mean structures of the snowband

As shown in Fig. 3.11, the snowband is composed of several snow cells and meso-γ-scale systems. In this subsection, the contribution of each snow cells and meso-γ-scale systems to the mean structures of the snowband is examined. Figure 3.21 shows the band-normal vertical structure at 1330 JST (3.5-h forecast). A few areas with high *qs* are found in the snowband (Fig. 3.21a).

These correspond to snow cells and a meso-γ-scale system. These detailed features are unclear in the mean structures (Fig. 3.15a). In the northern part of the snowband, small-scale snow cells, with the maximum *qs* of about 0.8 g $kg^{-1}$, are found in Fig. 3.21a. As shown in Figs. 3.21b and 3.21c, these snow cells are accompanied by low-level strong convergence and strong updraft. This indicates that they have just formed in the northern part of the snowband. Meanwhile, a meso-γ-scale system with higher *qs* ($\geq$ 1.0 g $kg^{-1}$), found in the southern part of the snowband, has larger horizontal and vertical scales. The moderate updraft found in this system implies that this system is in a mature stage. This updraft associated with the meso-γ-scale system forms the line-shaped updraft zone in the southern part of the snowband, shown in Fig. 3.13d. The updraft associated with the meso-γ-scale system has little relation to the cold pool, in contrast to that at the northern edge of the snowband. In the vertical profile of $\theta$ (Fig. 3.21d), the cold pool under the meso-γ-scale system is slightly deeper than that under the snow cells. This is because a strong snowfall produced by the meso-γ-scale system intensifies the cold pool.

As described above, the snapshot of the vertical structures shows the detailed variations associated with snow cells, and a meso-γ-scale system. However, the influence of the variations on the mean structures is not so large. For example, although the intensity of the cold pool under the snow cells is weaker than that under the meso-γ-scale system, the cold pool under the snow cells is able to produce the convergence at the northern edge of the snowband. Therefore, the following features shown in the mean structures are also dominant in the snapshot; the convergence of the low-level relatively warm northerly flow and the cold pool under the snowband generates cumulus convection at the northern part of the snowband.

## 3.6 Discussion

### 3.6.1 Formation mechanism of the snowband

In Section 3.3, several observations suggested that a land breeze was a trigger for the formation of the snowband in the present case. The BLR observations show that southerly winds were dominant under a height of 300 m just before the snowband formed. Surface observation data indicates that the southerly

winds were a land breeze, because they were accompanied by a decline of temperature and an increase of pressure.

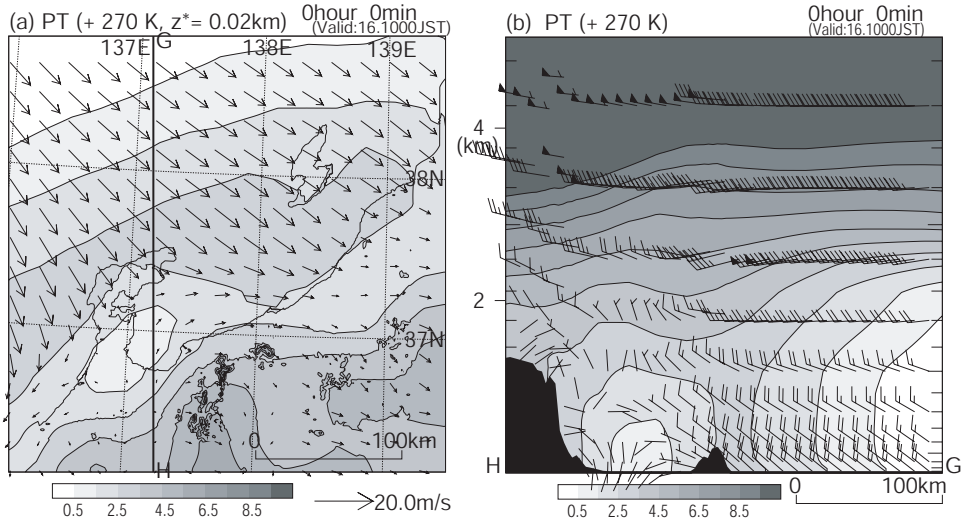


Figure 3.22: (a) Horizontal distribution of $\theta$ at z* = 0.02 km on the initial time of the JMA-NHM. Arrows show horizontal wind velocities. (b) Vertical-cross section of $\theta$ along the line G–H in (a). Half-barb, one full barb, and triangle-shaped barb mean 5 knots, 10 knots, and 50 knots, respectively.

As shown in Fig. 3.1b, the snowband formed around 09 JST. Because the initial time of the JMA-NHM is 10 JST, when the snowband had already formed, the numerical experiments cannot fully reveal the formation process of the snowband. However, the examination of the initial data can suggest the formation process of the snowband. Figure 3.22a shows the horizontal distribution of $\theta$ at the initial time. The low $\theta$ region with weak winds is distributed in the coastal area of the Hokuriku district. A horizontal convergence zone is found between the northwesterly monsoon and weak southerly winds around 37.4ºN. The vertical cross section of $\theta$ along the line G–H in Fig. 3.22a is shown in Fig. 3.22b. The cold layer found in the coastal area is several hundred meters deep, where southerly winds are predominant. This indicates that the cold southerly winds are a land breeze. Therefore, since the snowband forms on the convergence zone, the land breeze plays an important role for the formation process of the snowband. However, the origin and evolution processes of the land breeze in this region cannot be examine even using the initial data.

They will be examined in a future work.

As mentioned above, in the initial field (Fig. 3.22a), the horizontal convergence zone is located off the coast. As described in Section 3.4, in comparison with the observation, the JMA-NHM simulated the snowband at a little higher latitude. These results indicate that some errors are included in the initial wind field of the JMA-NHM. In this study, the initial condition of the JMA-NHM is only provided by the interpolated value of the RSM forecast. It is necessary for making a better simulation that the initial condition is improved by using some techniques, such as data assimilation.

### 3.6.2 Maintenance mechanism of the snowband

In this subsection, let us discuss the role of the cold pool for the maintenance mechanism of the snowband. As shown in the preceding section, the cold pool produced by snow sublimation contributes significantly to the formation of updraft and cumulus convection at the northern edge of the snowband. This suggests that the cold pool plays an important role on the maintenance of the snowband. The author would like to estimate the contribution of the cold pool to the maintenance of the snowband.

Figure 3.23 shows the time series of hourly accumulated precipitation charts. The amount of precipitation in the sensitivity experiment without snow sublimation (Fig. 3.23b) is larger than that in the case of the control experiment (Fig. 3.23a). This is caused by the increase in the amount of snow without sublimation. In the control experiment, the precipitation area associated with the snowband slowly shifts southward, as shown in Fig. 3.12. In the sensitivity experiment without snow sublimation, the simulated snowband also moves to the south, while its traveling speed is faster than that in the control experiment. The cold pool is not produced in the sensitivity experiment. These results indicate that the cold pool suppresses the southward movement of the snowband.

In the present snowband, new precipitation cells formed in the upstream side of developed ones. This formation has the similar feature to that of the back-building type, which is one of squall line types such as that observed in Oklahoma in the United States, and classified by Bluestein and Jain (1985). In the back-building type, new precipitation cells form upstream of precipitation bands. In the present case, however, new cells form along the upstream edge of

the snowband. Furthermore, in the present case, the snowband stagnates for a long time. Since the intensity of the cold pool is not so strong to produce a strong gust, the line-shaped convergence between the cold pool and relatively warm northerly flow, over which new convective cells form, stays in almost the same place.

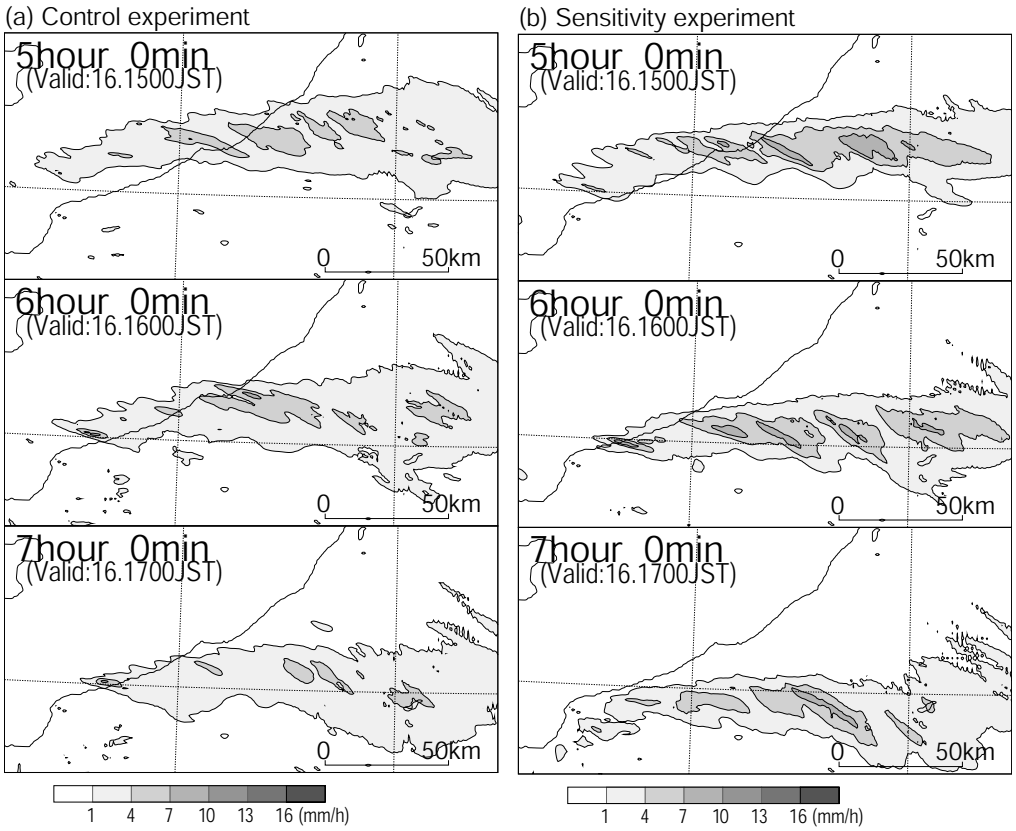


Figure 3.23: Time series of hourly accumulated precipitation simulated by (a) control experiment and (b) sensitivity experiment in which the sublimation process of snow is removed. Outputs are shown every 1 h after 5-h forecast.

Many studies suggested that a cold air due to the diabatic cooling through sublimation of ice and snow particles plays an important role on the self-organization of convection (e.g., Sakakibara et al. 1988b; Ishihara et al. 1989; Maki et al. 1992; Fujiyoshi et al. 1998). In their studies, the cold air was also accompanied by strong downdrafts, and a gust front formed near the surface. In the present case, neither strong downdraft nor near-surface strong gust is

simulated in the cold layer. Here, it is noted that a weak cold pool, without any strong gust, is also able to organize new convection, as shown in the present case.

Figure 3.23b also shows that the snowband lasts in the sensitivity experiment, although no cold pool is simulated. This indicates that there are some other mechanisms which maintain the snowband by keeping the low-level convergence. One of the mechanisms is thought to be the reinforcement of the low-level convergence by the strong updrafts that are produced by a great deal of latent heat release. As shown in Fig. 3.18a, the northerly flows supply high $\theta_e$ air to the snowband. This high $\theta_e$ air is able to reach LFC by being lifted at a few hundred meters (Fig. 3.18b). Therefore, it can rise to LFC by developed convection, and then latent heat release occurs. As a result, updraft and low-level convergence are intensified. This feedback mechanism is able to be maintained, because the northerly flows with high $\theta_e$ lasts during the occurrence of the snowband. The maintenance mechanism of the convergence, due to the latent heat release, was pointed out by Kato and Goda (2001).

The land breeze, which is a trigger for the formation of the snowband, is thought to be another maintenance mechanism of the low-level convergence. Ishihara et al. (1989) suggested that the successive formation of snowbands and low-level convergence lines was largely dependent on the duration of the land breeze circulation. From the BLR observation (Fig. 3.7), a land breeze had disappeared until 11 JST. In the simulation, a strong land breeze is not seen at that time. However, relatively weak west-southwesterly wind areas are distributed to the south of the snowband near the surface (e.g., Fig. 3.16a). In this region, since the sea-land temperature contrast is large in winter, the land breeze circulation remains, although it becomes weak.

Around the eastern coastal region of the Hokuriku district, a similar mesoscale convergence line was also observed during another period of the WMO-01 (Yoshihara et al. 2004). They suggested that a dynamical effect of topography was mainly responsible for the formation of the convergence line. Since the Hokuriku region is surrounded with a peninsula and high mountains, the synoptic-scale winds (e.g., the winter monsoon) can be modified by topography. This topographic effect can influence the formation of convergence line, even in the present case.

In order to estimate the contribution of the cold pool to the formation of low-level convergence, the distribution of horizontal divergence near the surface in the sensitivity experiment, in which no cold pool is simulated, is compared with that in the control experiment. Figure 3.24 shows snapshots of simulated horizontal divergence near the surface at 1400 JST (4-h forecast). In the control experiment (Fig. 3.24a), line-shaped convergence areas form, as shown in mean structures (Fig. 3.13b). In the sensitivity experiment (Fig. 3.24b), convergence areas are also simulated. However, their magnitude is smaller than that in the control experiment, and their shape is almost cellular, rather than linear. These features indicate that the cold pool contributes significantly to the maintenance and intensification of line-shaped convergence in the present case. The intensification of the convergence, due to the sublimation of snow particles, was also pointed out by Fujiyoshi et al. (1988) and Yoshihara et al. (2004).

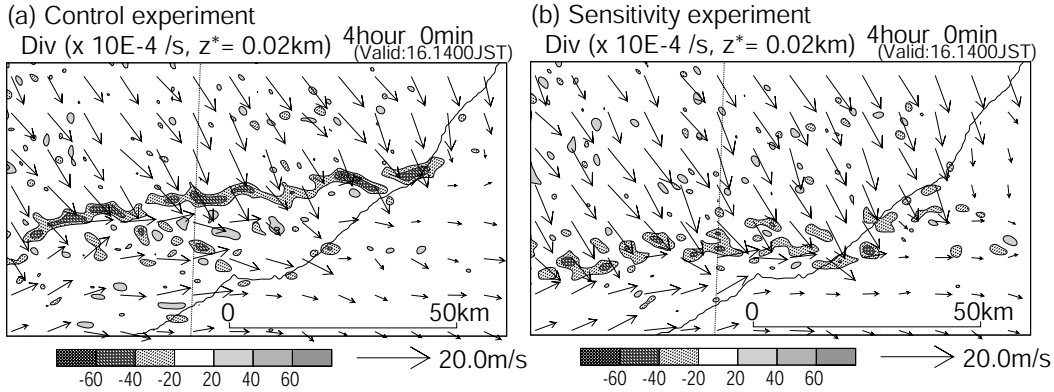


Figure 3.24: Horizontal distributions of horizontal divergence at z* = 0.02 km on 1400 JST (4-h forecast) simulated by the JMA-NHM (a) with a control experiment and (b) with a sensitivity experiment in which the sublimation process of snow is removed. Arrows show horizontal wind velocities.

The results of the present study and the previous studies (Ishihara et al. 1989; Yoshihara et al. 2004), suggest that low-level convergence lines are generated and maintained by various factors along the coastal region of the Hokuriku district. They also point out that the strong interaction between low-level convergence lines and snowbands influences the formation and maintenance mechanisms of the low-level convergence lines. Further studies are necessary to

clarify the mechanisms of snowbands around the Hokuriku region.

## 3.7 Conclusions

On 16 January 2001 during the WMO-01, a quasi-stationary snowband was observed extending from the east of Toyama Bay to the coastal area of the eastern Hokuriku district. This snowband was about 150 km long and about 50 km in width. It stagnated for half a day, and brought a snowfall of about 50 cm in this area. Figure 3.25 illustrates schematic depiction of the detailed structures and the formation and maintenance mechanisms of the snowband by analyzing the simulation results of the JMA-NHM in addition to the special observations of the WMO-01.

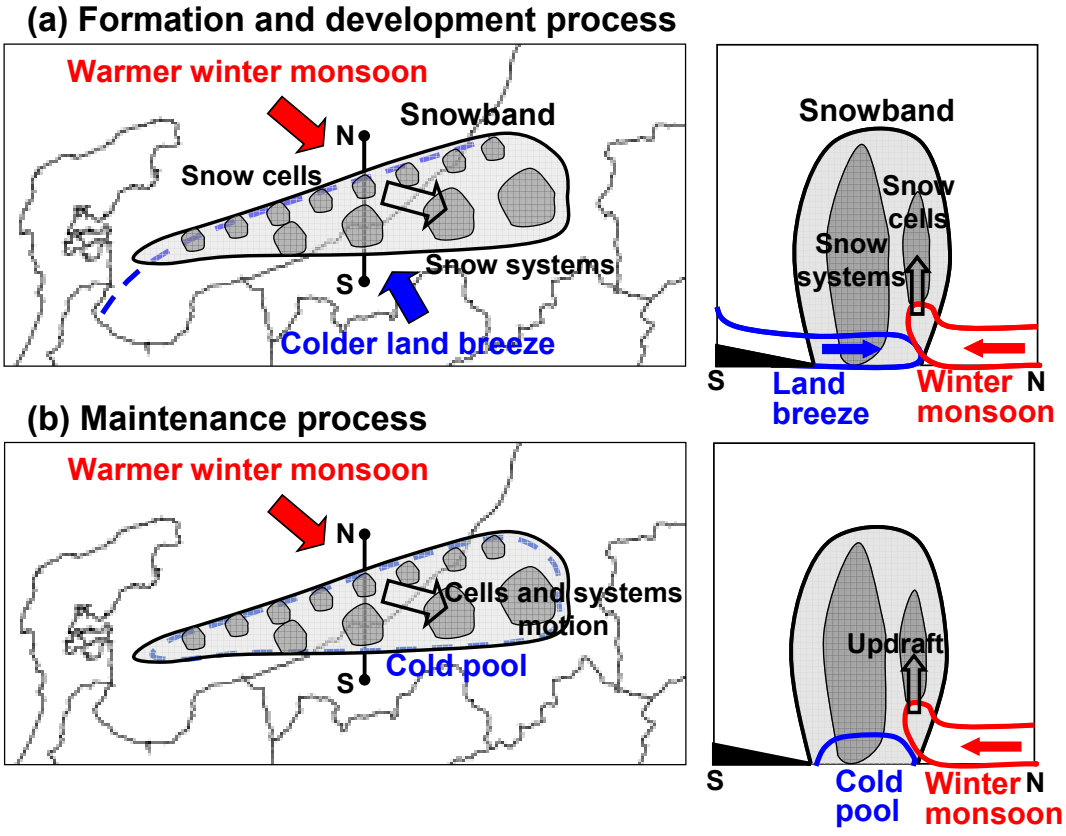


Figure 3.25: Schematic depiction of the structures and the formation and maintenance mechanisms of the snowband observed on 16 January 2001. Left figures show the horizontal structures of the snowband. The vertical cross sections perpendicular to the alignment of the snowband along the line N–S are shown in Right figures.

The snowband was simulated by the JMA-NHM with a horizontal grid size of 1km (JMA-NHM) that was nested within the forecast of the RSM. The JMA-NHM successfully reproduced the shape and precipitation intensity of the snowband. The simulated snowband contained several snow cells with the horizontal scale of a few km, and meso-γ-scale snow systems. These snow cells formed in the northern part of the snowband, and propagated east-southeastward. The snow cells developed and some of them organized a meso-γ-scale system. A line-shaped strong horizontal wind convergence zone was simulated at the northern edge of the snowband, where cumulus convection formed. These features are almost in common with those analyzed by dual-Doppler observations.

A weak cold pool was observed under the snowband by upper-air soundings. This cold pool was well reproduced by the JMA-NHM. A sensitivity experiment confirmed that the diabatic cooling, due the sublimation process of snow particles, was responsible for the formation of the cold pool. The convergence between the cold pool and a low-level northerly flow with a high $\theta_e$ to the north of the snowband contributed significantly to the formation of strong updraft and cumulus convection at the northern edge of the snowband. Therefore, these low-level flows are essential for the development and maintenance of the snowband.

The BLR and surface meteorological observations show that a land breeze could be a trigger for the formation of the present snowband. This was ascertained by examining the initial data of the JMA-NHM. The remarkable land breeze was not maintained during the existence of the snowband in both the observation and the simulation. The sensitivity experiment showed that the cold pool compensated for the weakened land breeze and contributed to the maintenance of the horizontal convergence.

# Chapter 4

# Structure and formation mechanism of transversal cloud bands associated with the JPCZ cloud band on 14 January 2001

## 4.1 Introduction

As mentioned in Chapter 1, the structure and the formation mechanism of the transversal cloud bands in the JPCZ cloud band are not yet clear. Moreover, it has been shown in the previous chapter that the snowband formed along the coastal region where the transversal cloud bands landed, suggesting that the transversal cloud bands is related to the snowband. During the WMO-01, the JPCZ cloud bands formed frequently. A typical JPCZ cloud band was observed by an instrumented aircraft off the coast of the San-in district on 14 January 2001. In this observation, cloud features were captured by an airborne CPR (SPIDER). In addition, the simulation of the observed JPCZ cloud band was performed using the JMA-NHM.

The purpose of this chapter is to clarify the characteristics (e.g., spacing, depth, and orientation), the kinematic and thermodynamic structures, and the formation mechanism of the transversal cloud bands in the JPCZ cloud band observed on 14 January 2001, by analyzing data provided by the special observations of the WMO-01 and the simulation results of the JMA-NHM with a horizontal resolution of 1 km. An overview of the JPCZ cloud band on 14 January 2001 is presented in Section 4.2. Detailed structures of the JPCZ cloud band and its environmental fields are described in Section 4.3, based on the special observations of the WMO-01. In Section 4.4, a numerical experiment is

conducted using the JMA-NHM. The simulated JPCZ cloud band is compared with the observation. An examination of simulation results is focused on the transversal cloud bands. The structure and the formation mechanisms of the transversal cloud bands are discussed in Section 4.5. The conclusions are presented in the last section.

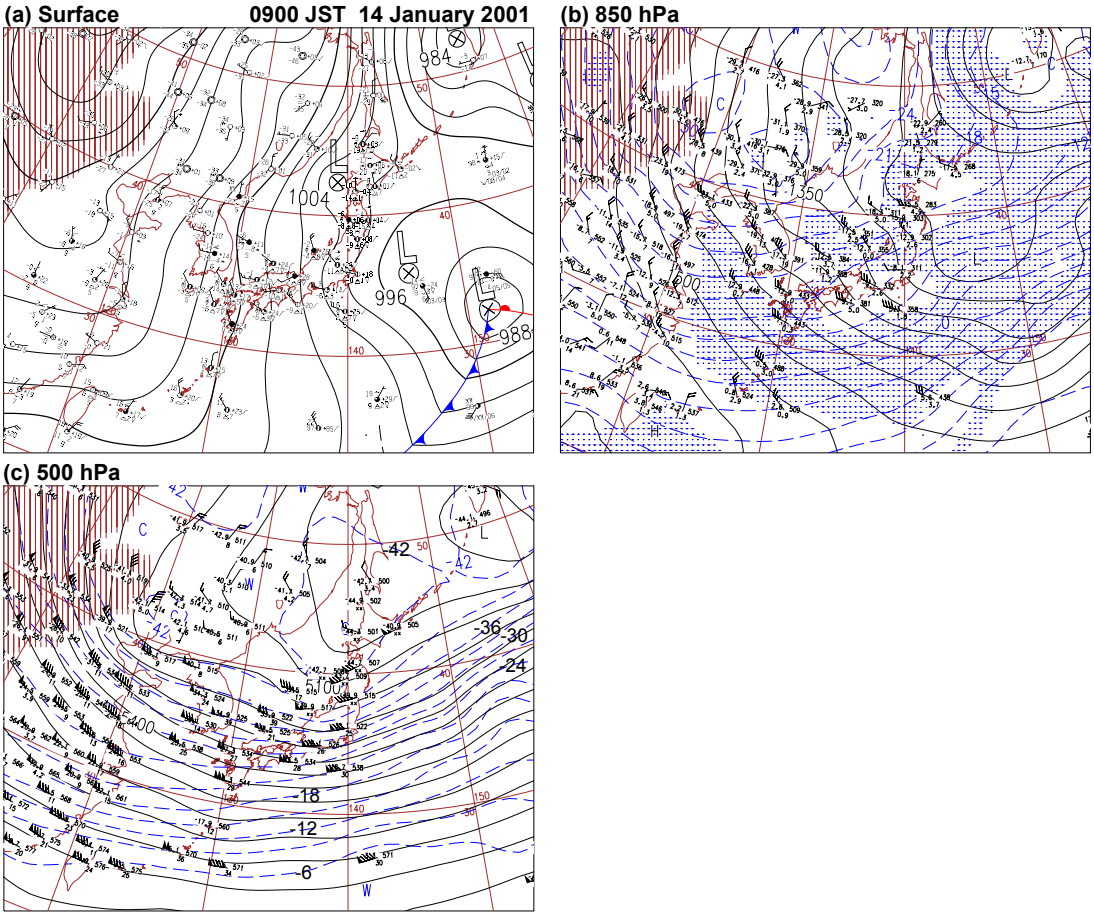


Figure 4.1: Weather maps provided by the JMA at 0900 JST on 14 January 2001. (a) At the surface, pressure is contoured by solid lines every 4 hPa. Half, full, and triangle-shaped barbs mean 5 knots, 10 knots, and 50 knots, respectively. (b) At 850 hPa, geopotential height is contoured by solid lines every 50 m; temperature is contoured by dashed lines every 3ºC; the wet areas (T−Td < 3ºC) are dotted. (c) At 500 hPa, geopotential height is contoured by solid lines every 60 m; temperature is contoured by dashed lines every 3ºC.

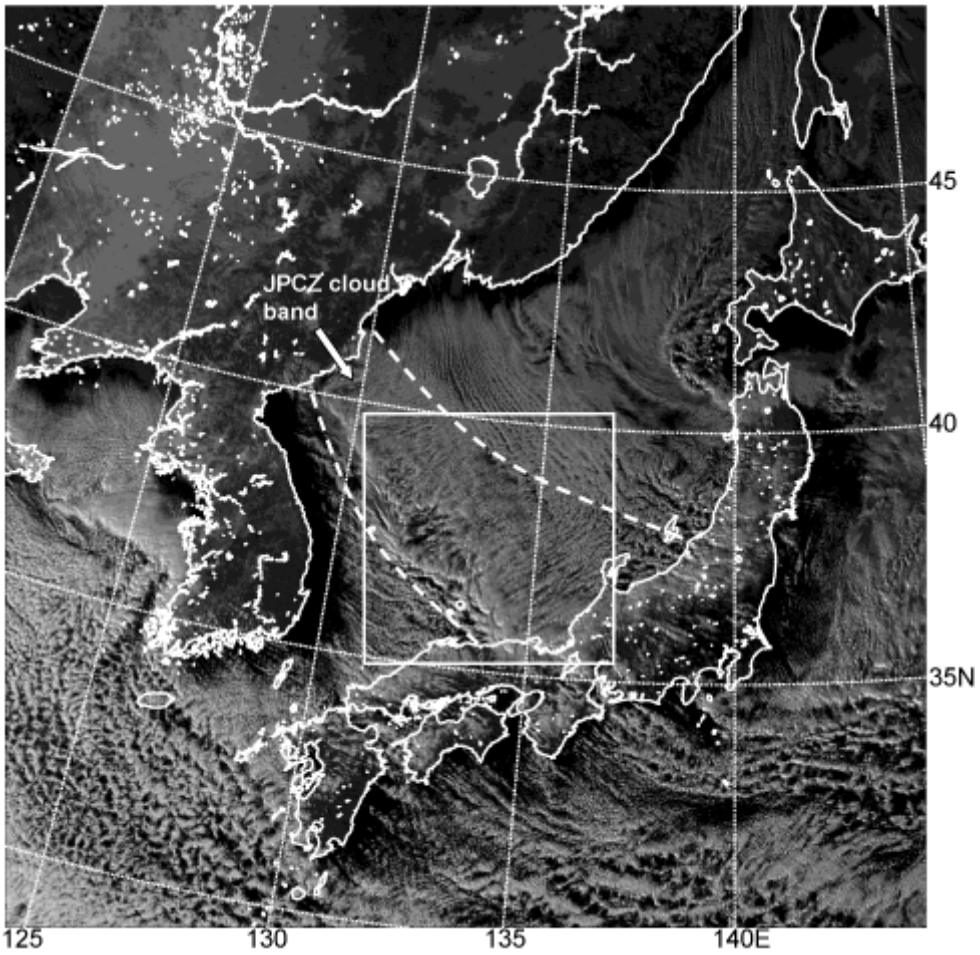


Figure 4.2: GMS-5 visible image at 1500 JST on 14 January 2001. The rectangle corresponds to the display area in Figs. 4.4a and 4.4c. Two dashed lines denote the boundaries of the JPCZ cloud band.

## 4.2 The JPCZ cloud band on 14 January 2001

Figure 4.1 shows the weather maps at 0900 JST on 14 January 2001. A developing extratropical cyclone with fronts exists over the Pacific Ocean to the east of Japan (Fig. 4.1a). This extratropical cyclone formed over the East China Sea around Taiwan on 13 January and moved east-northeastward over the Pacific Ocean along the southern coast of the Japanese Islands. Between the cyclone and a high-pressure zone over the continent, the contours of sea level pressure around Japan lie in a south-north direction. This pressure pattern often appears during the winter monsoon season, showing that there is an outbreak of

cold air from the Eurasian Continent over the Sea of Japan. At a level of 850 hPa (Fig. 4.1b), the isometric lines (solid lines) are almost normal to the isotherms (dashed lines) over the Sea of Japan. This feature denotes that the advection of a cold air was caused in this area. At a level of 500 hPa (Fig. 4.1c), a cold air mass with the temperature less than –33ºC covers most of the Sea of Japan. An eastward moving trough is situated over the Sea of Japan off the coast of the northern part of the Japanese Islands. Another trough with the minimum temperature of –42ºC is found over the Bohai Sea. After that, this trough moved eastward and passed over the Sea of Japan. At 0900 JST on 15 January (not shown), it reached over the Tohoku and Hokuriku districts.

Figure 4.2 shows the GMS-5 visible image at 1500 JST on 14 January 2001. Many convective clouds are found over the Sea of Japan as a consequence of heat and moisture supply to a continental cold air mass from the sea surface with the relatively high SST. The JPCZ cloud band with a width of 200–300 km is distributed over the Sea of Japan from the base of the Korean Peninsula to Wakasa Bay. A remarkably developed convective cloud band is found along the southwestern edge of the JPCZ cloud band. Transversal cloud bands extending to the northeast from the developed convective cloud band are also found in the JPCZ cloud band. Many cloud streets are distributed on both sides of the JPCZ cloud band.

A time series of the GMS-5 infrared images are shown in Fig. 4.3 for the period from 2100 JST on 13 January 2001 to 0300 JST on 15 January 2001. At 2100 JST on 13 January (Fig. 4.3a), the JPCZ cloud band extended from the base of the Korean Peninsula to the Hokuriku and Tohoku districts. The areas with low brightness temperature (TB) are distributed off the coast of the Hokuriku district, where clouds developed under the upper-level trough (see Fig. 4.1c). Associated with the northeastward propagation of the trough, these areas gradually moved to the Tohoku and Hokuriku districts and disappeared (Figs. 4.3b–d). Meanwhile, the downstream part of the JPCZ cloud band shifted to the southwest (Figs. 4.3a–c). Then, the JPCZ cloud band has remained quasi-stationary (Figs. 4.3c and 4.3d). Associated with the eastward propagation of the above-mentioned second trough located over the Bohai Sea at 0900 JST on 14 January (Fig. 4.1c), the JPCZ cloud band had gradually developed. At 2100 JST on 14 January (Fig. 4.3e), the low TB areas were found in the

southeastern part of the JPCZ cloud band, indicating the development of the JPCZ cloud band. These low TB areas extended northeastward, causing a heavy snowfall in the Hokuriku district (Fig. 4.3f). The movement and intensification processes of the present JPCZ cloud band have been examined by Ohigashi and Tsuboki (2007).

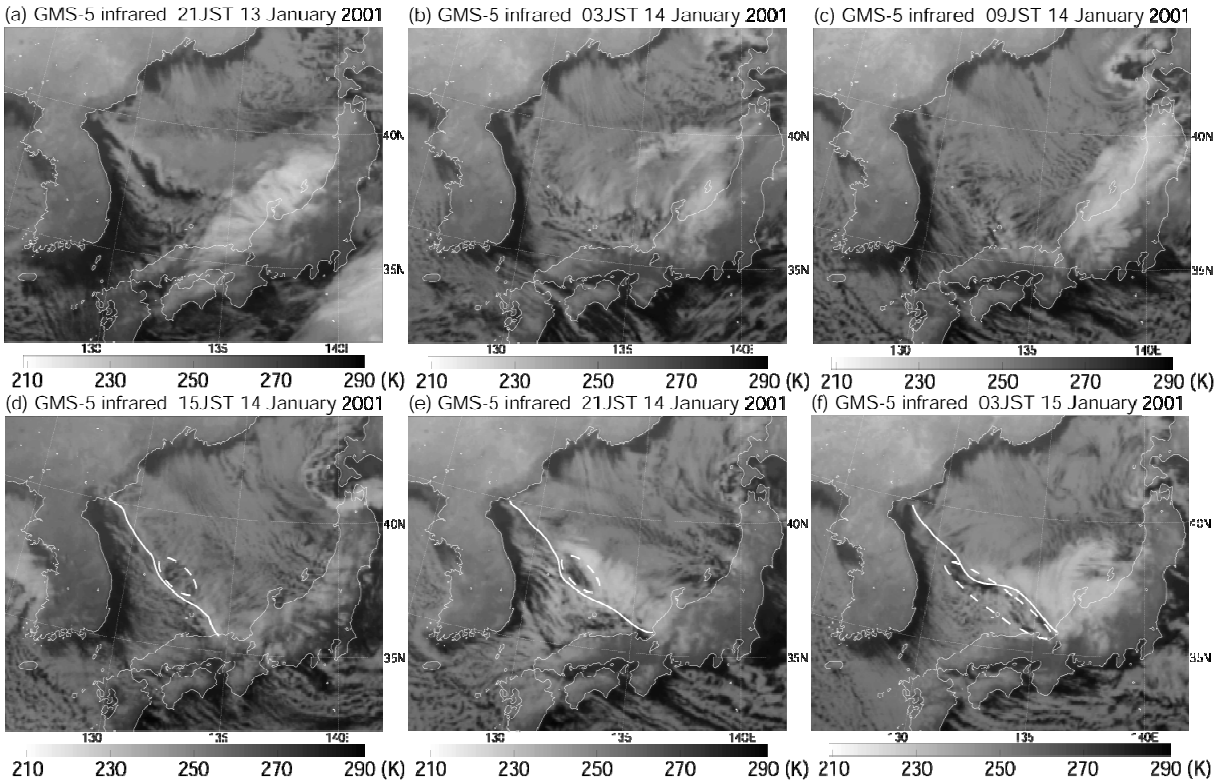


Figure 4.3: Time series of the GMS-5 infrared images every 6 h for the period from 2100 JST on 13 January 2001 to 0300 JST on 15 January 2001. The bold lines in (d), (e), and (f) denote the developed convective cloud band. The dashed ellipses in (d), (e), and (f) present the area with relatively smaller cloud coverage in the JPCZ cloud band.

## 4.3 Observational characteristics of the JPCZ cloud band

In this chapter, the author will focus on the characteristics of the cloud bands embedded in the JPCZ cloud band during the quasi-stationary period of the JPCZ cloud band when the aircraft observation was conducted (Figs. 4.2 and 4.3d). Figure 4.4a shows the zoomed-up image in the rectangle of Fig. 4.2 to

examine the detailed cloud features around the aircraft observation area. Transversal cloud bands extending in a northeast-southwest direction are embedded in the JPCZ cloud band. Figure 4.4b shows the zoomed-up image in the rectangle of Fig. 4.4a to measure the spacing and the orientation of the transversal cloud bands. Averaged band spacing is calculated by counting the number of bands within an interval (100 km) perpendicular to the axis of bands (e.g., Miura 1986). The averaged band spacing is estimated at 8–10 km in the northeastern part of the transversal cloud bands and at 11–14 km in the southwestern part of the transversal cloud bands. There is a tendency for the band spacing to increase toward the southwest. The mean orientation of the transversal cloud bands, which is expressed in degrees from true north, is estimated at about 50°. Detailed features of the developed convective cloud band along the southwestern edge of the JPCZ cloud band is also examined using Fig. 4.4a. The developed convective cloud band is not only single straight cloud band. It consists of line-shaped and arc-shaped cloud bands with a length of about 50 km.

Figure 4.4c is the same as Fig. 4.4a, but for the GMS-5 infrared image. The areas with lower TB are observed in the developed convective cloud band. This suggests that the developed convective cloud band contained developed cumuli or cumulonimbi (e.g., Yagi 1986). In the southeastern part of the developed convective cloud band, the areas with lower TB are broader (see the dotted ellipse in Fig. 4.4c). This suggests that the anvil-like clouds formed around the developed convective cloud (e.g., Yagi 1986), although the extent of the anvil-like clouds is small. The areas with lower TB are also found in the southwestern part of the transversal cloud bands, indicating that the transversal cloud bands well developed. Note that an area with relatively smaller cloud coverage is found in the transversal cloud bands around the developed convective cloud band (see the dashed ellipses in Figs. 4.4a and 4.4c). The transversal cloud bands separate partly from the developed convective cloud band around this area.

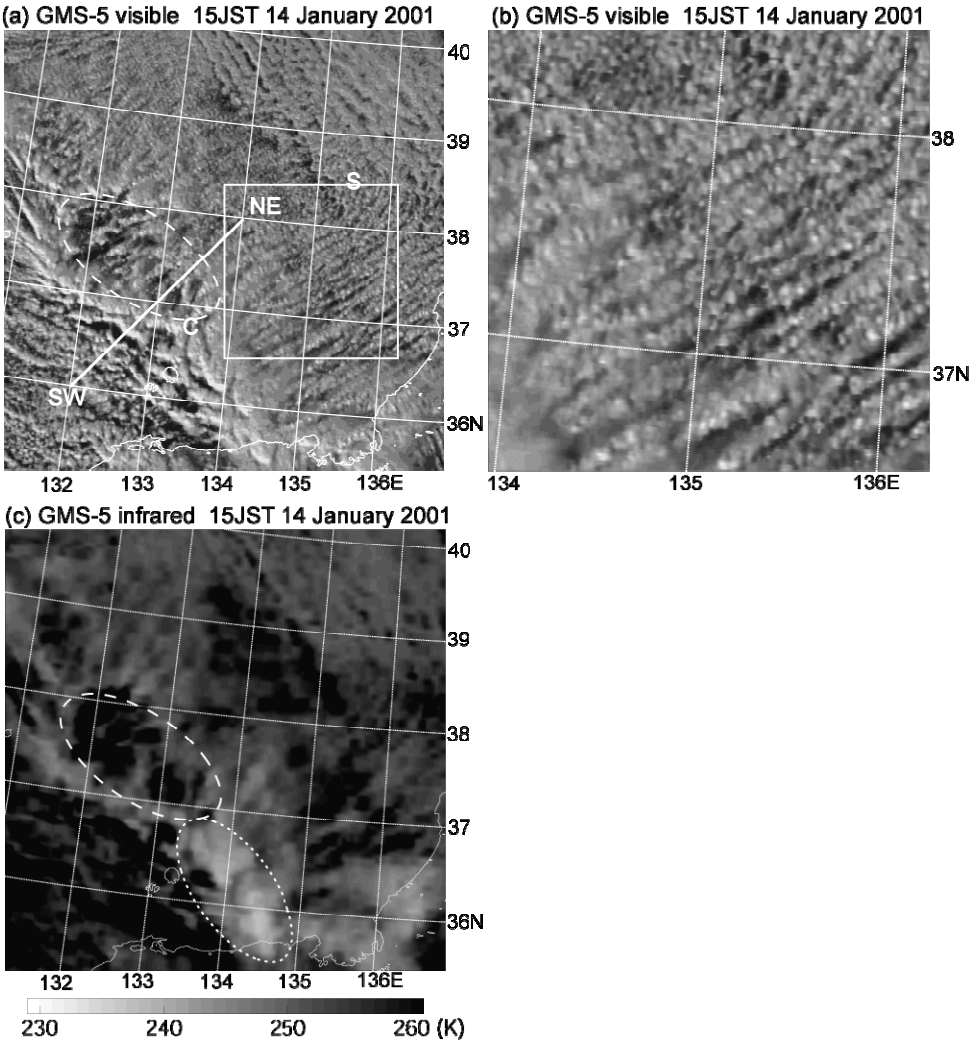


Figure 4.4: (a) GMS-5 visible image at 1500 JST on 14 January 2001. A line SW–NE shows the flight track of the instrumented aircraft. The locations of the Chofu-Maru and the Seifu-Maru, the observational vessels operated by the JMA, at 1500 JST are indicated by symbols of "C" and "S", respectively. (b) The zoomed-up image in the rectangle in (a). (c) GMS-5 infrared image at 1500 JST on 14 January 2001. The dotted ellipse in (c) denotes the area with relatively broader part of the developed convective cloud band. The dashed ellipses in (a) and (c) show the area with relatively smaller cloud coverage in the JPCZ cloud band.

The instrumented aircraft (Gulfstream-II) was operated over the JPCZ cloud band in a southwest-northeast direction at a height of 5.6 km along the line SW–NE in Fig. 4.4a. The flight track with a length of about 200 km is almost

normal to the JPCZ cloud band; therefore, it is almost parallel to the transversal cloud bands. SPIDER measurement with a downward-looking mode was conducted from the Gulfstream-II. SPIDER is a W-band (95 GHz) multi-parameter radar developed by the National Institute of Information and Communications Technology (NICT). The vertical resolution is 150 m. SPIDER is sensitive enough to detect small cloud and ice particles with a diameter of ~10 μm. The Gulfstream-II also performed in situ measurements along a "lawnmower" flight track, consisting of four southwest-northeast flight legs at different heights (2.7, 2.0, 1.1, and 0.3 km). Each individual flight leg was 100–150 km long in the line SW–NE around the transversal cloud bands.

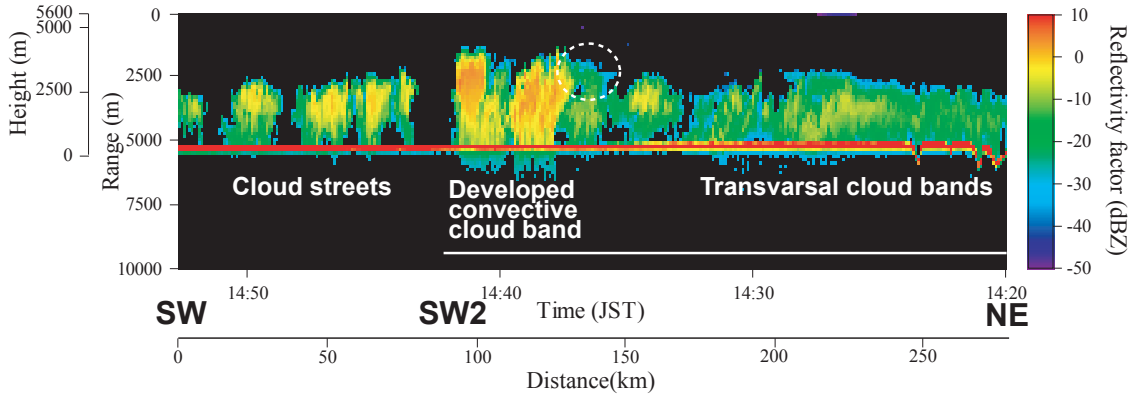


Figure 4.5: Time-height cross section of reflectivity measured with SPIDER installed in the Gulfstream-II that flew at a height of 5.6 km along the line SW–NE shown in Fig. 4.4a. The inner vertical axis indicates the range from the radar. The outer vertical axis indicates the height from the surface. The ranges of 0 m and 5600 m denote the height of 5600m and the surface, respectively. The dashed ellipse denotes weaker radar echoes assumed as the anvil-like clouds. The white line between SW2 and NE indicates the flight leg at a height of 5.6 km shown in Fig. 4.6.

Figure 4.5 shows the vertical cross section of radar reflectivity measured with SPIDER. Between 1437 JST and 1442 JST, tallest radar echoes with a top height of 4.2 km are observed, corresponding to the developed convective cloud band in the JPCZ cloud band. Between 1436 JST and 1438 JST, weaker radar echoes are found between 2.7 km and 3.8 km in height (see the dashed ellipse in Fig. 4.5). They look like anvil clouds extending from the top of the well-developed

clouds in the developed convective cloud band. Between 1420 JST and 1432 JST, radar echoes are continuously captured, corresponding to the transversal cloud band. The radar echoes slant northeastward with height between 1426 JST and 1432 JST, and their axes are slanted about 60° from the vertical. The top heights of radar echoes are 2.5 km around the northeastern edge (point NE) of the radar coverage, and they gradually increase toward the southwest and reached 3.4 km between 1426 JST and 1430 JST. Between 1432 JST and 1436 JST, sparse radar echoes are found, corresponding to the area with relatively smaller cloud coverage, as shown in Figs. 4.4a and 4.4c. Radar echoes with a top height of ~3.3 km are observed after 1443 JST, corresponding to cloud streets on the southwestern side of the JPCZ cloud band.

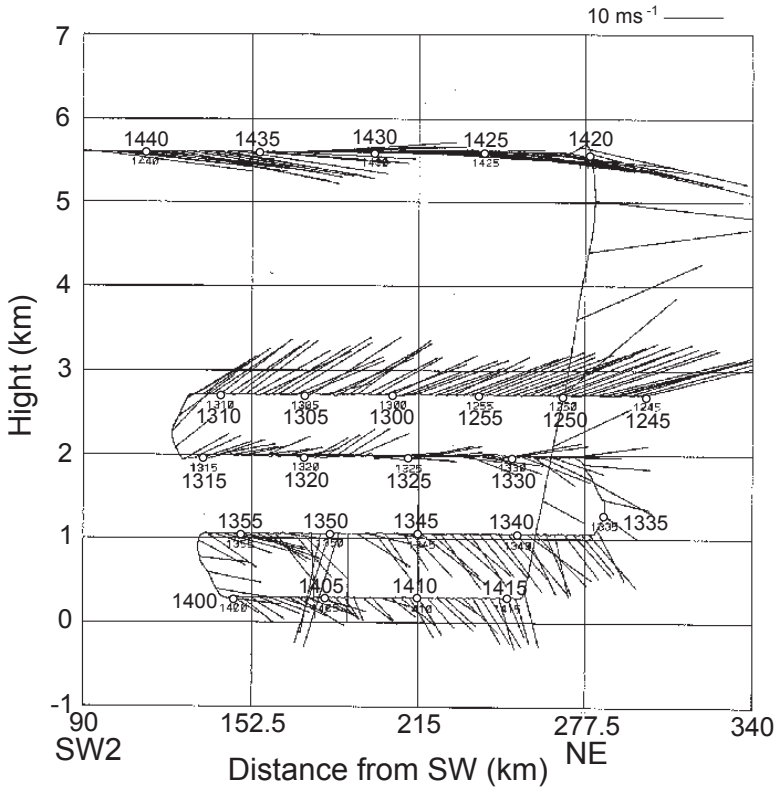


Figure 4.6: Vertical cross section of 1-min averaged horizontal wind velocities observed along the flight legs. Wind barbs point in the direction "toward" which the wind is blowing. The scale of wind speed is denoted on the upper-right side. Numbers shown along each flight leg indicates times of observations (JST). The horizontal axis indicates the distance from the point SW shown in Fig. 4.4a.

Figure 4.6 shows horizontal wind velocities observed along the flight legs in the vertical cross section. The wind direction changes from southwest to west and to northwest–north-northwest as the height decreases from 2.7 to 0.3 km. This indicates that a strong vertical wind shear existed in the area with the transversal cloud bands. Below a height of 2.0 km, the wind direction at each level changes from west-southwest–west-northwest to west-northwest–north-northwest along the flight legs.

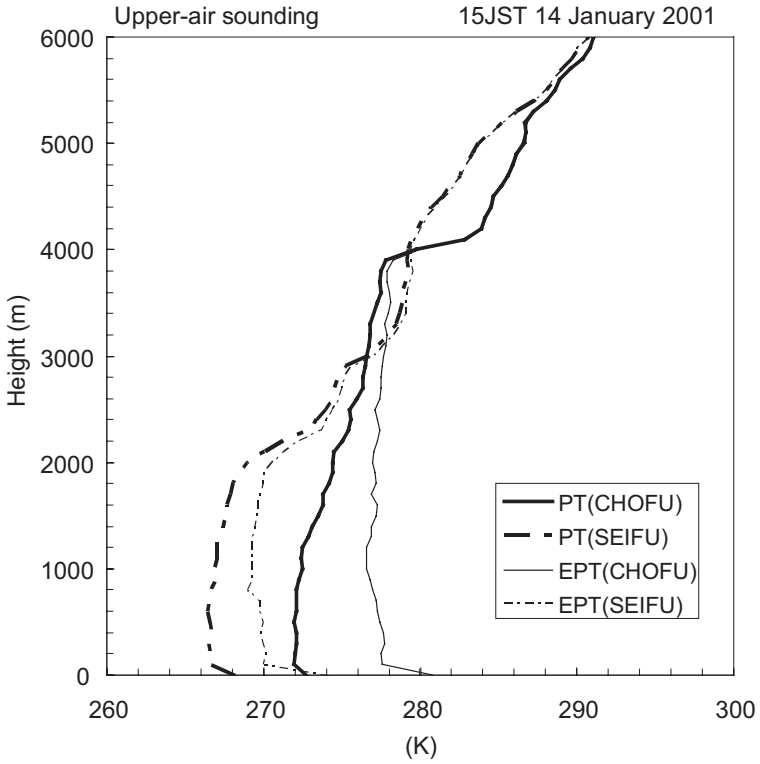


Figure 4.7: Vertical profiles of potential temperature (thick lines) and equivalent potential temperature (thin lines) obtained by upper-air soundings from the Chofu-Maru (solid lines) and the Seifu-Maru (dot-dashed lines) at 1500 JST on 14 January 2001.

Figure 4.7 shows the thermodynamic structures observed by upper-air soundings from two observation vessels (Chofu-Maru and Seifu-Maru) at 1500 JST on 14 January. As shown in Fig. 4.4a, the Chofu-Maru was located around the southwestern edge of the transversal cloud bands near the developed convective cloud band, while the Seifu-Maru was located around the

northeastern edge of the area with the transversal cloud bands near the cloud streets. Over the Chofu-Maru, a convective mixed layer with constant $\theta_e$ developed from the surface to a height of 3.9 km. A convectively unstable layer is observed from the surface to a height of 1.0 km. A strong stable layer is found from a height of 3.9 km to 4.1 km. On the other hand, over the Seifu-Maru, a mixed layer developed from the surface to a height of 2.0 km. A convectively unstable layer is also observed from the surface to a height of 0.8 km. A strong stable layer is found between a height of 2.0 km and 2.2 km. The mixed layer on the southwestern side of the transversal cloud bands developed higher than that on the northeastern side, which is consistent with the tendency of the cloud top heights observed by SPIDER shown in Fig. 4.5. The potential temperature in the mixed layer over the Chofu-Maru was about 5 K higher than that over the Seifu-Maru.

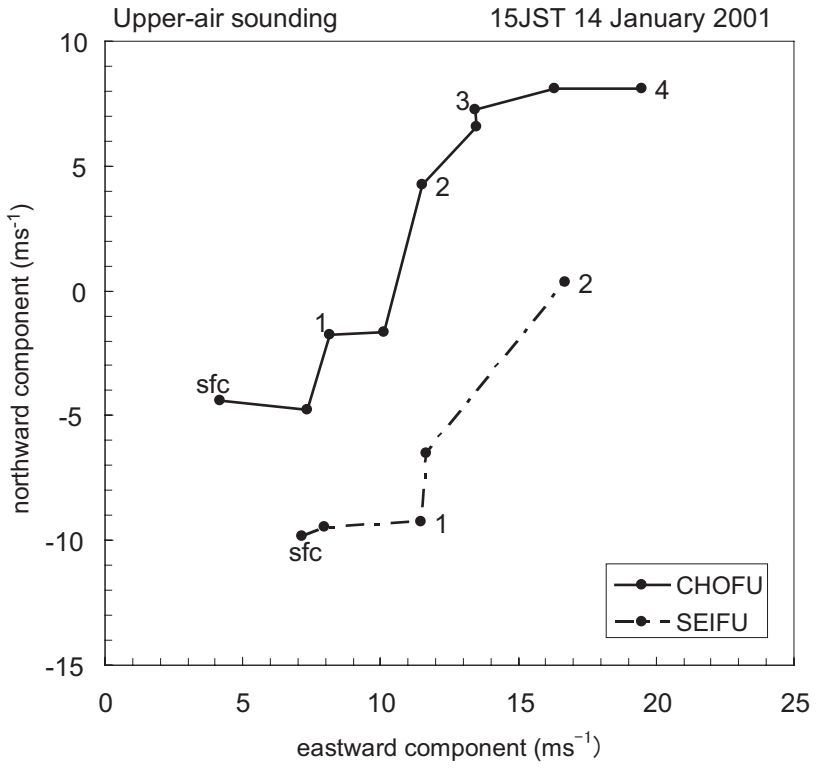


Figure 4.8: Hodographs of horizontal winds obtained by upper-air soundings from the Chofu-Maru (bold line) and the Seifu-Maru (dot-dashed line) at 15 JST on 14 January 2001. Dots are plotted at 0.5-km intervals. The symbol of "sfc" indicates the surface. Heights from the surface are labeled in km, every 1 km.

Figure 4.8 shows hodographs of horizontal winds in the mixed layer over the two vessels at 15 JST on 14 January. Over the Chofu-Maru, the wind direction rotates counterclockwise with height from the northwest to the west-southwest below a height of 3 km, although it rotates clockwise a little with height from a height of 3 km to 4 km. The direction of the vertical wind shear vector from the surface to the top height of the mixed layer (3.9 km) was 43° with respect to true north in the clockwise sense. The direction of the vertical wind shear vector is hereafter expressed in the same manner as above. Its magnitude was observed as $5 \times 10^{-3}$ $s^{-1}$. The wind direction also rotates counterclockwise with height from the north-northwest to the west over the Seifu-Maru. The direction and magnitude of the vertical wind shear vector in the mixed layer (2.0 km) were 43° and $7 \times 10^{-3}$ $s^{-1}$, respectively. The counter-clockwise rotation of the wind direction with height was also observed by in situ aircraft observations (Fig. 4.6). It should be noted that the orientation of the transversal cloud bands is almost parallel to the direction of the vertical wind shear vector.

## 4.4 Numerical simulation

### 4.4.1 Experimental design

The general characteristics of the JMA-NHM simulation as well as the specific options chosen in this chapter are summarized in Table 4.1. They are almost same as those shown in Table 3.1, except for the initial time, the forecast period and domain. This experiment is conducted in area with 2000 $km^2$, which is large enough to cover throughout the JPCZ cloud band. The domain and topography of the experiment is shown in Fig. 4.9. Cloud microphysics scheme is only used for the moist process in the same way as Chapter 3. The initial and boundary conditions are provided from the forecasts of the RSM. The boundary conditions are given by interpolating hourly forecast of the RSM. Daily analysis of the SST with 1.0° latitude/longitude resolution (JMA 2002) is used for a lower boundary condition in sea areas.

Table 4.1: Specification of the JMA-NHM and the experimental configurations in Chapter 4

| | |
|---|---|
| Initial time | 1000 JST, 14 January, 2001 |
| Time step | 5 s |
| Forecast period | 6 h |
| Horizontal mesh (resolution) | 2000 × 2000 (1 km) |
| Levels | 38 terrain-following stretched levels from 40 m to 1090 m |
| Model top | 20.36 km |
| Moist physics | bulk scheme, three-class ice (Ikawa and Saito 1991 based on Lin et al. 1983, Murakami 1990 and Cotton et al. 1986) |
| Surface | Bulk method (Ikawa and Saito 1991 based on Kondo 1975 and Sommeria 1976) |
| Turbulence | Diagnostic TKE scheme (Ikawa and Saito 1991 based on Deardorff 1980) |
| Radiation | Long and short wave radiation scheme for cloud optical properties with empirical constant (Saito et al. 2001 based on Sugi et al. 1990) |

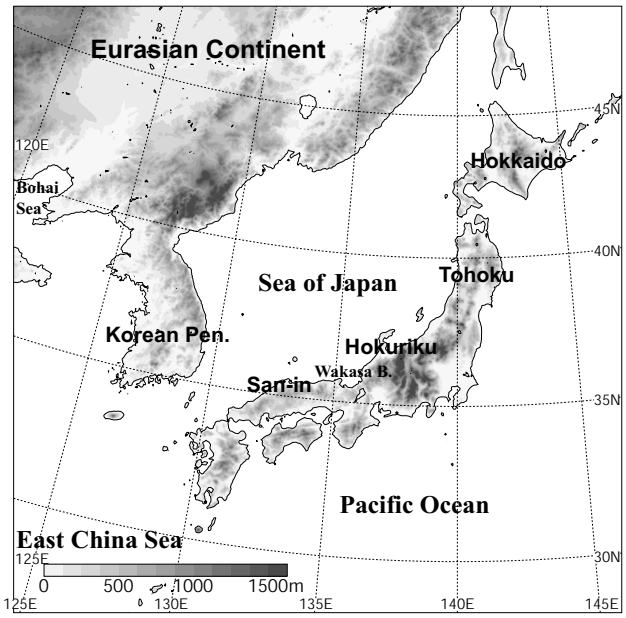


Figure 4.9: Domain and topography of numerical simulation.

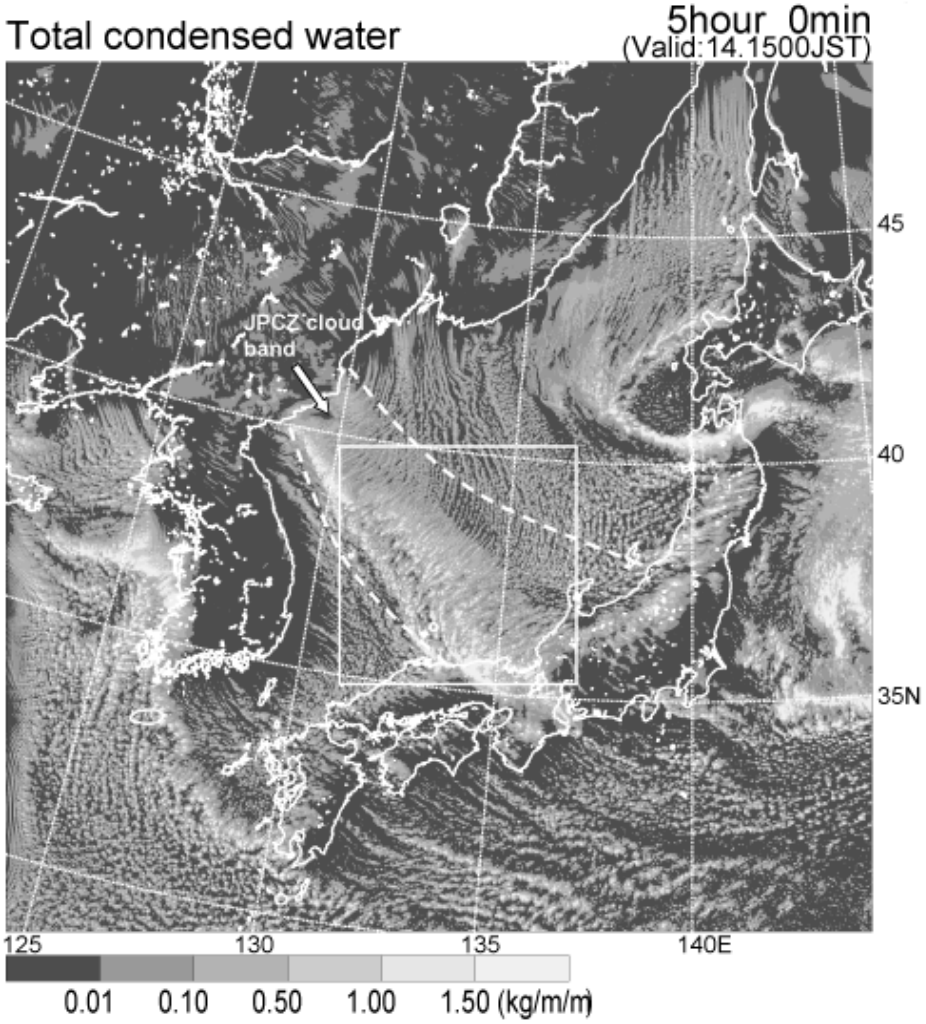


Figure 4.10: Horizontal distributions of vertically integrated total condensed water content (kg $m^{-2}$) simulated by the JMA-NHM at 1500 JST on 14 January 2001 (5-h forecast). The rectangle corresponds to the display area in Fig. 4.11. Two dashed lines denote the boundaries of the JPCZ cloud band.

### 4.4.2 Comparison of simulation with observation

The initial time of the JMA-NHM is 1000 JST on 14 January 2001 (1-h forecast of the RSM), which is about 5 h before the aircraft observations. In the initial field (not shown), the JPCZ was presented over the Sea of Japan from the base of the Korean Peninsula to Wakasa Bay. The calculation is performed for 6 h until 1600 JST on 14 January 2001, which is about 1 h after the aircraft observations. The simulated JPCZ cloud band has remained quasi-stationary

between forecast time (FT) = 4 and 6 h (not shown) after spin up time of the JMA-NHM, which is the time required to produce a realistic amount of cloud and precipitation particles in the beginning of the forecast period. Therefore, simulation results at FT = 5 h (1500 JST on 14 January 2001), which is near the time of the aircraft observations, are only presented here.

Figure 4.10 shows the horizontal distribution of vertically integrated total condensed water content simulated by the JMA-NHM at 1500 JST. Total condensed water refers to the sum of cloud water, cloud ice, rain, snow, and graupel. The JMA-NHM successfully reproduces cloud features around the Sea of Japan observed by the GMS-5 (Fig. 4.2). The JPCZ cloud band extending southeastward from the base of the Korean Peninsula is well-reproduced. Cloud streets are also simulated on both sides of the JPCZ cloud band.

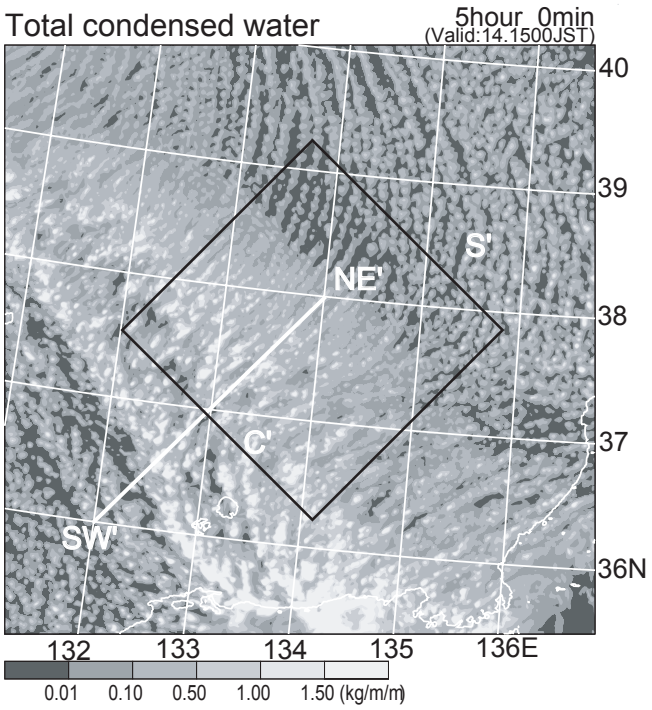


Figure 4.11: Horizontal distributions of vertically integrated total condensed water content (kg $m^{-2}$) simulated by the JMA-NHM at 1500 JST on 14 January 2001 (5-h forecast). The line SW′–NE′ is the flight track of the instrumented aircraft, same as the line SW–NE shown in Fig. 4.4. The locations of the Chofu-Maru and the Seifu-Maru at 1500 JST are indicated by the symbols of "C′" and "S′", same as "C" and "S", respectively, in Fig. 4.4. The rectangle corresponds to the display area in Fig. 4.15.

The zoomed-up image in the rectangle of Fig. 4.10, the same area as that in Fig. 4.4, is shown in Fig. 4.11 to examine the detailed structures of the model-simulated JPCZ cloud band. The JMA-NHM successfully reproduces characteristics of the cloud bands embedded in the JPCZ cloud band that are found in the GMS-5 observations (Fig. 4.4a): the developed convective cloud band along the southwestern edge of the JPCZ cloud band and the transversal cloud bands extending to the northeast from the developed convective cloud band. Moreover, the spacing between the simulated transversal cloud bands and their orientation are similar to those observed by the GMS-5 (Fig. 4.4a). The area with relatively smaller cloud coverage (see dashed ellipses in Figs. 4.4a, 4.4c) is reproduced around the developed convective cloud band. Cloud streets around the JPCZ cloud band are also reproduced on the southwestern side of the developed convective cloud band.

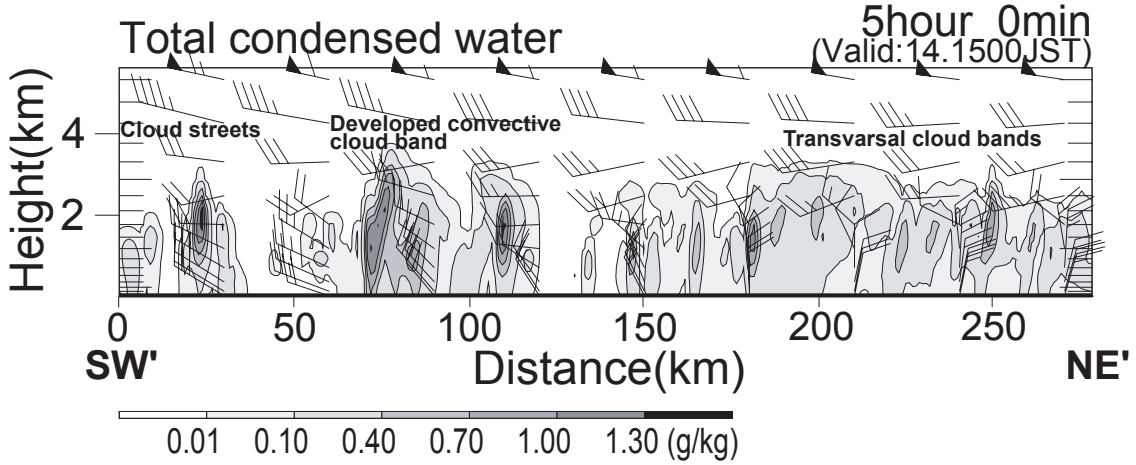


Figure 4.12: Vertical cross section of mixing ratio of simulated total condensed water (g $kg^{-1}$) along the line SW′–NE′ shown in Fig. 4.11 at 1500 JST on 14 January 2001. Wind barbs denote horizontal wind velocity; half, full, and triangle-shaped barbs mean 2.5 m $s^{-1}$, 5 m $s^{-1}$, and 25 m $s^{-1}$, respectively.

Figure 4.12 shows the vertical cross section of the simulated total condensed water mixing ratio along the line SW′–NE′ shown in Fig. 4.11. The horizontal axis in Fig. 4.12 indicates distance from the point SW′. The developed convective cloud band corresponds to the tallest simulated cloud with a top height of 3.8 km between a distance of 70 km and 120 km. The transversal cloud

band is simulated between a distance of 140 km and the point NE′. The cloud-top height gradually becomes higher toward the southwest from 2.5 km around the point NE′ to 3.3 km around a distance of 180 km to 220 km. The clouds in the simulated transversal cloud band tilt northeastward with height between a distance of 180 km and the point NE′. The axes of clouds are slanted about 50° from the vertical. The sparse cloud area is also simulated between a distance of 120 km and 140 km. The cloud streets with a top height of 3.2 km are simulated between the point SW′ and a distance of 40 km. These characteristic features of the simulated clouds almost correspond to those obtained from the SPIDER observations shown in Fig. 4.5, although the cloud-top heights are a little lower than the observation. Anvil-like clouds are not found around the top of the well-developed clouds in the simulated developed convective cloud band.

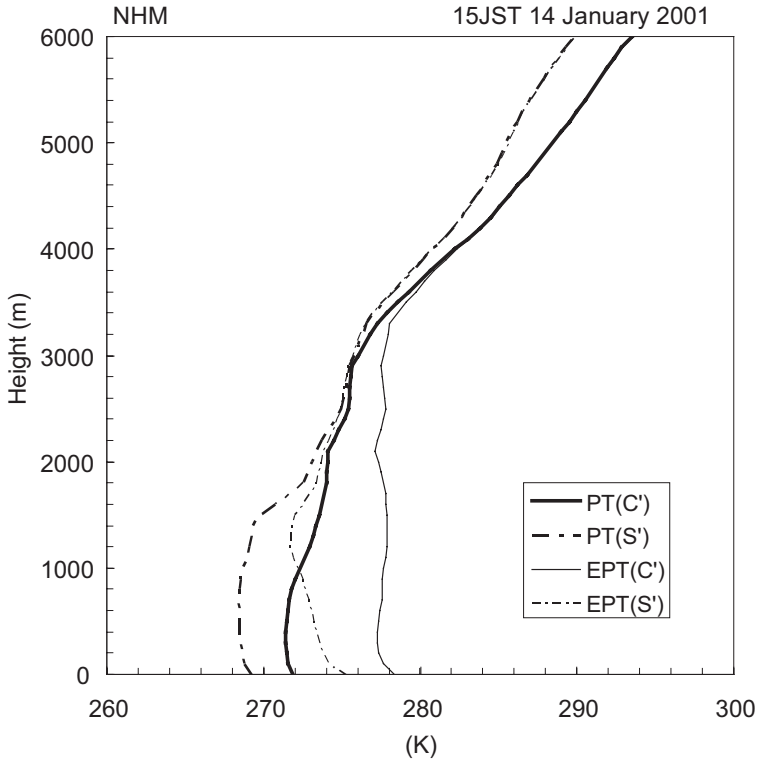


Figure 4.13: Vertical profiles of potential temperature (thick lines) and equivalent potential temperature (thin lines) at the point C′ (solid lines) and the point S′ (dot-dashed lines) in Fig. 4.11.

Horizontal wind velocities in the vertical cross-section are also shown in Fig. 4.12. The wind direction in the mixed layer rotates counterclockwise with height from the northwest to the southwest in the area with the transversal cloud bands, denoting the existence of the strong vertical wind shear. These features almost agree with those of the in-situ aircraft observations (Fig. 4.6).

Figure 4.13 shows the simulated thermodynamic structures at the same time and location as those of upper-air soundings from two observation vessels (Fig. 4.7). The depth of the simulated mixed layer is 3.3 km over the same location of the Chofu-Maru ("C′" in Fig. 4.11). A strong stable layer is found from a height of 3.3 km to 3.8 km. A convectively unstable layer is simulated from the surface to a height of 0.4 km. On the other hand, the depth of the simulated mixed layer is 1.5 km over the same location of the Seifu-Maru ("S′" in Fig. 4.11), and a strong stable layer is found between a height of 1.5 km and 1.8 km. A convectively unstable layer is simulated from the surface to a height of 1.2 km. Compared with observations (see Fig. 4.7), the depths of the simulated mixed layer are a little shallower at both points. However, the JMA-NHM fairly reproduces qualitative characteristics of the observed thermodynamic structures.

Figure 4.14 shows the hodographs of the simulated horizontal wind in the mixed layer at the same time and location as those in Fig. 4.13. Over the same location of the Chofu-Maru, the wind direction rotates counterclockwise with height from the northwest to the west-southwest below a height of 3 km. This feature corresponds to that obtained from upper-air sounding (Fig. 4.8). However, the wind direction largely rotates clockwise with height from the southwest to the west above a height of 3 km. This difference between the observation and the simulation could be caused by the shallower depth of the simulated mixed layer (Fig. 4.13). It is also possibly caused by the shift of the rawinsonde advected by the horizontal wind. The simulated wind speed near the surface is a little weaker than the observation. The direction and magnitude of the vertical wind shear vector from the surface to the top height in the simulated mixed layer are estimated at $52^{o}$ and $4 \times 10^{-3}$ $s^{-1}$, respectively. The same characteristic features of the simulated wind direction are found over the location of the Seifu-Maru. The direction and magnitude of the vertical wind shear vector in the simulated mixed layer are estimated at $52^{o}$ and $8 \times 10^{-3}$ $s^{-1}$, respectively. These results are similar to the observation. Moreover, the

simulation results also show that the vertical wind shear vector is almost parallel to the orientation of the transversal cloud bands.

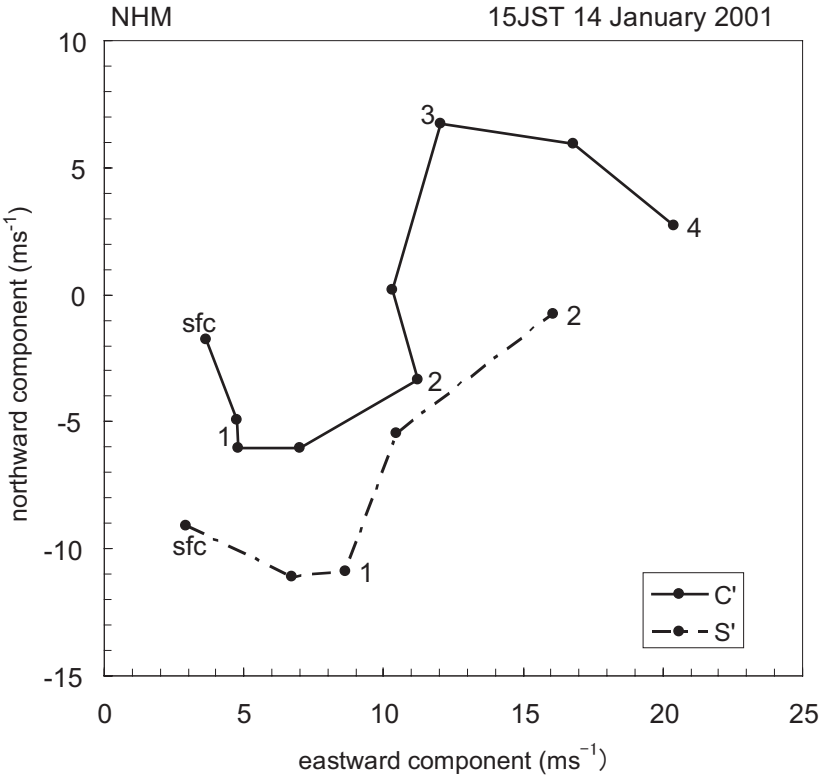


Figure 4.14: Hodographs of the winds at the point C′ (bold line) and the point S′ (dot-dashed line) in Fig. 4.11. Dots are plotted at 0.5-km intervals. The symbol of "sfc" indicates the surface. Heights from the surface are labeled in km, every 1 km.

As described above, the JMA-NHM successfully reproduces the qualitative characteristics of the observed JPCZ cloud band. Therefore, the structure and formation mechanisms of the transversal cloud bands are examined from the simulation results in the next subsection. However, there are some quantitative differences between the observation and the simulation results. As mentioned above, the JMA-NHM underestimates a depth of the mixed layer in comparison with the observations. This underestimation could be brought about from the lack of the horizontal resolution in this numerical experiment or the weak diffusion in the simulated planetary boundary layer. Weaker diffusion cannot cause enough downward transportation of the upper-level large momentum and

upward transportation of moisture from the surface; therefore, the underestimation of a depth of the convective mixed layer could be caused by the weaker diffusion.

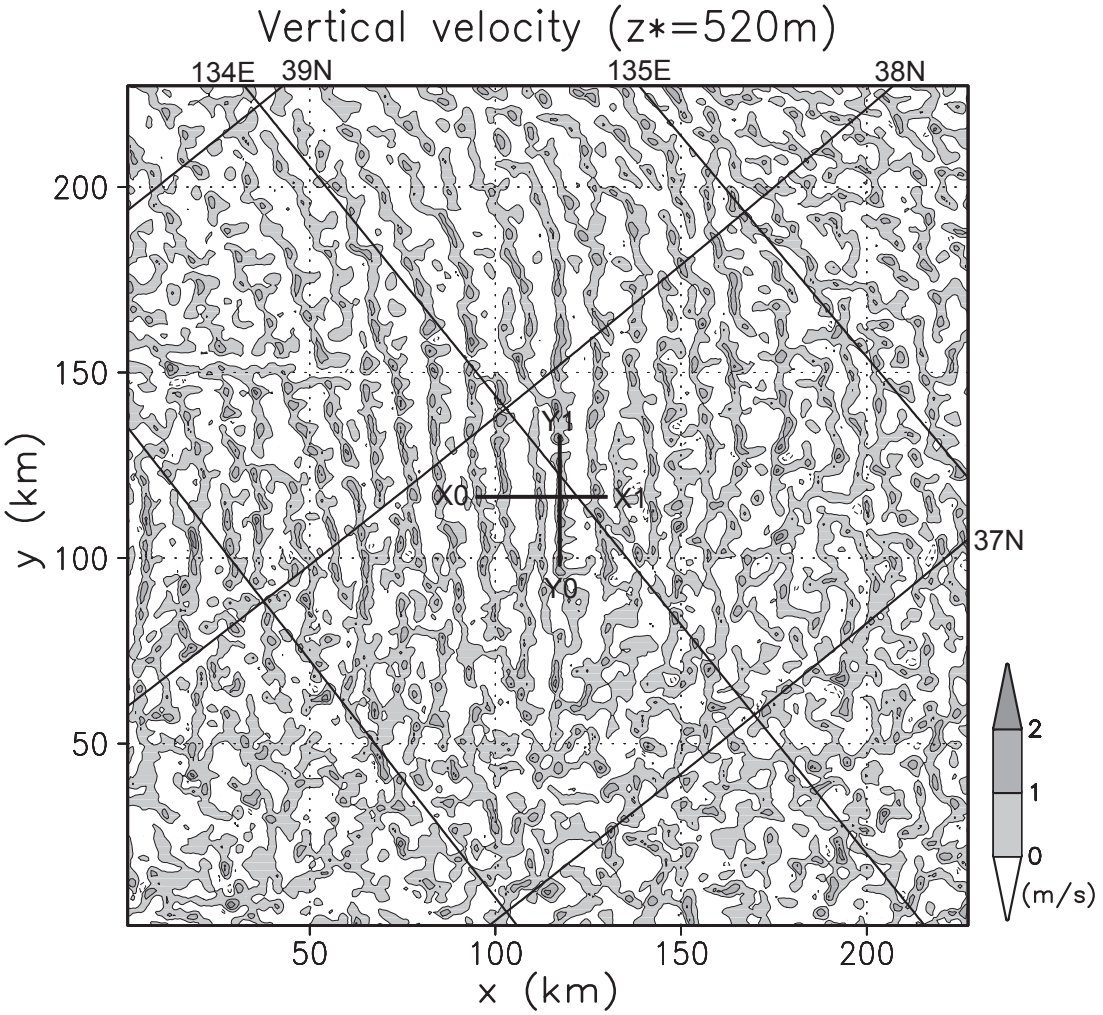


Figure 4.15: Horizontal distributions of simulated vertical velocity (m $s^{-1}$) at a height of 0.52 km at 1500 JST on 14 January 2001.

### 4.4.3 Structures of the transversal cloud bands

Figure 4.15 show the vertical velocity field at a height of 0.52 km in the area of the transversal cloud bands. Cellular and wavelike patterns are found in the vertical wind field, which well correspond to cloud patterns detected from the total condensed water field (Fig. 4.11). Wavelike patterns are evident in the northeastern part of the transversal clouds, and they gradually become obscure

toward the southwest.

In order to examine the structures of the transversal cloud bands, the author defines a Cartesian coordinate system (*x, y, z*) with the *x* and *y* axes normal and parallel to the transversal cloud bands, respectively (see Fig. 4.15). The *x* and *y* axes almost points southeastward and northeastward, respectively. The *z* axis goes vertically upward. Using anelastic approximation for simplicity, the momentum equation in the (*x, y, z*) coordinate system is written in the form as

$$\frac{d\mathbf{v}}{dt} + f\mathbf{k} \times \mathbf{v} = -\frac{\mathbf{1}}{\rho_0}\nabla p + b\mathbf{k} + \mathbf{D}, \tag{1}$$

where $\mathbf{v} = (u, v, w)$ denotes the Cartesian wind components, $\mathbf{k}$ is the unit vector in the *z* direction, *f* is the Coriolis parameter, *p* and *b* are pressure and buoyancy deviations, respectively, from their basic hydrostatic state, and $\mathbf{D}$ is the parameterized subgrid-scale transport. Here, $\rho_0$ is the density of basic state and is the horizontal area average over the full domain shown in Fig. 4.15. Density $\rho$ is defined as the sum of the masses of moist air and the condensed water substances per unit volume. The buoyancy deviation *b* is defined as $b \equiv -g(\rho - \rho_0)/\rho_0$, where *g* is the magnitude of the gravitational acceleration.

Since the wavelike structure is dominant in the *x*-direction, it is convenient to decompose the variables into *x* averages and deviations from them (e.g., Kawashima and Fujiyoshi 2005; Kawashima 2007). A given variable $\phi$ is decomposed as

$$\phi(x, y, z, t) = \bar{\phi}(y, z, t) + \phi'(x, y, z, t), \tag{2}$$

where the overbar represents the value averaged in *x*-direction over the full domain width (~200 km) in Fig. 4.15 and the prime represents the deviation from that average and will be referred to as the eddy part of $\phi$. The value averaged horizontally over the full domain shown in Fig. 4.15 is also defined as $\bar{\phi}^{xy}(z,t)$.

Figure 4.16a shows the vertical profiles of mean cross-band horizontal velocity ($\bar{u}^{xy}$) and mean along-band horizontal velocity ($\bar{v}^{xy}$). The mean along-band wind has a profile with positive vertical shear, which almost points northeastward, below a height of 3 km. An inflection point is also found around a height of 1.5 km in the vertical profile of $\bar{v}^{xy}$. There is no remarkable vertical shear below a height of 3.5 km in the vertical profile of $\bar{u}^{xy}$. The vertical profiles of mean thermodynamic structures are shown in Fig. 4.16b. There is an

instability layer below a height of 1 km.

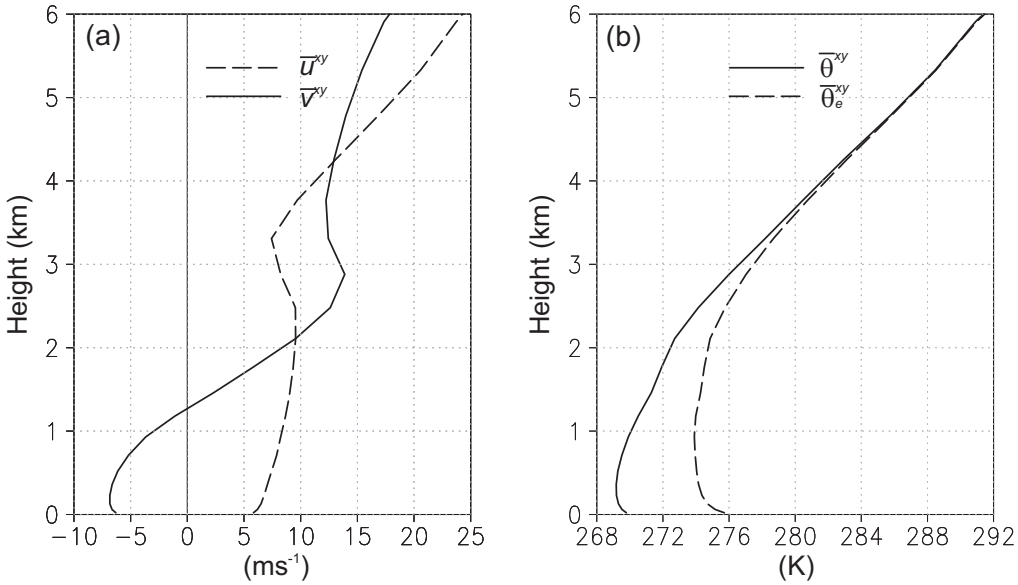


Figure 4.16: (a) Vertical profiles of mean cross-band horizontal velocity ($\overline{u}^{xy}$) and mean along-band horizontal velocity ($\overline{v}^{xy}$).The variables are averaged horizontally over the full domain shown in Fig. 4.15. (b) Same as (a), except for mean potential temperature ($\overline{\theta}^{xy}$) and mean equivalent potential temperature ($\overline{\theta_e}^{xy}$).

Figure 4.17 shows the eddy parts of vertical velocity ($w'$), buoyancy ($b'$), cross-band horizontal velocity ($u'$), and along-band horizontal velocity ($v'$) in the vertical cross-sections along the line X0–X1 in Fig. 4.15. The magnitude of $w'$ is large between a height of 0.2 km and 1.5 km (Fig. 4.17a). Updraft cores are associated with the large mixing ratio of total condensed water. The averaged spacing between updraft cores is estimated at 8 km. The eddy part of buoyancy ($b'$) is nearly in phase with $w'$ (i.e., $\overline{b'w'} > 0$) below a height of 0.5 km (Fig. 4.17b), where amplitude of $b'$ is large in the instability layer (see Fig. 4.16b). This indicates that the kinetic energy of the perturbation is created by thermally direct flow perturbations through the upward transport of heat. The magnitude of $u'$ is largest near the surface (not shown). In this cross section, a phase shift of ~ 90° is found between $w'$ and $u'$ below a height of 1.5 km (i.e., $\overline{u'w'} \sim 0$), where streamlines of eddy velocities $(u', w')$ in the cross section form roll circulations (Fig. 4.17c). The eddy part of the along-band velocity ($v'$) is almost in antiphase with $w'$ (i.e., $\overline{v'w'} < 0$) below a height of 1.5 km (Fig. 4.17d). This indicates that the kinetic energy of the mean along-band wind is transferred to

the perturbation through the downward transport of along-band momentum because the mean along-band wind has a profile with positive vertical shear below a height of 3 km (Fig. 4.16a).

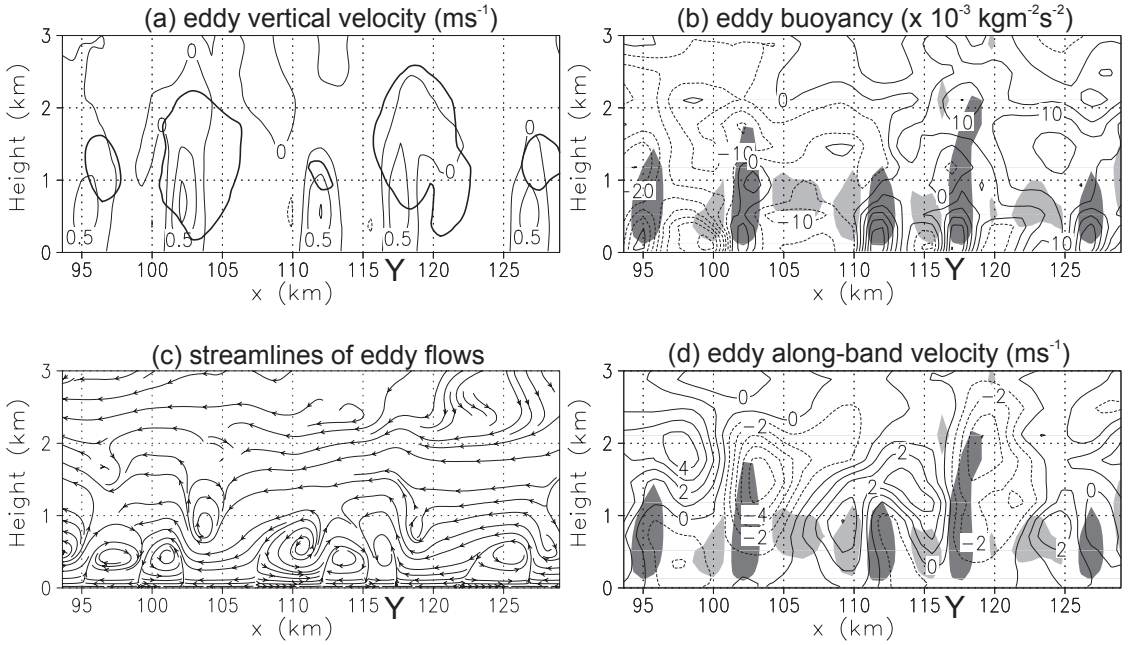


Figure 4.17: Vertical cross sections along the line X0–X1 in Fig. 4.15 showing the eddy parts of (a) vertical velocity ($w'$; 0.5 m $s^{-1}$ contour interval), (b) buoyancy ($b'$; 5 × $10^{-3}$ kg $m^{-2}$ $s^{-2}$ contour interval), (c) streamlines of eddy velocity vectors $(u', w')$ in the plane of the cross section, and (d) along-band velocity ($v'$; 1.0 m $s^{-1}$ contour interval). The variables are averaged in y over the 10-km width across the line X0–X1. The regions enclosed by the thick contours in (a) represent the area where the mixing ratio of total condensed water exceeds 0.1 g $kg^{-1}$. The eddy parts of vertical velocity greater than 0.3 m $s^{-1}$ (less than –0.3 m $s^{-1}$) is heavily (lightly) shaded in (b) and (d). The symbol of "Y" indicates the location of the line Y0–Y1 in Fig. 4.15.

The vertical cross sections parallel to the transversal cloud bands along the line Y0-Y1 in Fig. 4.15 are shown in Fig. 4.18. The cross sections are located in the upward branch of the roll circulation shown in Fig. 4.17c. As shown in Fig. 4.17a, updraft cores are distributed below a height of 2 km and are associated with the large mixing ratio of total condensed water (Fig. 4.18a). The clouds slant with height toward the downshear-side (see Fig. 4.16a). The downwshearward tilt of the clouds is caused by the differential advection due to the vertical shear of the mean along-band wind. The distribution of $v'$ (Fig. 4.18b) shows that negative along-band velocities are found in the clouds as

found in the cross-band vertical cross sections (Fig. 4.17d). The streamlines of eddy velocities in the cross section have an upshearward tilt with height (Fig. 4.18c). In the cross section located in the downward branch of the roll circulation, streamlines of positive $v'$ and negative $w'$ also have an upshearward tilt with height (not shown). This indicates that the roll circulations formed of the eddy velocities tilt with height toward the upshearside. The direction is opposite to the slant direction of the clouds. Note that the vertical velocity perturbation field also exhibits wavelike structures above a height of 2 km (Fig. 4.18a). The disturbances are gravity waves generated by convection.

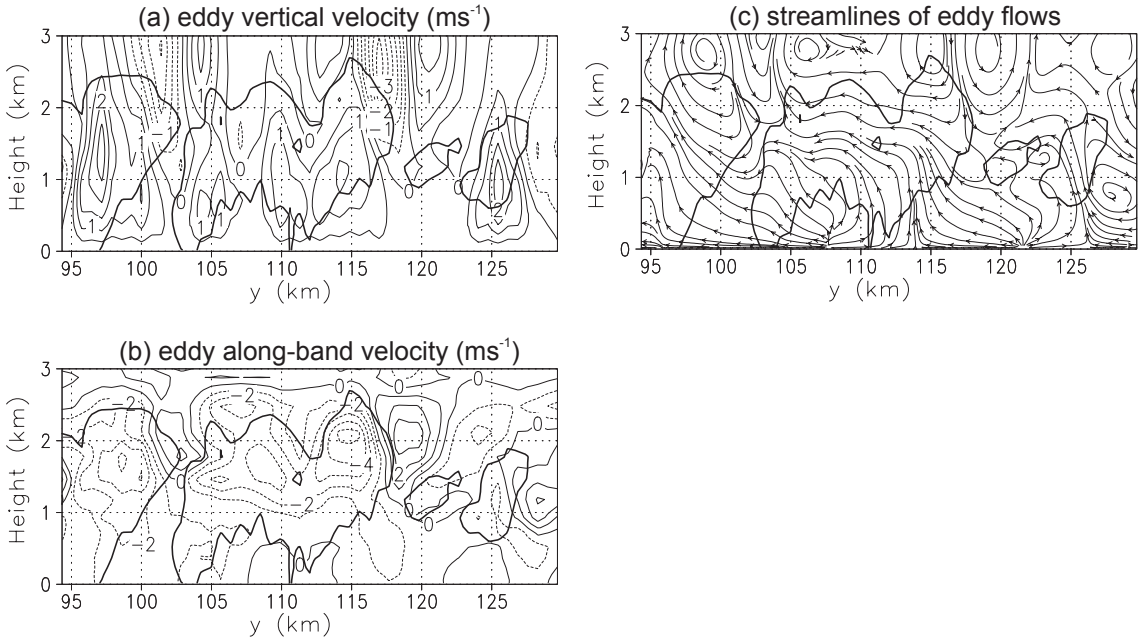


Figure 4.18: Vertical cross sections along the line Y0–Y1 in Fig. 4.15 showing the eddy parts of (a) vertical velocity ($w'$; 0.5 m $s^{-1}$ contour interval), (b) along-band velocity ($v'$; 1.0 m $s^{-1}$ contour interval), and (c) streamlines of eddy velocity vectors $(v', w')$ in the plane of the cross section. The regions enclosed by the thick contours represent the area where the mixing ratio of total condensed water exceeds 0.2 g $kg^{-1}$.

As stated above, the perturbation analysis shows that the transversal cloud bands are accompanied by roll circulations. The characteristics of the roll circulations shown in Figs. 4.17 and 4.18 are also found in the other place where the transversal cloud bands are present. However, the roll circulations become deep and wide toward the southwestern part of the area with the transversal cloud bands, as the mixed layer becomes deep.

### 4.4.4 Energetics of the roll circulations

To investigate the mechanism responsible for the formation of the roll circulations, the eddy kinetic energy (EKE) budget analysis is conducted in this subsection (e.g., Kawashima and Fujiyoshi 2005; Kawashima 2007). Taking $\mathbf{v}' \cdot$Eq. (1) and then averaging both sides of the equation in $x$ leads to the following eddy kinetic energy equation:

$$\begin{aligned}\frac{\partial \overline{K_e}}{\partial t} = & \underbrace{-\overline{v_i' v'} \frac{\partial \overline{v_i}}{\partial y}}_{\text{HSP}} \underbrace{-\overline{v_i' w'} \frac{\partial \overline{v_i}}{\partial z}}_{\text{VSP}} \underbrace{+\overline{b' w'}}_{\text{BP}} \\ & \underbrace{-\frac{1}{\rho_0} \overline{\mathbf{v}' \cdot \nabla p'}}_{\text{PG}} \underbrace{-\left( \overline{v} \frac{\partial}{\partial y} + \overline{w} \frac{\partial}{\partial z} \right) \overline{K_e}}_{\text{ADV}} \\ & \underbrace{-\overline{\mathbf{v}' \cdot \nabla K_e}}_{\text{ET}} - \text{dissipation terms},\end{aligned} \tag{3}$$

where $i$ = 1, 2, 3; ($v_1$, $v_2$, $v_3$) = ($u$, $v$, $w$); and $\overline{K_e}$ is the EKE averaged in $x$-direction given by $\overline{K_e} = (\overline{u'^2} + \overline{v'^2} + \overline{w'^2})/2$. Here, summation over repeated $i$ indices is assumed. In this equation, HSP (VSP) represents the horizontal (vertical) shear production; BP, the buoyant production; PG, the production (destruction) of the EKE by the eddy flows $\mathbf{v}'$ from high to low (low to high) pressure; ADV, the advection of the EKE by the mean flow $(\overline{v}, \overline{w})$; and ET, the eddy transport of the EKE. Among these energy conversion terms, HSP, VSP, and BP may have net contributions to the total EKE increase/decrease (e.g., Kawashima 2007).

Figure 4.19 shows the vertical profiles of the mean EKE and terms HSP, VSP, and BP averaged horizontally over the full domain shown in Fig. 4.15. The large EKE distributes below a height of 4 km with a maximum near a height of 2 km. Although not shown, the EKE stays fairly constant between FT = 4 and 6 h after spin up time of the JMA-NHM. The term VSP has positive values between a height of 0.5 km and 3.0 km and has larger amplitude than BP and HSP, indicating that it is the primary energy source responsible for maintenance of the roll circulations. Among the three components of VSP (i.e., $-\overline{u'w'}\partial\overline{u}/\partial z$, $-\overline{v'w'}\partial\overline{v}/\partial z$, and $-\overline{w'w'}\partial\overline{w}/\partial z$), the terms $-\overline{u'w'}\partial\overline{u}/\partial z$, and $-\overline{w'w'}\partial\overline{w}/\partial z$ have a considerably smaller amplitude than the term $-\overline{v'w'}\partial\overline{v}/\partial z$ (not shown). Therefore, the energy conversion from the mean along-band wind ($-\overline{v'w'}\partial\overline{v}/\partial z$) contributes greatly to the vertical shear production. The term BP, which distributes below a height of 1 km, is the second-most important energy source.

The term HSP has a considerably smaller amplitude than the terms VSP and BP, making little contribution to the maintenance of the EKE.

As described above, the energetics analysis suggests that the roll circulations, which are responsible for the transversal cloud bands, are maintained by the combined effects of vertical shear and unstable stratification in the mixed layer.

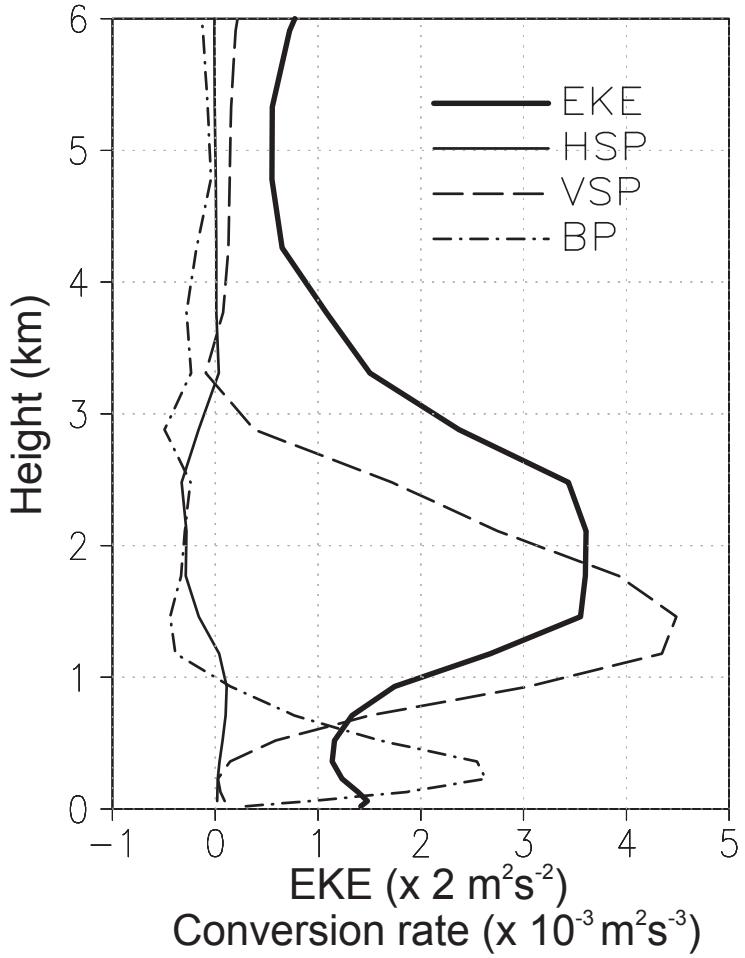


Figure 4.19: Vertical profiles of EKE ($\times$ 2 $m^2s^{-2}$) and primary energy conversion terms (HSP, VSP, and BP; $\times$ $10^{-3}$ $m^2s^{-3}$) averaged horizontally over the full domain shown in Fig. 4.15.

## 4.5 Discussion

The observation and simulation results indicate that the transversal cloud bands mainly consisted of convective clouds in the mixed layer. The simulation results also indicate that the transversal cloud bands could be generated by the roll circulations in unstably stratified shear flows. Asai (1972) investigated the nature of instability in unstably stratified shear flows turning the direction with height, which is a similar situation in this case. He showed that two different types of instability are obtained in the case of directional shear flows with points of inflection as in the unidirectional shear flow case shown in Asai (1970b). One is the shear-perpendicular mode driven primary by the vertical shear and the other is the shear-parallel mode driven by the buoyancy. The temporal evolutions of the roll circulations are not clear in the present experiment; therefore, it is inappropriate to relate the roll circulations simply with the instability modes presented by Asai (1972). Nevertheless, the present analyses show that the structures and energetics of the roll circulations qualitatively resemble those associated with the instability wave driven by the thermal instability modified by a shear flow. This also supports the formation mechanism of the transversal cloud bands proposed by Yagi et al. (1985).

The previous studies have shown that an optimal combination of buoyancy and vertical wind shear is important for the existence of roll circulations in the mixed layer (e.g., Deardorff 1972; Grossman 1982; LeMone 1973; Sykes and Henn 1989). They used the Monin–Obukhov length $L$ and the ratio $-z_i / L$, where $z_i$ is the depth of the mixed layer, to define the necessary conditions for the occurrence of roll circulations. The Monin–Obukhov length is proportional to the height above the surface at which buoyancy dominates over shear in the production of turbulence, and is negative for unstable surface layers; therefore, $-L$ is a measure of convective instability. Larger (smaller) $-L$ indicates less (more) convectively unstable boundary layers. The ratio $-z_i / L$ is also used to quantify the stability of the mixed layer. High values of $-z_i / L$ are associated with free convection and the existence of cellular pattern consistent with thermals, and low values of $-z_i / L$ are associated with forced convection and in some cases, the existence of roll circulations. Grossman (1982) observed that roll circulations tended to form when $-z_i / L$ was less than 21.4. Most of other

previous studies (e.g., Deardorff 1972; LeMone 1973; Sykes and Henn 1989) showed that their criterions for $-z_i / L$ were smaller than that of Grossman (1982), suggesting that roll circulations will be dominant within a slightly unstable mixed layer.

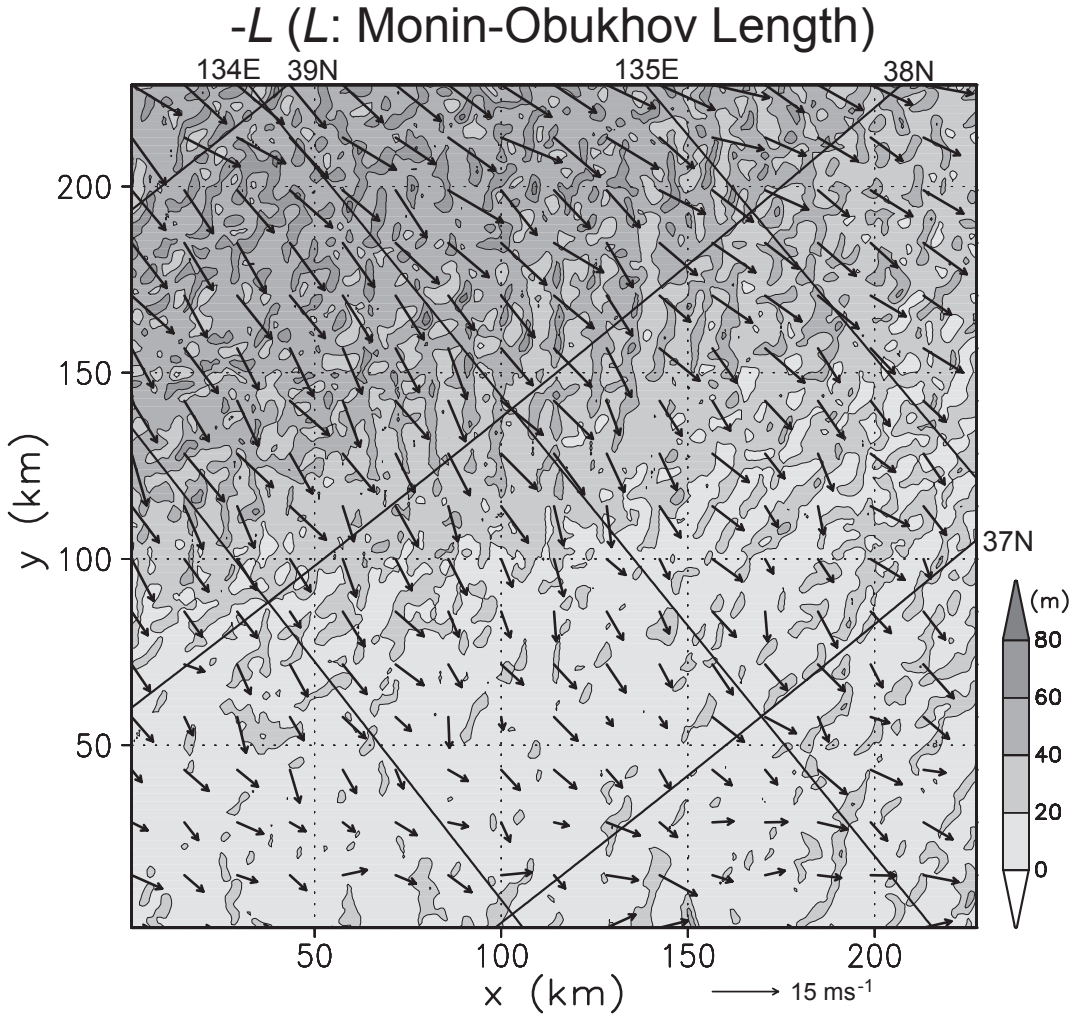


Figure 4.20: Same as Fig. 4.15, except for $-L$ ($L$: the Monin–Obukhov Length (m) ) and horizontal wind vector distributions at a height of 0.02 km.

In the present case, the parameters are estimated from model outputs. Figure 4.20 shows the horizontal distribution of $-L$ and horizontal wind vectors near the surface around the same area as shown in Fig. 4.15. As the air flows toward south, $-L$ gradually decreases from 60 to 10 m, indicating that the mixed layer becomes more unstable. This pattern almost corresponds to the north–south

gradient of the SST (not shown). As the air flows toward south, $z_i$ estimated from the height of constant $\theta_e$ layer increases from 1.5 to 3.0 km (not shown). As a result, the ratio $-z_i / L$ ranges from 25 to 300, indicating that Grossman's (1982) criterions for $-z_i / L$ is not met in the present case. There may be as yet unknown reasons why roll circulations occur in the present situation of high $-z_i / L$. Grossman (1982) observed a marine, fair weather, trade-wind boundary layer in which $z_i$ was nearly at 0.6 km. In the present case, $z_i$ is deeper than that observed in Grossman's (1982) case; therefore, the value of $-z_i / L$ becomes higher. The present mixed layer is in more moist condition; therefore, latent heat release associated with convective clouds play an effective role in the deepening of the mixed layer (e.g., Asai and Nakamura 1978). Similarly, Kristovich (1993) observed roll circulations in the mixed layer over Lake Michigan in which $z_i$ was at 1.0–1.5 km, when $-z_i / L$ was larger than 30.

It is also presented in the previous sections that the transversal cloud bands become wide and deep toward the southwest. These features are similar to those of the cloud streets (e.g., Miura 1986). As mentioned above, $-L$ decreases as the air flows toward south, indicating that the mixed layer becomes more unstable. With a decrease of the stability, the mixed layer becomes deep. The widening and deepening of the transversal cloud bands occur in this condition. Latent heat release associated with convective clouds probably affects the deepening of the mixed layer (e.g., Asai and Nakamura 1978).

Several studies (e.g., Hozumi and Magono 1984; Arakawa et al. 1988) proposed that the transversal cloud bands were mainly stratiform clouds, which extend northeastward from the developed convective cloud band. However, remarkable stratiform clouds were not found in the present case. In contrast, convective clouds were dominant in the area of the observed and simulated transversal cloud bands. Hozumi and Magono (1984) showed that a few anvil-like clouds were seen to extend from the top of the developed convective cloud band; however, they were considerably small compared with the stratiform clouds in the area of the transversal cloud bands. In this case, aircraft and satellite observations suggest that the developed convective cloud band contained several cumulonimbi with anvil-like clouds. However, anvil-like clouds appeared to form in the limited areas near the cumulonimbi. Anvil-like clouds are not found around the simulated developed convective cloud band. These features of anvil-like clouds shown in our case are similar to those in Hozumi and Magono (1984). On the other hand, in the developing stage of the

JPCZ cloud band under the eastward propagation of the trough, the areas with lower TB were broader. This suggests that cumulonimbi developed deeper, and anvil-like clouds extended wider in the area of the transversal cloud bands (see Figs. 4.3e and 4.3f). Further observational and numerical studies are necessary to clarify the structure of transversal cloud bands in the developing JPCZ cloud band.

In the present JPCZ cloud band, an area with relatively smaller cloud coverage (see the dashed ellipse in Fig. 4.3d) was observed around the developed convective cloud band (see the bold line in Fig. 4.3d), where the transversal cloud bands partly separated from the developed convective cloud band. In the developing stage of the JPCZ cloud band, the small cloud coverage area became distinct (see the dashed ellipse in Fig. 4.3e), so that the transversal cloud bands appeared to separate from the developed convective cloud band (see the bold line in Fig. 4.3e). In this stage, the transversal cloud bands gradually developed, and finally, the developed convective cloud band appeared to shift toward the southwestern edge of the transversal cloud bands (see the bold line in Fig. 4.3f). Therefore, the area with relatively smaller cloud coverage could be a transitional area between the old and new developed convective cloud bands. Further analysis of the change in the structure in the developing stage of the JPCZ cloud band is needed to clarify the formation mechanism of the area with relatively smaller cloud coverage. These are the future issues.

## 4.6 Conclusions

The JPCZ cloud band was observed over the Sea of Japan on 13–15 January 2001 during the WMO-01 field campaign. It extended from the base of the Korean Peninsula to the Japanese Islands. As the upper-level trough approached the Sea of Japan, the JPCZ cloud band gradually developed, and then its downstream part moved between the San-in district and the Tohoku district to cause heavy snowfalls there.

On 14 January 2001, the JPCZ cloud band extended almost straightly southeastward from the base of the Korean Peninsula to Wakasa Bay, and it stagnated during half a day. In this period, besides the satellite observations, the instrumented aircraft observation and upper-air soundings from two observation

vessels were conducted off the coast of the San-in district to capture the characteristics of the cloud bands embedded in the JPCZ cloud band. Moreover, the JPCZ cloud band was successfully reproduced by the JMA-NHM with a horizontal grid size of 1 km that was nested within the forecasts of the RSM. Figure 4.21 illustrates a conceptual model of the detailed structure of the JPCZ cloud band observed on 14 January 2001 by analyzing the simulation results of the JMA-NHM in addition to the special observations of the WMO-01.

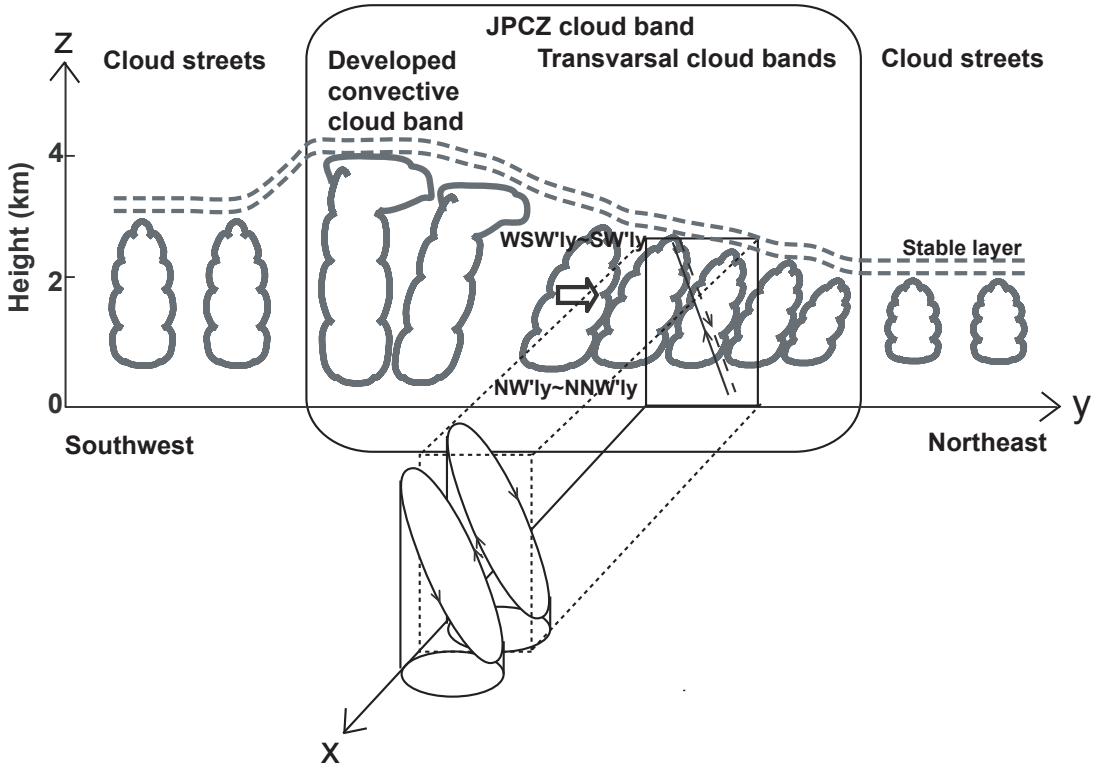


Figure 4.21: Conceptual model of the mesoscale structures of the JPCZ cloud band on 14 January 2001. Vertical cross section normal to the JPCZ cloud band is displayed in the y–z plane. Bold solid lines denote clouds. Double dashed lines indicate a stable layer. An open arrow indicates a direction of the vertical wind shear vector in the mixed layer nearly parallel to the page. Typical three-dimensional streamlines of eddy velocities $(u', v', w')$ in the rectangle on the y–z plane are illustrated by solid ellipses with arrows. The solid and dashed arrows denote projections of the streamlines of eddy velocities $(v', w')$ on the y–z plane.

The JPCZ cloud band consisted of two typical cloud bands; one was a developed convective cloud band, and the others were transversal cloud bands. The developed convective cloud band was found along the southwestern edge of the JPCZ cloud band. It contained relatively deep (~4 km) convective clouds. The transversal cloud bands extending to the northeast from the developed convective cloud band were aligned in a northwest–southeast direction. Vertical shear in the horizontal wind field existed in the mixed layer accompanied by the transversal cloud bands. The wind direction in the mixed layer rotated counter-clockwise with height from the north-northwest–northwest to the west-southwest–southwest.

The transversal cloud bands mainly consisted of convective clouds. The clouds slanted with height toward the northeast, which was the direction pointed by the vertical shear vector of horizontal wind in the mixed layer. The downwshearward tilt of the clouds was caused by the differential advection due to the vertical shear of the horizontal wind. A convectively unstable layer was observed in the lower layer under the transversal cloud bands. The transversal cloud bands widened and deepened toward southwest, as the depth of the mixed layer increased due to the increase of the sea surface temperature toward the downwind side. An examination of simulation results showed that the transversal cloud bands were accompanied by roll circulations. The axes of rolls were oriented nearly parallel to the direction of the vertical shear vector in the mixed layer. An analysis of the EKE budget indicated that the roll circulations derived most of their energy from the mean vertical shear and the buoyancy. The characteristics of the transversal cloud bands shown in Fig. 4.21 were also found in the other place where the transversal cloud bands are present.

When the upper-level trough approached, the JPCZ cloud band developed and moved northward. Various changes in the structure appeared in the developing JPCZ cloud band. Further observational and numerical studies are necessary to clarify the change of the JPCZ cloud band, especially the formation and decay of the area with relatively smaller cloud coverage around the developed convective cloud band pointed out in this chapter.

# Chapter 5

# General discussion

## 5.1 Comparison with other snowbands

In this section, the present snowband is compared with other cases from the view of their characteristics and the formation and maintenance mechanisms. The snowbands along the western coast of the Hokuriku district studied by Ishihara et al. (1989, hereinafter ISY89) had similar formation mechanism, in which the convergence of the winter monsoon and a land breeze produces cumulus convection to organize the snowband, to that described in the present snowband. Both snowbands resembles in shape, horizontal scale and vertical extent. Major differences between the snowbands in ISY89 and the present one are their movement and lifetime. The snowbands in ISY89 repeatedly formed (4 times per 3 h) with a short lifetime (1.0–1.5 h) and traveled faster toward the coast (~5 m $s^{-1}$), while the present snowband lasted and stagnated for a long time. The snowband movement is affected by the wind direction around the snowband that controls the movement of snow cells and snow systems, which are components of the snowband (see Chapter 3). The typical wind direction around the snowband is often westerly in this region. The direction of the present snowband was nearly wind-parallel, while the snowbands in ISY89 formed in the wind-normal direction. Therefore, the snowbands in ISY89 were forced to move toward the land, and they rapidly dissipated due to the cutoff of heat and water vapor supply from the sea, differently from the present snowband.

Ohigashi and Tsuboki (2005, hereinafter OT05) presented that double snowbands were quasi-stationary along the western coast of the Hokuriku district with a long lifetime (~20 h). They formed in the convergence zone between the winter monsoon and a land breeze; therefore, the formation

mechanism is the same as that of the present and ISY89's case. However, their location and movement are different from those of the present and ISY89's case, owing to different behaviors of a land breeze. In OT05's case, the land breeze uniformly continued during the occurrence of the snowbands, contributing to maintain the quasi-stationary snowbands. However, the successive formation and movement of the snowbands were observed in ISY89's case. They were largely dependent on the duration of a land breeze with the periodical intensification. As stated above, the snowbands along the western coastal line of the Hokuriku district (ISY89's and OT05's cases) formed in the wind-normal direction; therefore their location and movement are strongly affected by the balance between a land breeze and the winter monsoon. Moreover, gusts or stronger cold outflows produced by the snowbands sometimes contribute to the generation of new snowbands (e.g., ISY89). On the other hand, the snowbands along the eastern coastal line of the Hokuriku district, just like the present case, form in the nearly wind-parallel direction; therefore, it is hard to move toward the land. In this situation, a weak cold pool effectively helps to maintain the horizontal convergence, compensating for the weakened land breeze.

This type of snowband, which forms due to an interaction between a land breeze and the winter monsoon, can form in the other coastal regions that face the Sea of Japan. In fact, the snowband accompanied with a land breeze often forms and develops along the west coast of Hokkaido. The stagnation of snowbands often causes heavy snowfalls. Doppler radar studies revealed the formation and maintenance processes of the snowbands (Fujiyoshi et al. 1988; Tsuboki et al. 1989). The snowband observed along the west coast of Hokkaido resembles the present snowband in the structure and the formation mechanism: a single band and an interaction between the winter monsoon and a land breeze. However, the snowband observed along the west coast of Hokkaido had neither gust nor cold pool. Therefore, the maintenance of the land breeze is important to that of the snowband, because it maintains the horizontal convergence. On the other hand, in the present case, a cold pool contributes to the maintenance of the horizontal convergence, because it compensates for the weakened land breeze.

As stated here, the behavior and characteristics of snowbands along the coastal line depend primary on the behavior of a land breeze, and secondary on the scale of a cold pool produced by themselves. Further analytical and numerical studies, which focus on the evolution and duration of the land breeze

and the formation of the cold pool, are needed to understand fully the formation and maintenance mechanisms of the snowbands.

Different types of snowbands were observed around the coastal region of the Japanese Islands. Both snowbands studied by Maki et al. (1992) and Fujiyoshi et al. (1998) were the developed longitudinal-mode cloud bands, that is, cloud streets. As mentioned above, they are produced from shear-parallel mode roll convections related to thermal instability in the vertical shear flow (Asai 1970a, 1970b, and 1972). Sakakibara et al. (1988b) observed two squall line-like snowbands in the western Hokuriku district. They formed offshore and moved eastward. Gust fronts were observed during the passage of the snowbands, contributing to the maintenance of the snowbands. Though the formation mechanism is not clearly stated in their study, it looks that the snowbands were developed transversal cloud bands.

During the WMO-01, the snowbands investigated by Yoshihara et al. (2004) were observed around the eastern coast of Hokuriku district, where the present snowband was observed. Three snowbands successively formed about 70 km offshore in association with a cold front and moved southeastward. Yoshihara et al. (2004) showed that a low-level mesoscale convergence line, which formed 10–30 km offshore, contributed significantly to the successive development of the snowbands. As mentioned in the previous chapter, the convergence line is similar to that in the present case. However, their formation process and movement are different from those of the present snowband, owing to their different synoptic situation such as a cold front with a stronger winter monsoon.

## 5.2 Role of the JPCZ in the formation and maintenance of the snowbands

As described in the previous section, the present snowband formed along the eastern coast of the Hokuriku district in the convergence zone between the winter monsoon and a land breeze. The snowbands along the western coast of the Hokuriku district also have the same formation mechanism (e.g., Ishihara 1989; Ohigashi and Tsuboki 2005). They formed under the similar environmental conditions to the present case: the large sea-land temperature contrast to produce a land breeze circulation, large water vapor and heat supply from the sea surface to the low-level atmosphere, and the sufficiently weak

monsoon that can not break the land breeze circulation. Therefore, just like the present case, the snowbands are often simultaneously observed along both the eastern and western coastal lines of the Hokuriku district under such environmental conditions (see Fig. 1.3).

Around the Hokuriku district, snow accumulates on the slopes of the mountain, cooling the air above the slopes. This cold air tends to flow downward to the coastal line as a land breeze. The SST near the coast of the Hokuriku District is relatively warmer under the influence of a warm current. Therefore, the sea-land temperature contrast tends to be large enough to intensify the land breeze circulation. The warmer sea surface also provides water vapor and heat to the colder winter monsoon.

The present snowband formed along the eastern coast of the Hokuriku district, where the transversal cloud bands landed (see Fig. 3.5). Another snowband in OT05 was simultaneously observed along the western coast of the Hokuriku district (see Fig. 1.3). The snowband was also observed in the downstream of the transversal cloud bands, forming under the same environmental condition as the present snowband. Figure 5.1 shows time-space plots of radar reflectivity at an altitude of 1 km derived from the Range Height Indicator (RHI) mode scans at an azimuth of 10.5$^{o}$ by the NIED X-band Doppler radar at Omi (see Fig. 3.2). Weak radar echoes moved southeastward and merged into the snowband. The echoes (referred to as "T-mode echoes" in Kusunoki et al. 2002) had a line-shaped structure extending from the southwest to the northeast (not shown). T-mode echoes were observed in the area with transversal cloud bands (see Fig. 3.5). These features of T-mode echoes suggest that the transversal cloud bands flow into the snowband. As shown in Chapter 4, a low-level air with a higher $\theta_e$ was observed under the transversal cloud bands. The low-level air with the transversal cloud bands flowed into the northern or western side of the snowbands, generating cumulus convection. Therefore, the transversal cloud bands act as a source of the snowbands, playing an important role in the formation and maintenance of the snowbands.

Furthermore, the low-level flow in the area with the transversal cloud bands is weaker than in other areas where cold air outbreaks occur, as already mentioned in section 1.3, (e.g. Yagi et al. 1986; Nagata 1987; Ohigashi and Tsuboki 2005, 2007). The low-level flow tends to be weak, especially near the coastal region of the Hokuriku district (e.g., Ohigashi and Tsuboki 2005). Weak winter monsoon

is favorable for a land breeze to develop; therefore, it also contributes to the formation and maintenance of the snowbands.

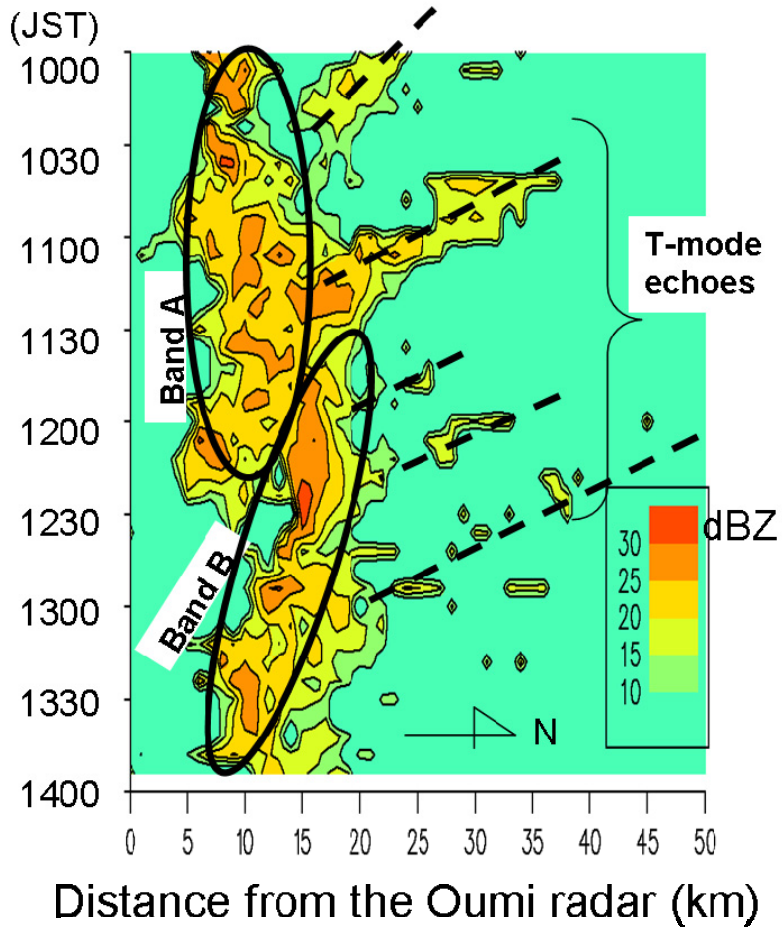


Figure 5.1: Time-space plots of radar reflectivity at an altitude of 1 km derived from the Range Height Indicator (RHI) mode scans at an azimuth of 10.5 ° by the NIED X-band Doppler radar at Omi on 16 January 2001 (adapted from Kusunoki et al. 2002).

Figure 5.2 shows a schematic depiction of the structure of the cloud bands causing heavy snowfalls to the coastal region of the Hokuriku and San-in districts and their relation to the JPCZ. As already shown in the previous chapters, the JPCZ generates the developed convective cloud band on the strongest convergence line in the southwestern side of the JPCZ. The developed convective cloud band lands and directly brings heavy snowfalls to the coastal plain areas of the Japanese Islands (see Figs 1.2b and 1.3; e.g., Okabayashi 1969; Yagi et al. 1986). In addition, the JPCZ also generates the transversal

cloud bands with a weak and convectively unstable low-level flow. The transversal cloud bands do not directly bring heavy snowfalls to the coastal region. However, as mentioned above, they probably act as a source of the coastal snowbands. Moreover, the JPCZ provides a favorable situation for the coastal snowbands to develop, which is the weak low-level flow with the transversal cloud bands. Therefore, the JPCZ contributes to the formation and maintenance of the coastal snowbands, affecting heavy snowfalls to the coastal region.

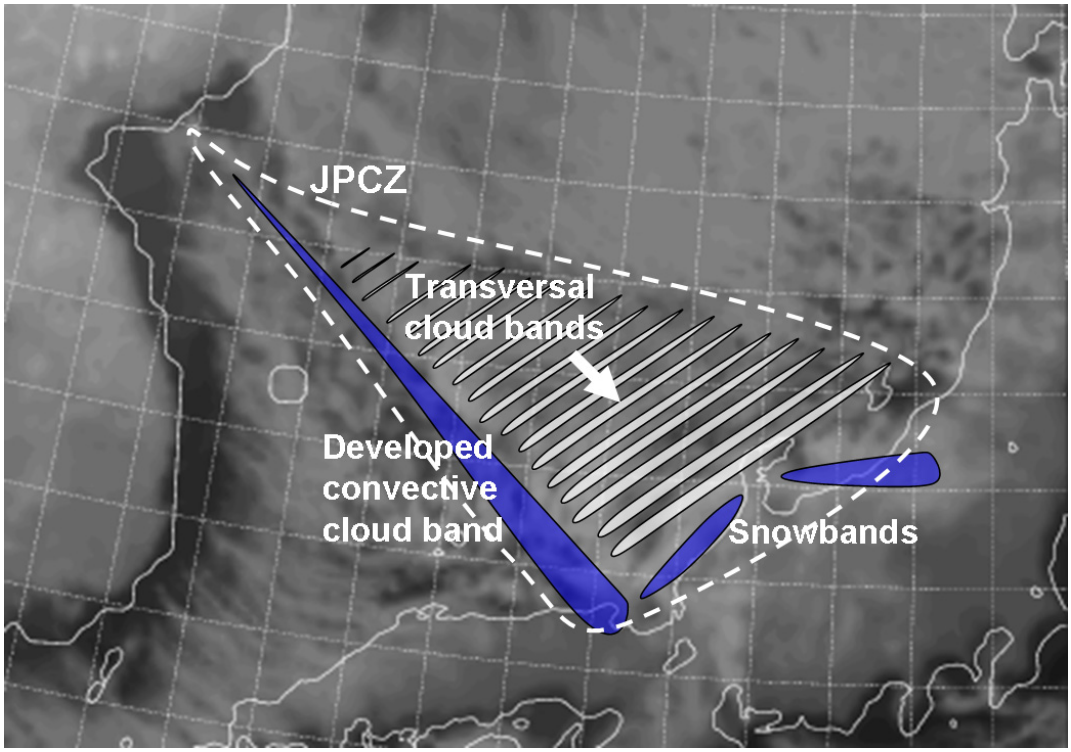


Figure 5.2: Schematic depiction of the structures of the cloud bands causing heavy snowfalls to the coastal region of the Hokuriku and San-in districts and their relation to the JPCZ. An area enclosed by a white dashed-line indicates the JPCZ. Blue bars denote precipitable cloud bands (the developed convective cloud band and snowbands). White bars denote non-precipitable cloud bands (the transversal cloud bands). A white arrow indicates the moving direction of the transversal cloud bands.

# Chapter 6

# General conclusions

In this thesis, cloud bands such as snowbands and the JPCZ cloud band, which brought P-type heavy snowfalls, have been investigated using the data obtained by a field campaign (WMO-01) and a cloud resolving model (JMA-NHM). Their high-resolution data provided essential information on the cloud bands, contributing to understand their inner structures and their formation and maintenance mechanisms.

In Chapter 1, phenomena focused in this thesis, such as snowbands and the JPCZ cloud band, were introduced. The WMO-01 and the JMA-NHM were also introduced. The purpose of this thesis was presented in this chapter.

In Chapter 2, an outline of the WMO-01 was presented. Various observation facilities and their locations were reported. An overview of the heavy snowfalls during the WMO-01 was also presented. P-type heavy snowfalls occurred over the coastal region of the Hokuriku and San-in districts during the period of 12–17 January 2001, when an upper-level synoptic-scale trough was quasi-stationary over the Sea of Japan. Cloud bands such as snowbands and the JPCZ cloud band periodically formed and developed under the affect of moving upper-level potential vorticity anomalies around the large-scale trough, causing heavy snowfalls to the coastal plain areas.

In Chapter 3, a quasi-stationary snowband observed on 16 January 2001 was analyzed. The snowband formed in the coastal area of the eastern Hokuriku district, causing a heavy snowfall in this area. The structure and the formation and maintenance mechanisms were investigated on the basis of observations (e.g., Doppler radars, BLRs, and upper-air soundings) and the simulation results of the JMA-NHM with a horizontal resolution of 1 km. The results obtained in

this chapter can be summarized as follows:

1. Structures of the snowband
   - Convective snow cells with the horizontal scale of a few km successively formed at the northern part of the snowband and propagated east-southeastward.
   - Meso-γ-scale convective snow systems were organized of developed snow cells in the snowband.
   - A cold pool formed under the snowband.
2. Formation mechanism of the snowband
   - A land breeze was a trigger for the formation of the snowband.
3. Formation mechanism of the cold pool and its role in maintenance of the snowband
   - The diabatic cooling due to sublimation of snow was responsible for the formation of the cold pool.
   - The cold pool contributed to the maintenance of the horizontal convergence with the northwesterly winter monsoon at the northern edge of the snowband by compensating for the weakened land breeze.

In Chapter 4, the JPCZ cloud band was investigated. On 14 January 2001, the JPCZ cloud band extended almost straightly southeastward from the base of the Korean Peninsula to Wakasa Bay, and it stagnated during half a day. In this period, the transversal cloud bands in the JPCZ cloud band were examined on the basis of observations (e.g., satellite images, in-situ measurement and CPR data from an instrumented aircraft, and upper-air soundings from observation vessels) and simulation results of the JMA-NHM with a horizontal resolution of 1 km. The results obtained in this chapter can be summarized as follows:

1. Structures of the transversal cloud bands
   - The transversal cloud bands extended along a northeast-southwest direction, which was parallel to the direction pointed by the vertical shear vector of horizontal wind in the mixed layer.
   - They mainly consisted of convective clouds, which slanted with height toward the downshear side.
   - They widened and deepened toward southwest, as the depth of the mixed layer increased.
   - A convectively unstable layer was observed in the lower layer under the transversal cloud bands.

2. Formation mechanism of the transversal cloud bands
   - The transversal cloud bands were accompanied by roll circulations.
   - The axes of rolls were oriented nearly parallel to the direction of the vertical shear vector in the mixed layer.
   - The roll circulations derived most of its energy from the mean vertical shear and the buoyancy.

In Chapter 5, the present snowband was compared with the other snowbands investigated in the previous studies. The snowbands along the western coast of the Hokuriku district had similar formation mechanism, in which the convergence of the winter monsoon and a land breeze produces cumulus convection to organize the snowband, to that described in the present snowband. However, they all had different behavior and characteristics on their movement and maintenance, which were strongly affected primary by a land breeze and secondary by a cold pool produced by themselves.

The relation between the snowband and the JPCZ cloud band was also discussed. The author focused the role of the transversal cloud bands in the maintenance and formation of the snowbands. Some of the results obtained through this study suggest that the transversal cloud bands with a higher $\theta_e$ low-level air flow into the snowbands, acting as a source of the snowbands. Moreover, the JPCZ provides a favorable situation for the snowband to develop, which is the weak low-level flow in the area with the transversal cloud bands. These aspects suggest that the JPCZ contributes to the formation and maintenance of the snowband.

In summary, the author clarified the detailed structures and the formation and maintenance processes of the cloud bands causing P-type heavy snowfalls such as the snowband and the JPCZ cloud band, on the basis of observations and numerical experiments with high-resolution. The author also suggested that the JPCZ does not only generate the JPCZ cloud band but also play an important role in the formation and maintenance of the snowband. The previous studies (e.g. Akiyama 1981a and 1981b) presented that P-type heavy snowfalls occur when a upper-level cold trough slowly propagates to east after protruding southward over the Sea of Japan. They also suggested that mesoscale disturbances tend to form and cause P-type heavy snowfalls under the large-scale situation. In this thesis, the author clarified the contributions of respective mesoscale disturbances to P-type heavy snowfalls under the influence of the

JPCZ. Therefore, the findings shown in this thesis have led us to deeper understanding of the cause and detailed process for P-type heavy snowfalls in the western coastal region of the Japanese Islands during a cold air outbreak.

# Bibliography

Akiyama, T., 1981a: Time and spatial variations of heavy snowfalls in the Japan Sea coastal region Part I. Principal time and space variations of precipitation described by EOF. *J. Meteor. Soc. Japan*, **59**, 578–590.

Akiyama, T., 1981b: Time and spatial variations of heavy snowfalls in the Japan Sea coastal region Part II. Large-scale situations for typical spatial distributions of heavy snowfalls classified by EOF. *J. Meteor. Soc. Japan*, **59**, 591–601.

Arakawa, S. and Research Group on Mesoscale Meteorology of Marine Development, JMA, 1988: On the mesoscale structure of the cloud band system over Japan Sea in winter monsoon period.—A mesoscale observation on board R/V Keifu-Maru. *Tenki*, **35**, 237–248 (in Japanese).

Asai, T., 1965: A numerical study of the air-mass transformation over the Japan Sea in winter. *J. Meteor. Soc. Japan*, **43**, 1-15.

Asai, T., 1970a: Three-dimensional features of thermal convection in a plane Couette flow. *J. Meteor. Soc. Japan*, **48**, 18–29.

Asai, T., 1970b: Stability of a plane parallel flow with variable vertical shear and unstable stratification. *J. Meteor. Soc. Japan,* **48**, 129–139.

Asai, T., 1972: Thermal instability of a shear flow turning the direction with height. *J. Meteor. Soc. Japan,* **50**, 525–532.

Asai, T., 1988: Meso-scale features of heavy snowfalls in Japan Sea coastal regions of Japan. *Tenki*, **35**, 156–161 (in Japanese).

Asai, T. and K. Nakamura, 1978: A numerical experiment of airmass transformation processes over warmer sea. Part I: Development of a convectively mixed layer. *J. Meteor. Soc. Japan*, **56**, 424–434.

Bluestein, H. B. and M. H. Jain, 1985: Formation of mesoscale lines of precipitation: Severe squall lines in Oklahoma during the spring. *J. Atmos. Sci.*, **42**, 1711-1732.

Cotton, W. R., G. J. Tripoli, R. M. Rauber, and E. A. Mulvihill, 1986 : Numerical simulation of the effects of varying ice crystal nucleation rates and aggregation processes on orographic snowfall. *J. Clim. Appl. Meteor.,* **25**, 1658–1680.

Deardorff, J. W., 1972: Numerical investigation of neutral and unstable planetary boundary layers. *J. Atmos. Sci.,* **29**, 91–115.

Deardorff, J. W., 1980: Stratocumulus-capped mixed layers derived from a three-dimensional model. *Bound.-Layer Meteor.,* **18**, 495–527.

Eito, H., T. Kato, M. Yoshizaki, and A. Adachi, 2005: Numerical simulation of the quasi-stationary snowband observed over the southern coastal area of the Sea of Japan on 16 January 2001. *J. Meteor. Soc. Japan*, **83**, 551–576.

Eito, H., M. Murakami, C. Muroi, T. Kato, S. Hayashi, H. Kuroiwa, and M. Yoshizaki, 2010: The structure and formation mechanism of transversal cloud bands associated with the Japan-Sea Polar-Airmass Convergence Zone. *J. Meteor. Soc. Japan*, **88**, 625–648.

Endoh, T., K. Hozumi, and C. Magono, 1984: Formation mechanism of a notable cloud system that causes heavy snowfall and a tentative prediction of its behavior. *Natural Disaster Sci.*, **6**, 31–42.

Estoque, M. A. and K. Ninomiya, 1976: Numerical simulation of Japan Sea effect snowfall. *Tellus*, **28**, 243–253.

Fujiyoshi, Y., K. Tsuboki, H. Konishi, and G. Wakahama, 1988: Doppler radar observation of convergence band cloud formed on the west coast of Hokkaido Island (I): warm frontal type. *Tenki*, **35**, 427–439 (in Japanese).

Fujiyoshi, Y., K. Tsuboki, S. Satoh, and G. Wakahama, 1992: Three-dimensional radar echo structure of a snow band formed on the lee side of a mountain. *J. Meteor. Soc. Japan*, **70**, 11–24.

Fujiyoshi, Y., N. Yoshimoto, and T. Takeda, 1998: A dual-Doppler radar study of longitudinal-mode snowbands. Part I: A three-dimensional kinematic structure of meso-γ-scale convective cloud systems within a longitudinal-mode snowband. *Mon. Wea. Rev.*, **126**, 72–91.

Grossman, R. L., 1982: An analysis of vertical velocity spectra obtained in the BOMEX fair-weather, trade-wind boundary layer. *Bound.-Layer Meteor.,* **23**, 323–357.

Hirota, I., K. Yamada, and K. Sato, 1995: Medium-scale travelling waves over the north Atlantic. *J. Met. Soc. Japan*, **73**, 1175–1179.

Horie, H., T. Iguchi, H. Hanado, H. Kuroiwa, H. Okamoto, and H. Kumagai, 2000: Development of a 95-GHz airborne cloud profiling radar (SPIDER): Technical aspects. *IEICE Trans. Commun.,* **E83-B**, 2010–2020.

Hoskins, B. J., M. E. McIntyre, and A. W. Robertson, 1985: On the use and significance of isentropic potential vorticity maps. *Quart. J. Roy. Meteor. Soc.*, **111**, 877–946.

Hozumi, K. and C. Magono, 1984: The cloud structure of convergent cloud bands over the Japan Sea in winter monsoon period. *J. Meteor. Soc. Japan*, **62**, 522–533.

Ikawa, M., 1988: 2-dimensional simulation of the convective snow band observed over Japan Sea, Part 2 - Precipitation mechanism of the convective snow band and the effects of the different parameterization of cloud microphysics on the convective snow band -. *Papers Meteor. Geophys.*, **39**, 13–43.

Ikawa, M. and K. Saito, 1991: Description of a nonhydrostatic model developed at the Forecast Research Department of the MRI. *Tech. Rep. of the MRI*, **28**, 238pp.

Ikawa, M., H. Sakakibara, M. Ishihara, and Z. Yanagisawa, 1987: 2-dimensional simulation of the convective snow band observed over the Japan Sea - the structure and time evolution of the organized multicellular convection -. *J. Meteor. Soc. Japan*, **65**, 605–633.

Ishihara, M., H. Sakakiara, and Z. Yanagisawa, 1989: Doppler radar analysis of the structure of mesoscale snow bands developed between the winter monsoon and the land breeze. *J. Meteor. Soc. Japan*, **67**, 503–520.

Japan Meteorological Agency, 2002: Outline of the operational numerical weather prediction at the Japan Meteorological Agency. *Appendix to WMO Numerical Weather Prediction Progress Report*, 157 pp.

Kato, T., 1998: Numerical simulation of the band-shaped torrential rain observed over southern Kyushu, Japan on 1 August 1993, *J. Meteor. Soc. Japan*, **76**, 97–128.

Kato, T. and H. Goda, 2001: Formation and maintenance processes of a stationary band-shaped heavy rainfall observed in Niigata on 4 August 1998. *J. Meteor. Soc. Japan*, **79**, 899–924.

Kawashima, M., 2007: Numerical study of precipitation core-gap structure along cold fronts. *J. Atmos. Sci.,* **64**, 2355–2377.

Kawashima, M. and Y. Fujiyoshi, 2005: Shear instability wave along a snowband: Instability structure, evolution, and energetics derived from dual-Doppler radar data. *J. Atmos. Sci.,* **62**, 351–370.

Kondo, J., 1975: Air-sea bulk transfer coefficients in diabatic conditions. *Bound.-Layer Meteor.,* **9**, 91–112.

Kristovich, D. A. R., 1993: Mean circulations of boundary-layer rolls in lake-effect snow storms. *Bound.-Layer Meteor.*, **63**, 293–315.

Kumagai, H., K. Nakamura, H. Hanado, K. Okamoto, N. Hosaka, N. Miyano, T. Kozu, N. Takahashi, T. Iguchi, and H. Miyauchi, 1996: CRL Airborne Multiparameter Precipitation Radar (CAMPR): System description and preliminary results. *IEICE Trans. Commun.,* **E79-B**, 770–778.

Kusunoki, K., K. Iwanami, M. Maki, S. G. Park, R. Misumi, and WMO-01 Observation Group, 2002: A dual-Doppler analysis of the mesoscale snow bands under the winter monsoon Part I: Band regeneration. *Proc. International conference on mesoscale convective systems and heavy rainfall/snowfall in East Asia*, 546–550.

LeMone, M. A., 1973: The structure and dynamics of horizontal roll vortices in the planetary boundary layer. *J. Atmos. Sci.,* **30**, 1077–1091.

Lin, Y. H., R. D. Farley, and H. D. Orville, 1983: Bulk parameterization of the snow field in a cloud model. *J. Clim. Appl. Meteor.,* **22**, 1065–1092.

Maki, M., S. Nakai, T. Yagi, and H. Nakamura, 1992: Doppler radar observations of snow stroms: L-mode case. *Tenki*, **39**, 551–563 (in Japanese).

Matsumoto, S., K. Ninomiya, and T. Akiyama, 1967: A synoptic and dynamic study on the three dimensional structure of mesoscale disturbances observed in the vicinity of a cold vortex center. *J. Meteor. Soc. Japan*, **45**, 64–82.

Miura, Y., 1986: Aspect ratios of longitudinal rolls and convection cells observed during cold air outbreaks. *J. Atmos. Sci.,* **43**, 26–39.

Miyazawa, S., 1968: A mesoclimatological study on heavy snowfall. *Papers Meteor. Geophys.*, **19**, 487–550 .

Murakami, M., 1990: Numerical modeling of dynamical and microphysical evolution of an isolated convective cloud – The 19 July 1981 CCOPE cloud. *J. Meteor. Soc. Japan*, **68**, 107–128.

Nagata, M., 1987: On the structure of a convergent cloud band over the Japan Sea in winter; a prediction experiment. *J. Meteor. Soc. Japan*, **65**, 871–883.

Nagata, M., 1991: Further numerical study on the formation of the convergent cloud band over the Japan Sea in winter. *J. Meteor. Soc. Japan*, **69**, 419–428.

Nagata, M., 1992: Modeling case study of the Japan-Sea convergent cloud band in a varying large-scale environment: Evolution and upscale effect. *J. Meteor. Soc. Japan*, **70**, 649–671.

Nagata, M., 1993: Meso-β-scale vortices developing along the Japan-Sea Polar-Airmass Convergence Zone (JPCZ) cloud band: numerical simulation. *J. Meteor. Soc. Japan*, **71**, 43–57.

Nagata, M., M. Ikawa, S. Yoshizumi, and T. Yoshida, 1986: On the formation of a convergent cloud band over the Japan Sea in winter; Numerical experiments. *J. Meteor. Soc. Japan*, **64**, 841–855.

Ninomiya, K., 1968: Heat and water budget over the Japan Sea and the Japan Islands in winter season. *J. Meteor. Soc. Japan*, **46**, 343–372.

Ogura, Y., 2000: *An introduction to synoptic-dynamic meteorology*. University of Tokyo Press, 289 pp (in Japanese).

Okabayashi, T., 1969: Photograph of heavy snowfall on Japan Sea side on Jan. 2, 1969, taken by ESSA. *Tenki*, **16**, 79–80 (in Japanese).

Okabayashi, T., 1972: Snow clouds seen from meteorological satellites and their application to the research on snowfall. *Kisho Kenkyuu Note*, **113**, 74–106 (in Japanese).

Okabayashi, T. and M. Satomi, 1971: A study on the snowfall and its original clouds by the meteorological radar and satellite (Part I). *Tenki*, **18**, 573–581 (in Japanese).

Ohigashi, T. and K. Tsuboki, 2005: Structure and Maintenance Process of Stationary Double Snowbands along the Coastal Region. *J. Meteor. Soc. Japan*, **83**, 331–349.

Ohigashi, T. and K. Tsuboki, 2007: Shift and intensification processes of the Japan-Sea Polar-Airmass Convergence Zone associated with the passage of a mid-tropospheric cold core. *J. Meteor. Soc. Japan*, **85**, 633–662.

Saito, K., T. Fujita, Y. Yamada, J. Ishida, Y. Kumagai, K. Aranami, S. Ohmori, R. Nagasawa, S. Kumagai, C. Muroi, T. Kato, H. Eito, and Y. Yamazaki, 2006 : The operational JMA nonhydrostatic mesoscale model. *Mon. Wea. Rev.*, **134**, 1266–1298.

Saito, K., J. Ishida, K. Aranami, T. Hara, T. Segawa, M. Narita, and Y. Honda, 2007: Nonhydrostatic atmospheric models and operational development at JMA. *J. Meteor. Soc. Japan*, **85B**, 271–304.

Saito, K., T. Kato, H. Eito, and C. Muroi, 2001: Documentation of the Meteorological Research Institute / Numerical Prediction Division unified nonhydrostatic model. *Tech. Rep.of MRI*, **42**, p133.

Saito, K., M. Murakami, T. Matsuo, and H. Mizuno, 1996: Sensitivity experiments on the orographic snowfall over the mountainous region of northern Japan. *J. Meteor. Soc. Japan*, **74**, 797–813.

Sakakibara, H., M. Ishihara, and Z. Yanagisawa, 1988a: Classification of mesoscale snowfall systems observed in western Hokuriku during a heavy snowfall period in January 1984. *J. Met. Soc. Japan,* **66**, 193–199.

Sakakibara, H., M. Ishihara, and Z. Yanagisawa, 1988b: Squall line like convective snowbands over the Sea of Japan. *J. Meteor. Soc. Japan*, **66**, 937–953.

Sato, K., H. Eito, and I. Hirota, 1993: Medium-scale travelling waves in the extra-tropical upper troposphere. *J. Meteor. Soc. Japan*, **71**, 427–436.

Sato, K., K. Yamada, and I. Hirota, 2000: Global characteristics of medium-scale tropopausal waves observed in ECMWF operational data. *Mon. Wea. Rev.*, **128**, 3808–3823.

Seko, H., T. Kato, K. Saito, M. Yoshizaki, K. Kusunoki, and H. Okamura, 1999: Analytical and numerical studies of a quasi-stationary precipitation band observed over Kanto area associated with Typhoon 9426 (Orchid). *J. Meteor. Soc. Japan*, **77**, 929–928.

Shimizu, K. and K. Tsuboki, 2005: The formation process of transverse mode snowfall band observed in the offshore of Hokuriku on December 26th, 2000. *Kisho Kenkyuu Note*, **208**, 243–250 (in Japanese).

Sommeria, G., 1976: Three-dimensional simulation of turbulent processes in an undisturbed trade wind boundary layer. *J. Atmos. Sci.,* **33**, 216–241.

Sugi, M., K. Kuma, K. Tada, K. Tamiya, N. Hasegawa, T. Iwasaki, S. Yamada, and T. Kitade, 1990: Description and performance of the JMA operational global spectral model (JMAGSM88). *Geophys. Mag.,* **43**, 105–130.

Sykes, R. I., and D. S. Henn, 1989: Large-eddy simulation of turbulent sheared convection. *J. Atmos. Sci.,* **46**, 1106–1118.

Takayama, H. and M. Nagata 1995: Successive development of two types of vortex disturbance over the Japan Sea in winter (numerical simulation). *Papers Meteor. Geophys.*, **45**, 149–162.

Tsuboki K., Y. Fujiyoshi, and G. Wakahama, 1989: Doppler radar observation of convergence band cloud formed on the west coast of Hokkaido Island. II: Cold frontal type. *J. Meteor. Soc. Japan*, **67**, 985–999.

Tsuchiya, K. and T. Fujita, 1967: A satellite meteorological study of evaporation and cloud formation over the western Pacific under the influence of the winter monsoon. *J. Meteor. Soc. Japan*, **45**, 232–250.

Uemura, H., 1980: On the structure and formation of the disturbances causing a heavy snowfall over the coastal area of the Sea of Japan under the winter monsoon. *Tenki*, **27**, 33–44 (in Japanese).

Yagi, S., 1985: Large scale snow clouds with roll axes roughly perpendicular to the direction of winter monsoon burst: Observational studies of convective cloud roll axes and some theoretical consideration. *Tenki*, **32**, 175–187 (in Japanese).

Yagi, S., T. Muramatsu, T. Uchiyama, and N. Kurokawa, 1986: 'Convergent band cloud' and 'Cu-Cb line' over Japan Sea affected by topographic features in the coast of the Asian continent. *Tenki*, **33**, 453–465 (in Japanese).

Yamamori, M., and K. Sato, 1998: A quasi-geostrophic analysis on medium-scale waves near the midlatitude tropopause and their relation to the background state. *J. Met. Soc. Japan*, **76**, 879–888.

Yamamori, M., and K. Sato, 2002: An energy source of medium-scale tropopausal waves. *Mon. Wea. Rev.*, **130**, 1455–1467.

Yamamori, M., K. Sato, and I. Hirota, 1997: A study on seasonal variation of upper tropospheric medium-scale waves over East Asia based on regional climate model data. *J. Met. Soc. Japan*, **75**, 13–22.

Yoshihara, H., M. Kawashima, K. Arai, J. Inoue, and Y. Fujiyoshi, 2004: A Doppler radar study on the successive development of snowbands at a convergence line near the coastal region of Hokuriku district. *J. Meteor. Soc. Japan*, **82**, 1057–1079.

Yoshimoto, N., Y. Fujiyoshi, and T. Takeda, 2000: A dual-Doppler radar study of longitudinal-mode snowbands. Part II: Influence of the kinematics of a longitudinal-mode snowband on the development of an adjacent snowband. *J. Meteor. Soc. Japan*, **78**, 381–403.

Yoshizaki, M. and T. Kato, 2005: *Meteorology of heavy rainfall and snowfall.* Asakura Publishing Co., Ltd., 187 pp (in Japanese).

Yoshizaki, M., T. Kato, H. Eito, A. Adachi, M. Murakami, S. Hayashi, and WMO-01 Observation Group, 2001: A report on "Winter MCSs (mesoscale convective systems) observations over the Japan Sea in January 2001 (WMO-01)". *Tenki*, **48**, 893–903 (in Japanese).

Yoshizaki, M., T. Kato, H. Eito, S. Hayashi, and W. -K. Tao, 2004: An overview of the field experiment "Winter Mesoscale Convective Systems (MCSs) over the Japan Sea in 2001", and comparisons of the cold-air outbreak case (14 January) between analysis and a non-hydrostatic cloud-resolving model. *J. Meteor. Soc. Japan*, **82**, 1365–1387.

Yoshizaki, M., T. Kato, Y. Tanaka, H. Takayama, Y. Shoji, H. Seko, K. Arao, K. Manabe, and X-BAIU-98 Observation Group, 2000: Analytical and numerical study of the 26 June 1998 orographic rainband observed in western Kyushu, Japan, *J. Meteor. Soc. Japan*, **78**, 835–856.

# Publication list

Note: This thesis is based on articles numbered 6 and 9 of the following list. Reference articles for this thesis are marked with an asterisk.

**Refereed journals**

1. *Sato, K., H. Eito, and I. Hirota, 1993: Medium-scale travelling waves in the extra-tropical upper troposphere. *J. Meteor. Soc. Japan*, **71**, 427–436.

2. Kusunoki, K., H. Eito, and K. Akaeda, 2000: A case study of low-level internal gravity waves using Doppler radar and ACARS. *J. Meteor. Soc. Japan*, **78**, 511–525.

3. Saito, K., T. Kato, H. Eito, and C. Muroi, 2001: Documentation of the Meteorological Research Institute / Numerical Prediction Division unified nonhydrostatic model. *Tech. Rep. of MRI*, **42**, p133.

4. Kusunoki, K. and H. Eito, 2003: Analytical studies of low-level internal gravity waves over the Kanto plain associated with a stationary front. *Mon. Wea. Rev.*, **131**, 236–248.

5. *Yoshizaki, M., T. Kato, H. Eito, S. Hayashi, and W. -K. Tao, 2004: An overview of the field experiment “Winter Mesoscale Convective Systems (MCSs) over the Japan Sea in 2001”, and comparisons of the cold-air outbreak case (14 January) between analysis and a non-hydrostatic cloud-resolving model. *J. Meteor. Soc. Japan*, **82**, 1365–1387.

6. *Eito, H., T. Kato, M. Yoshizaki, and A. Adachi, 2005: Numerical simulation of the quasi-stationary snowband observed over the southern coastal area of the Sea of Japan on 16 January 2001. *J. Meteor. Soc. Japan*, **83**, 551–576.

7. *Saito, K., T. Fujita, Y. Yamada, J. Ishida, Y. Kumagai, K. Aranami, S. Ohmori, R. Nagasawa, S. Kumagai, C. Muroi, T. Kato, H. Eito, and Y. Yamazaki, 2006 : The operational JMA nonhydrostatic mesoscale model. *Mon. Wea. Rev.*, **134**, 1266–1298.

8. *Eito, H. and K. Aonashi, 2009: Verification of hydrometeor properties simulated by a cloud-resolving model using a passive microwave satellite and ground-based radar observations for a rainfall System associated with the Baiu front. *J. Meteor. Soc. Japan*, **87A**, 425–446.

9. *Eito, H., M. Murakami, C. Muroi, T. Kato, S. Hayashi, H. Kuroiwa, and M. Yoshizaki, 2010: The structure and formation mechanism of transversal cloud bands associated with the Japan-Sea Polar-Airmass Convergence Zone. *J. Meteor. Soc. Japan*, **88**, 625–648.

10. *Aonashi, K. and H. Eito, 2011: Displaced ensemble variational assimilation method to incorporate microwave imager brightness temperatures into a cloud-resolving model. *J. Meteor. Soc. Japan*, **89**, 175–194.

**Unrefereed articles**

11. Eito, H., M., Yoshizaki, T., Kato, K., Saito, and Y., Mano, 1999: 3-D numerical experiments of marine stratocumulus observed around Japan Islands in winter. *CAS/JSC WGNE Research Activities in Atmospheric and Oceanic Modelling*, **29**, 5.21–5.22.

12. Kusunoki, K., H. Eito, and K. Akaeda, 2000: Low–level internal gravity waves observed with the Narita Doppler radar for airport weather. *Tenki*, **47**, 345–346 (in Japanese).

13. Muroi, C., K. Saito, T. Kato, and H. Eito, 2000: Development of the MRI/NPD nonhydrostatic model. *CAS/JSC WGNE Research Activities in Atmospheric and Oceanic Modelling*, **30**, 5.25–5.30.

14. Saito, K., T. Kato, H. Eito, A. Murata, and N. Seino, 2000: Report on the Third International SRNWP (Short–Range Numerical Weather Prediction) workshop on Nonhydrostatic Modelling. Tenki, **47**, 203–210 (in Japanese).

15. Yoshizaki, M., H. Seko, T. Kato, Y. Shoji, H. Eito, K. Bessho, H. Goda, and X-BAIU-99 Observation Group, 2000: A report on a special observation of Baiu over East China Sea and Kyushu in 1999 (X–BAIU–99). *Tenki*, **47**, 217–224 (in Japanese).

16. Saito, K., T. Kato, H. Eito, and C. Muroi, 2001: Cloud resolving simulation of cold air outbreak over Japan with a parallel version of the MRI/NPD nonhydrostatic model. *CAS/JSC WGNE Research Activities in Atmospheric and Oceanic Modelling*, **31**, 5.36–5.37.

17. Saito, K., J. Steppeler, T. Kato, H. Eito, N. Seino, and A. Murata, 2001: Report on the Third International SRNWP (Short–Range Numerical Weather Prediction) Workshops on nonhydrostatic modelling. *Bulletin of the American Meteorological Society,* **82***,* 2245–2250.

18. Yoshizaki, M., T. Kato, H. Eito, A. Adachi, M. Murakami, S. Hayashi, and WMO-01 Observation Group, 2001: A report on "Winter MCSs (mesoscale convective systems) observations over the Japan Sea in January 2001 (WMO-01)". *Tenki*, **48**, 893–903 (in Japanese).

19. Eito, H., T. Kato, and M. Yoshizaki, 2002: Numerical Simulation of Heavy Snowfall Systems observed on the southern coastal area of Sea of Japan on 16 January 2001. *CAS/JSC WGNE Research Activities in Atmospheric and Oceanic Modelling*, **32**, 5.7–5.8.

20. Kato, T., S. Shimizu, S. Kanada, W. Yanase, N. Kitabatake, H. Fudeyasu, T. Maesaka, Q. Moteki, M. Yoshizaki, and H. Eito, 2002: Report on "International Conference on Meso–scale Meteorology and Typhoon in East Asia" (Taipei, Taiwan) on 26–28 September 2001. *Tenki*, **49**, 227–231 (in Japanese).

21. Yoshizaki, M., T. Kato, C. Muroi, H. Eito, S. Hayashi, Y. Shibagaki, K. Araki, K. Suzuki, M. Murakami, H. Kuroiwa, and H. Minda, 2003: A report on field observations of Baiu fronts over East China Sea and Kyushu in 2001 and 2002. *Tenki*, **50**, 561–569 (in Japanese).

22. Yoshizaki, M., H. Eito, S. Hayashi, T. Kato, K. Aonashi, M. Murakami, H. Kuroiwa, and H. Minda, 2003: A report on "Winter MCSs (mesoscale convective systems) Observation over the Japan Sea–2003 (WMO–03)". *Tenki*, **50**, 661–668 (in Japanese).

23. Eito, H., C. Muroi, S. Hayashi, T. Kato, and M. Yoshizaki, 2004: A high-resolution wide-range numerical simulation of cloud bands associated with The Japan Sea Polar-air mass Convergence Zone in winter using a non-hydrostatic model on the Earth Simulator. *CAS/JSC WGNE Research Activities in Atmospheric and Oceanic Modelling*, **34**, 5.7–5.8.

24. Fujiyoshi, Y., T. Takemi, T. Nasuno, N. Kuba, H. Yamada, M. Katsumata, H. Uyeda, K. Tsuboki, C. Takahashi, T. Ohigashi, Y. Shusse, M. Nomura, S. Shimizu, K. Moteki, R. Misumi, S. Nakai, M. Ishizaka, K. Iwamoto, M. Wada, M. Murakami, N. Orikasa, K. Kusunoki, H. Eito, A. Hashimoto, S. Kanada, and A. Watanabe, 2004: Report on 14th International Conference on Clouds and Precipitation (ICCP). *Tenki*, **52**, 41–44 (in Japanese).

25. Kato, T., K. Yasunaga, C. Muroi, M. Yoshizaki, S. Kanada, A. Hashimoto, Y. Wakazuki, H. Eito, S. Hayashi, and H. Sasaki, 2004: Regional climate prediction by using a Japan Meteorological Agency nonhydrostatic model with a high resolution. Part 1: Outline/purpose of a high-resolution long-term prediction. *CAS/JSC WGNE Research Activities in Atmospheric and Oceanic Modelling*, **34**, 7.19 – 7.20.

26. Nakamura, H., W. Ohfuchi, M. Yoshioka, K. Takaya, T. Enomoto, C. Muroi, H. Eito, and Y. Kawatani, 2004: Report on 23th workshop on mesoscale meteorology. *Tenki*, **51**, 141–149 (in Japanese).

27. Noda, A. T., T. Takemi, Y. Wakatsuki, H. Kusaka, H. Tomita, Y. Honda, H. Eito, and T. Iwasaki, 2004: Sixth workshop on non–hydrostatic modeling. *Tenki*, **52**, 369–372 (in Japanese).

28. Eito, H., 2005: A high-resolution numerical simulation of cloud bands associated with the Japan Sea Polar-air mass Convergence Zone using the JMA-NHM. *Kisho Kenkyuu Note*, **208**, 265–276 (in Japanese).

29. Eito, H., 2005: Numerical simulation of the quasi-stationary snowband observed over the Joetsu region in Niigata prefecture on 16 January 2001. *Kisho Kenkyuu Note*, **208**, 311–319 (in Japanese).

30. Eito, H., K. Aonashi, G. Liu, C. Muroi, S. Hayashi, T. Kato, and M. Yoshizaki 2005: Preliminary comparison of AMSR-E observation and numerical simulation with cloud resolving model for solid precipitation in winter during the Wakasa 2003. *CAS/JSC WGNE Research Activities in Atmospheric and Oceanic Modelling*, **35**, 5.3–5.4.

31. Eito, H. and K. Aonashi, 2007: Resolution dependence of hydrometeor structures generated by cloud resolving model. *CAS/JSC WGNE Research Activities in Atmospheric and Oceanic Modelling*, **37**, 5.7–5.8.

32. Eito, H. and K. Aonashi, 2008: The sensitivity of passive microwave responses to the hydrometeor properties simulated by a cloud resolving model in real rainfall systems associated with Baiu front. *CAS/JSC WGNE Research Activities in Atmospheric and Oceanic Modelling*, **38**, 5.3–5.4.

33. Ohigashi, T., H. Eito, Y. Fujiyoshi, H. Okamoto, W. Yanase, and K. Kusunoki, 2010: Report on 33th workshop on mesoscale meteorology. *Tenki*, **57**, 707–712 (in Japanese).